Thermodynamically constrained surface energy balance using medium-resolution remote sensing for efficient evapotranspiration mapping

Yeonuk Kim[a,*], Justin L Huntington[a], Bruno Comini de Andrade[b], Mark S Johnson[c,d], John M Volk[a], Sayantan Majumdar[a], Charles Morton[a], Peter ReVelle[a]

Affiliations

a. Division of Hydrologic Sciences, Desert Research Institute, Reno, Nevada, USA
b. Hydraulic Research Institute, Federal University of Rio Grande do Sul, Porto Alegre, Brazil
c. Institute for Resources, Environment and Sustainability, University of British Columbia, Vancouver, BC, Canada
d. Department of Earth, Ocean and Atmospheric Sciences, University of British Columbia, Vancouver, BC, Canada

***Corresponding author:** Yeonuk Kim (yeonuk.kim@dri.edu)

This manuscript is a non-peer reviewed preprint submitted to EarthArXiv.

Abstract

Medium-resolution (10-100 m) satellite evapotranspiration (ET) products are rapidly advancing agricultural water resources research and management, but underperformance across non-agricultural land cover continues to limit broader hydrologic and ecosystem applications. These inconsistencies are often linked to model structure and representation of ET dynamics across space and time. In extensive natural ecosystems such as forests and shrublands, ET is primarily governed by equilibrium radiative energy exchange, whereas in croplands it is often enhanced by advective energy inputs. While select models represent these processes, recent intercomparison studies highlight persistent performance gaps across land covers. We hypothesize that model structure governing land–atmospheric coupling, rather than sensor limitations alone, remains a primary constraint on medium-resolution ET performance.

Here, we introduce a diffusivity-independent equilibrium formulation free of conductance terms that conditionally incorporates aerodynamic enhancement when advection is expected. Landsat thermal and optical observations are integrated with gridded meteorological data within the presented Radiation Advection Diffusivity-independent ET (RADET) modeling framework to predict ET. Performance is evaluated using 145 in situ flux stations across the contiguous United States and intercomparisons with OpenET and

MODIS products. Results indicate that RADET achieves comparable performance to leading models in croplands while providing consistent improvements across natural ecosystems, including ~35% lower mean absolute error and sustained positive Nash-Sutcliffe efficiency where ensemble models often showed reduced skill. Application of satellite-based equilibrium formulations with conditional transport enhancement enables computationally efficient generation of medium-resolution ET with robust cross-land cover performance, advancing research and operational applications emphasized in recent medium-resolution remote sensing initiatives.

Keywords

evapotranspiration, Landsat surface temperature, surface energy balance modeling, medium-resolution remote sensing

Highlights

- Introduced RADET, a Radiation Advection Diffusivity-independent ET framework
- Produced 30 m daily and monthly ET estimates using Landsat and gridded meteorology
- Comparable to OpenET in croplands with superior performance across natural ecosystems
- Improved agreement relative to MODIS ET products across cropland and non-cropland systems
- Computationally efficient and operationally scalable

1. Introduction

Evapotranspiration (ET), the combined flux of plant transpiration and soil evaporation, is the second-largest terrestrial hydrologic flux after precipitation and often represents the dominant loss term in terrestrial water budgets (Oki and Kanae, 2006). It is a key variable that governs runoff, aquifer recharge, and water availability for ecosystems and society and serves as a central diagnostic variable for evaluating land-atmosphere interactions across scales (Wang and Dickinson, 2012). ET also serves as a key linkage among the water, carbon, and energy cycles (Gentine et al., 2019), and modulates weather and climate while reflecting soil moisture conditions that signal drought severity and changes in carbon and water fluxes (Katul et al., 2012). Because of these roles, accurate, spatiotemporally continuous ET mapping using medium- to moderate-resolution (~10-100 m to 250-1000 m) satellite imagery has substantial scientific and operational relevance, particularly as recent advances in satellite data availability, algorithm development, and cross-sensor

harmonization enable routine regional-to-global ET monitoring (Claverie et al., 2018; Crawford et al., 2023). Applications include defensible estimation of water availability and sectoral use, characterization of long-term climate variability and land-atmosphere processes, and improved agricultural and ecosystem management through drought monitoring and wildfire risk assessment (Fisher et al., 2017; Loveland et al., 2022; Radeloff et al., 2024; Seitzinger et al., 2026).

Despite numerous satellite-based ET models and products being available, their widespread adoption for routine decision-making by water and land management agencies, farmers, and practitioners remains uneven across decision contexts (Kumar et al., 2024). Key barriers include operational constraints, coarse spatial resolution, and inconsistent performance across land cover types. MODIS-based moderate scale ET products, including MOD16 and PML-V2 (Mu et al., 2011; Zhang et al., 2019), are widely used for regional-scale assessments; however, their relatively coarse resolution (500 m) limits applicability for field- to small watershed-scale applications, and their performance is often reduced in croplands and wetlands (McCabe and Wood, 2006).

OpenET is an operational medium-resolution Landsat-based ensemble ET product (Melton et al., 2022), which integrates six well-established remote sensing ET models, including eeMETRIC, ALEXI/DisALEXI, geeSEBAL, PT-JPL, SIMS, and SSEBop (Bastiaanssen et al., 1998; Allen et al., 2007; Fisher et al., 2008; Anderson et al., 2012; Melton et al., 2012; Senay, 2018). Owing to its high public accessibility, medium-resolution (30 m), strong performance in croplands, and operational delivery through Google Earth Engine (GEE) cloud computing (Gorelick et al., 2017), OpenET is now widely used for agricultural water use assessments by federal, state, and local agencies, consulting firms, and farmers (Ott et al., 2024; Pearson et al., 2024; Huntington et al., 2025; Martin et al., 2025; Romera and Silver, 2025; Wobus et al., 2025). However, despite its demonstrated accuracy in croplands, OpenET ensemble performance remains more variable across structurally complex natural ecosystems (Volk et al., 2024; Reitz et al., 2025). In particular, OpenET models currently exhibit greater uncertainty and systematic positive bias in forested ecosystems, which can result in poor water balance closure in forest-dominated watersheds (Khand et al., 2025; Nassar et al., 2025). Consequently, OpenET applications remain predominantly agricultural, despite considerable potential for multidisciplinary research and water resource management, further motivating the need for medium-resolution ET estimation approaches that are robust across diverse land cover types.

In many implementations, ET models scale instantaneous ET to daily and longer timescales as a function of reference ET (ETo), whereby increased atmospheric dryness enhances ETo through Penman's aerodynamic term and, in turn, increases estimated ET

(Allen et al., 2005; Allen et al., 2007; Melton et al., 2012; Senay et al., 2013). Over irrigated croplands, atmospheric dryness often results from advection of warm, dry air from surrounding arid regions, leading to increased ET that can exceed locally available radiative energy (Rana and Katerji, 2000; de Bruin et al., 2016). In contrast, over natural landscapes where advective influences are weak, atmospheric dryness largely reflects reduced ET, and elevated ETo indicates suppressed rather than enhanced ET, consistent with the complementary relationship of evaporation framework (Bouchet, 1963; Morton, 1969; Brutsaert and Stricker, 1979), which has implications for ETo-based scaling approaches. This contrast helps explain strong model performance over croplands and degraded performance over extensive natural land covers where land–atmosphere coupling is strongest. Additional uncertainties arise from neglected biomass heat storage in tall forest canopies (Lindroth et al., 2010), errors in semi-empirical aerodynamic conductance, particularly over rough forest canopies where small surface-air temperature gradients render aerodynamic conductance the primary control on sensible heat flux (Trebs et al., 2021), and the common assumption of constant evaporative fraction or ETo fraction when upscaling instantaneous ET to daily or longer time scales, which frequently breaks down (Crago and Brutsaert, 1996; Gentine et al., 2011; Cammalleri et al., 2014; Liu, 2021).

2. Objectives

Despite decades of satellite-based ET model development and continued advances in remote sensing observations, many opportunities for improvement in model structure and mechanics remain. In some settings, parsimonious frameworks with little or no reliance on satellite inputs—such as complementary relationship and surface flux equilibrium theories—have been shown to achieve performance comparable to, or in some cases exceeding, that of more complex satellite-driven approaches (Comini de Andrade et al., 2025; Thakur et al., 2025). This indicates that model structure assumptions governing land–atmospheric coupling, rather than sensor limitations alone, remain a primary constraint on medium-resolution ET performance.

Here we aim to accurately map ET at 30-m resolution across diverse land cover types while maintaining operational scalability. We introduce RADET (Radiation Advection Diffusivity–independent Evapotranspiration), a physically–based model built on four elements: (1) a diffusivity-independent flux hypothesis that yields surface energy balance closure under advection-free conditions without requiring aerodynamic conductance parameterization; (2) direct estimation of daily ET from instantaneous satellite observations, avoiding constant evaporative fraction assumptions and minimizing canopy heat storage effects; (3) separate treatment of canopy and soil components to represent distinct stomatal and soil-water controls; and (4) conditional inclusion of Penman's aerodynamic term where

advection effects are expected. We apply RADET to Landsat imagery, gridded daily meteorology, and annual land cover data, and evaluate its performance against in situ ET data and widely used satellite ET products across the conterminous United States.

3. Theoretical basis and model description

3.1. The diffusivity-independent flux hypothesis

Evaporation converts liquid water to vapor by consuming energy, generating a surface–air humidity gradient that drives vertical water vapor flux through turbulent mixing. Because aerodynamic conductance (g_a) parameterizes turbulent transport efficiency, increased mixing is often assumed to enhance ET.

However, at daily or longer temporal scales, land–atmosphere feedbacks regulate near-surface humidity gradients, and ET may become weakly sensitive to changes in g_a. Classical atmospheric boundary layer theory shows that, under spatially extensive and weakly advective conditions, ET approaches an equilibrium state independent of g_a (Slatyer and McIlroy, 1961; Priestley and Taylor, 1972; McNaughton, 1976). Accordingly, several studies explicitly define equilibrium ET as the state in which ET is independent of g_a (Monteith, 1965; Raupach, 2001). Similar assumptions arise in complementary relationship and Surface Flux Equilibrium (SFE) theory, which describe regimes where evaporation is constrained primarily by surface energy and thermodynamic feedbacks rather than turbulent transport (Morton, 1969; Brutsaert and Stricker, 1979; McColl et al., 2019). Experimental evidence indicates reduced sensitivity of evaporation to wind speed under quasi-steady conditions (Davarzani et al., 2014).

From a diffusion perspective, this behavior emerges from compensating adjustments between g_a and the vertical humidity gradient: stronger turbulent mixing reduces the gradient, whereas weaker mixing allows it to increase, yielding near-invariant ET (over a sufficient time period) despite variations in transport efficiency (Brutsaert, 1982; Salvucci and Gentine, 2013; Kim et al., 2025). Analogous behavior occurs in chemical transport and reaction systems described by Damköhler-number analysis and Sherwood-number scaling, where fluxes become reaction- or energy-limited rather than turbulent transport-limited (Levenspiel, 1999; Bird et al., 2002). Under such conditions, increases in mixing modify gradients but do not substantially increase total flux (Fig. 1). Consistent with this interpretation, the diurnal variability of ET is primarily controlled by incoming radiative energy rather than by aerodynamic mixing, a premise that underlies the common assumption of self-preserved ratios between ET and radiation in satellite-based ET models (Crago and Brutsaert, 1996).

Given these theoretical and empirical insights, daily ET under advection-free conditions can be approximated by

$$\frac{\partial ET}{\partial g_a} \approx 0 \quad (1)$$

which we refer to as the Diffusivity-Independent Flux (DIF) hypothesis. DIF assumes that surface–air thermodynamic gradients associated with phase change govern evaporation, allowing ET to be expressed without explicit parameterization of g_a. Importantly, this framework does not imply that turbulence or surface roughness are negligible; rather, their effects are implicitly embedded in the evolving humidity gradient when land–atmosphere coupling is strong.

The primary exception occurs when surfaces remain near saturation beneath dry, advective air masses (Fig. 1). In these transport-limited regimes, such as irrigated cropland, open water, wetlands, or riparian zones, humidity gradients cannot adjust, and ET increases with g_a ($\frac{\partial ET}{\partial g_a} > 0$). This behavior is consistent with the aerodynamic "drying power of the air" term in Penman's combination equation (Penman, 1948; Brutsaert and Stricker, 1979), representing departures from equilibrium evaporation.

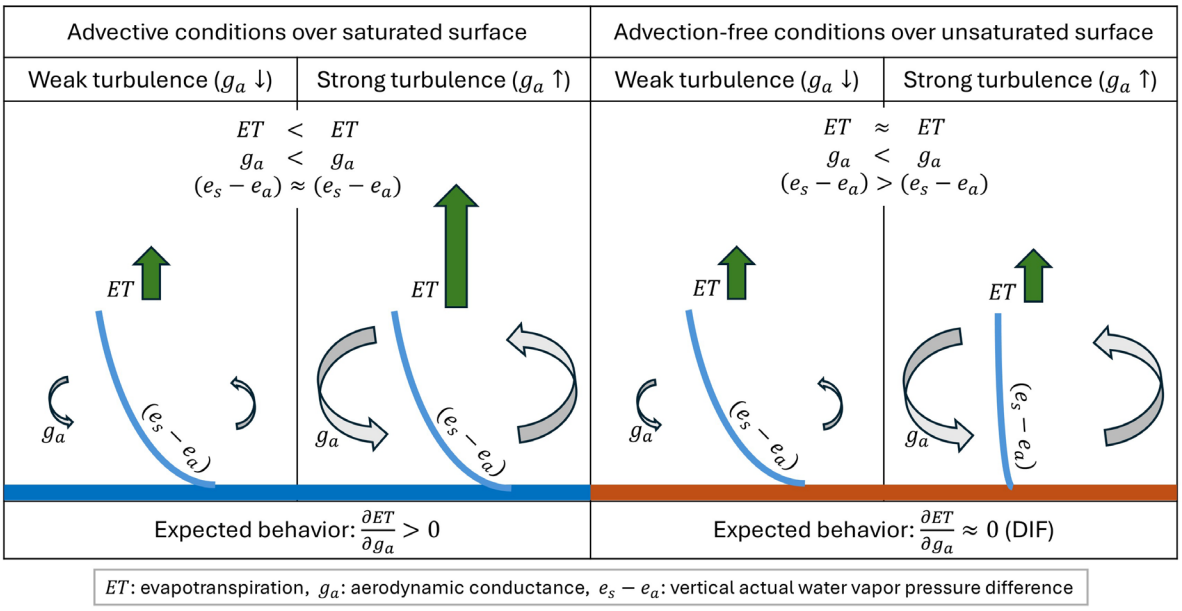

Figure 1. Conceptual schematic of the diffusivity-independent flux (DIF) hypothesis. Evapotranspiration (ET) is represented as the product of aerodynamic conductance (g_a) and vertical water vapor pressure difference (e_s-e_a). Under advective conditions, increases in g_a enhance ET through transport-limited exchange. Under advection-free conditions, enhanced turbulent mixing reduces the surface–air humidity gradient, leading to weak sensitivity of ET to g_a ($\partial ET/\partial g_a \approx 0$). The schematic illustrates the compensating

adjustment between transport efficiency and thermodynamic gradients that characterizes DIF behavior.

3.2. Evapotranspiration under the DIF hypothesis

Building on the thermodynamic invariance introduced above, the DIF constraint enables an analytical reduction of the combination equation into an equilibrium-limit form. Within this equilibrium framework, the DIF constraint acts as a thermodynamic constraint linking the combination-equation framework to equilibrium ET formulations (Monteith, 1965; Raupach, 2001). Substitution of Equation (1) into the Penman-Monteith (PM) equations yields equilibrium ET when the dependence of land surface temperature (LST) on g_a is neglected, directly linking the diffusivity-independent constraint to classical combination-equation theory. Raupach (2001) further introduced the concept of isothermal net radiation (Monteith, 1981) to eliminate explicit LST dependence from the PM formulation and obtain radiatively coupled equilibrium ET under the DIF constraint, which serves as the starting point for the present derivation.

Building on this basis, we derive an ET formulation under the DIF hypothesis in Appendices A and B. While the formulation by Raupach (2001) retains an explicit dependence on g_a, the present formulation removes this dependence by reintroducing surface temperature after application of the DIF constraint, such that g_a no longer appears in the final expression. As a result, temperature difference between surface and air emerges as a diagnostic thermodynamic constraint on equilibrium ET. This reformulation is particularly advantageous for ET modeling, as LST is directly observable from satellite remote sensing, while near-surface air temperature (T_a) fields are widely available through multiple operational mesoscale meteorological modeling and data assimilation frameworks.

Parameterizing surface water constraints using canopy conductance and soil relative humidity to represent stomatal conductance and soil surface water potential, respectively (Monteith, 1981; Kim et al., 2021), leads to distinct behavior under the DIF hypothesis (Kim et al., 2023). Accordingly, we adopt a two-source framework and apply the DIF assumption separately to canopy and soil. As derived in Appendices A and B, introducing the DIF assumption into the two-source surface energy balance yields the following analytical expression:

$$ET_{DIF} = \frac{1}{L_v}\left[\underbrace{\frac{\Delta R_{nc}}{\Delta + \mu_c\gamma}}_{canopy} + \underbrace{\frac{RH_s\Delta(R_{ns} - G)}{RH_s\Delta + \mu_s\gamma}}_{soil}\right] \quad (2)$$

where ET_{DIF} is daily ET under the DIF assumption (mm d^{-1}); L_v is latent heat of vaporization (MJ kg^{-1}); Δ is the slope of the saturation vapor pressure curve at T_a (kPa K^{-1}); γ is the

psychrometric constant (kPa K^{-1}); RH_s is the relative humidity at the soil surface (kPa kPa^{-1}); R_{nc} and R_{ns} are canopy and soil net radiation, respectively (MJ m^{-2} d^{-1}); G is the soil heat flux (MJ m^{-2} d^{-1}); and $R_{ns} - G$ is available energy at the soil surface (AE_s in MJ m^{-2} d^{-1}). Equation (2) represents a reduced form of the combination equation under the DIF constraint rather than a new empirical closure. μ_c and μ_s emerge as nondimensional canopy and soil parameters from the DIF-constrained energy balance and quantify land-atmosphere coupling strength and associated radiative–thermal departure from isothermal conditions, obtained by solving the quadratic equations (details in Appendices A and B):

$$\mu_c = \frac{R_{nci} + \sqrt{{R_{nci}}^2 + 4\frac{\Delta}{\gamma}R_{nc}(R_{nci} - R_{nc})}}{2R_{nc}} \tag{3a}$$

$$\mu_s = \frac{AE_{si} + \sqrt{{AE_{si}}^2 + 4\frac{RH_s\Delta}{\gamma}AE_s(AE_{si} - AE_s)}}{2AE_s} \tag{3b}$$

where R_{nci} is isothermal net radiation at the canopy (MJ m^{-2} d^{-1}), and AE_{si} is isothermal available energy at the soil surface (MJ m^{-2} d^{-1}). These quantities represent the hypothetical radiative state that would occur if the surface temperature equaled air temperature (Monteith, 1981) and are expressed as follows:

$$R_{nci} = R_{nc} + \rho c_p g_{Rc}(T_c - T_a) \tag{4a}$$

$$AE_{si} = AE_s + \rho c_p g_{Rs}(T_s - T_a) \tag{4b}$$

where T_c and T_s are canopy and soil radiative component temperatures derived from satellite LST (details in section 3.4.2; Appendix C); g_{Rc} and g_{Rs} are respective radiative conductances expressed in velocity units (m s^{-1}) by normalizing the linearized longwave exchange with ρc_p (details in Appendices A and B); ρ is air density (kg m^{-3}); c_p is specific heat capacity of dry air at constant pressure (MJ kg^{-1} K^{-1}).

The canopy component of ET_{DIF} aligns with conventional equilibrium ET formulations (Slatyer and McIlroy, 1961), whereas the soil component resembles SFE ET (McColl et al., 2019). A defining feature of the formulation is the emergence of μ_c and μ_s directly from the DIF-constrained energy balance rather than from prescribed conductances. μ_c and μ_s analytically reduce to unity when T_c=T_a and T_s=T_a, and exceed unity when T_c>T_a and T_s>T_a, thereby reducing ET through a thermodynamically consistent temperature-difference adjustment. Similar temperature-dependent constraints arise in alternative thermodynamic ET formulations, including Hamiltonian and maximum-entropy approaches (Liu et al., 2012; Kim et al., 2023; Pan et al., 2024), supporting the generality of the DIF hypothesis.

Notably, neither aerodynamic conductance nor surface conductance appears explicitly in Equation (2), even though the derivation begins with conductance-based formulations. Under the DIF hypothesis, together with satellite-derived surface temperature, the surface energy balance admits an analytical reduction in which aerodynamic and canopy surface conductances do not vanish physically but cancel algebraically under the DIF constraint, while remaining physically implicit through thermal gradients, yielding Equation (2) as a reduced form of the governing energy balance. Soil-surface relative humidity remains as a physical constraint but can be obtained by rearranging the soil evaporation equation (see Section 3.4.6; Appendix D), maintaining analytical closure without explicit conductance parameterization. Although μ_c and μ_s depend on radiative temperature derived from satellite LST, they implicitly represent conductance-related controls and are analogous to conductance or resistance adjustments commonly used in satellite-based two-source energy balance models (Norman et al., 1995).

3.3. The RADET model

Evapotranspiration regimes span a continuum between thermodynamically constrained equilibrium states and transport-enhanced conditions, motivating a formulation that retains the analytical structure of Equation (2) while accommodating aerodynamic forcing where appropriate. Under advective conditions, enhanced turbulent drying can shift evaporation away from equilibrium behavior (i.e., $\frac{\partial ET}{\partial g_a} > 0$). In these regimes, Equation (2) represents the equilibrium limit and may underestimate ET where advective enhancement becomes significant relative to radiative control. As illustrated in Figure 1, advective enhancement over saturated surfaces represents a primary departure from equilibrium behavior. In Appendix E, we demonstrate that once $\frac{\partial ET}{\partial g_a} \neq 0$ under advective conditions, retaining $\frac{\partial ET}{\partial g_a}$ in the derivation yields an extended formulation that preserves the structural form of Equation (2) while adding an explicit aerodynamic term.

Accordingly, we extend the ET_{DIF} formulation through the Radiation Advection Diffusivity-independent Evapotranspiration (RADET) framework, which conditionally incorporates Penman's aerodynamic term (Penman, 1948), thereby recovering a reduced combination-equation form consistent with classical Penman–Monteith lineage.

$$ET_{RAD} = ET_{DIF} + \delta_{LC}\delta_{WET}\frac{\gamma f(u) VPD_a}{\Delta + \gamma} \quad (5)$$

where δ_{LC} is a nondimensional parameter, representing a land cover modulation of aerodynamic enhancement, and δ_{WET} is a nondimensional wetness parameter. Their

product activates Penman's aerodynamic contribution, where *f(u)* is the empirical wind function and VPD_a is the vapor pressure deficit at the reference height (kPa).

Because the physically derived aerodynamic term of Penman (1948) represents enhanced turbulent drying associated with regional-scale advection (de Bruin et al., 2016), Equation (5) extends the DIF formulation into transport-influenced regimes while preserving the equilibrium-limit structure of Equation (2), such that aerodynamic forcing acts as a perturbation to the DIF equilibrium solution rather than introducing an independent conductance parameterization, maintaining consistency with equilibrium-based interpretations of land–atmosphere exchange rooted in complementary relationship theory (Brutsaert and Stricker, 1979; Brutsaert, 1982). Land cover classification, fractional vegetation cover, and soil moisture and temperature limitations represented through δ parameters modulate the magnitude of aerodynamic enhancement under conditions conducive to advection. Further details on δ parameters and the wind function are provided in Section 3.4.8.

3.4. Satellite derived parameters for RADET

The analytical formulation introduced above is implemented using medium-resolution satellite remote sensing observations combined with gridded meteorological data. The present implementation focuses on Landsat observations and the gridMET meteorological dataset, although the framework is sensor-agnostic and transferable to other satellite sensors and meteorological products.

3.4.1. Daily land surface temperature

The instantaneous radiative land surface (skin) temperature observed by the Landsat satellite and the daily minimum air temperature ($T_{a,min}$) from gridMET are used to estimate the daily mean land surface temperature (LST_{daily}). Here, land surface temperature is interpreted as the thermodynamic radiative temperature that links satellite observations to surface energy balance constraints, rather than as a bulk aerodynamic temperature (Brutsaert, 1982). Following common boundary layer assumptions, the minimum land surface temperature (LST_{min}) is approximated as slightly lower than $T_{a,min}$, as frequently observed across various environments (Good, 2016), reflecting nocturnal radiative cooling under weak turbulent mixing.

$$LST_{min} \approx T_{a,min} - offset \tag{6}$$

The offset is set to 1 K, representing a small empirical adjustment rather than a universal physical constant. Next, the maximum land surface temperature (LST_{max}) is estimated using a cosine-based diurnal reconstruction function (Göttsche and Olesen, 2001).

$$LST_{max} = LST_{min} + \frac{LST_{10am} - LST_{min}}{\cos\left(\frac{\pi}{2} \cdot \frac{10 - t_{max}}{t_{max} - t_{min}}\right)} \quad (7)$$

where LST_{10am} is the Landsat satellite observed land surface temperature around 10:00; t_{max} is the peak time of land surface temperature, assumed to occur at 12:30, consistent with a representative clear-sky diurnal cycle; and t_{min} is the local sunrise time (i.e., time corresponding to LST_{min}).

The daily mean land surface temperature is then calculated as:

$$LST_{daily} = \frac{LST_{min} + LST_{max}}{2} \quad (8)$$

If the estimated LST_{daily} from Equation (8) is lower than the gridMET daily mean air temperature ($T_{a,daily}$), LST_{daily} is set equal to $T_{a,daily}$ to prevent unrealistically cold surface states under weak land–atmosphere coupling.

The daily outgoing longwave radiation (LW_{out}, MJ m^{-2} d^{-1}) is computed using the Stefan-Boltzmann law:

$$LW_{out} = \varepsilon \sigma LST_{daily}^{\ 4} \quad (9)$$

Here, LST_{daily} is expressed in Kelvin and represents the radiative temperature governing longwave emission, $\sigma (= 4.901 \times 10^{-9})$ is the Stefan-Boltzmann constant (MJ K^{-4} m^{-2} d^{-1}), and ε is emissivity from Landsat emissivity band.

This approach was evaluated against in situ outgoing longwave radiation measurements from flux tower sites (Figure S1). The results indicate that the coefficient of determination (R^2) exceeds 0.9 across all land cover types, with slopes near unity, indicating strong consistency between predicted and observed LW_{out}.

3.4.2. Daily canopy and soil surface temperature

To apply the DIF formulation within a two-source energy balance framework, the daily radiative temperature is partitioned into canopy and soil components consistent with radiative transfer and surface energy balance constraints. We estimate the daily mean canopy surface temperature ($T_{c,daily}$) and soil surface temperature ($T_{s,daily}$) from LST_{daily}. In the two-source energy balance (TSEB) framework, these temperatures at an instantaneous satellite overpass are related through the fractional vegetation cover observed at the sensor's view angle (Norman et al., 1995). However, because our analysis is based on daily averaged LST, which represents the hemispheric outgoing longwave radiative temperature, we express this relationship using the daily longwave transmissivity (τ_L). Under the assumption of equal emissivity for canopy and soil surfaces, the daily mean radiometric

temperature can be expressed as the sum of the outgoing longwave radiation from the two components:

$$LST_{daily}{}^4 = (1 - \tau_L)T_{c,daily}{}^4 + \tau_L T_{s,daily}{}^4 \quad (10a)$$

$$\tau_L = \exp(-\kappa_L LAI) \quad (10b)$$

where *LAI* is leaf area index, and κ_L is the extinction coefficient for longwave, set to 0.95, which is equivalent to the extinction coefficient for diffuse radiation (Kustas and Norman, 1999).

In Equations (10a) and (10b), both LST_{daily} and *LAI* can be derived from Landsat optical and thermal observations (details in sections 3.4.1 and 3.4.5). However, $T_{c,daily}$ and $T_{s,daily}$ remain unknown unless an additional constraint is introduced. To address this, we introduce a constraint derived from the ET_{DIF} (see Appendix C), which links canopy surface temperature to LST_{daily} and $T_{a,daily}$. This additional constraint is expressed as follows:

$$T_{c,daily} = T_{a,daily} + \beta(LST_{daily} - T_{a,daily}) \quad (11a)$$

$$\beta = \frac{f_c}{f_c + \frac{\mu_s}{\mu_c}\frac{\Delta + \mu_c\gamma}{RH_s\Delta + \mu_s\gamma}(1 - f_c)} \quad (11b)$$

$$f_c = 1 - \exp(-0.4LAI) \quad (11c)$$

where β is a parameter that controls the degree to which canopy surface temperature departs from LST_{daily}, and f_c is canopy fraction and represents the fraction of net radiation absorbed by the canopy, estimated as in Equation (11c) (Norman et al., 1995). The parameter β acts as a weighting factor that adjust canopy temperature. When β approaches 1, the canopy surface temperature remains close to LST_{daily}. Conversely, when β approaches 0, the canopy surface temperature converges to the overlying air temperature.

We first estimate $T_{c,daily}$ using Equation (11a) and then substitute the result into Equation (10a) to obtain $T_{s,daily}$. However, the resulting $T_{s,daily}$ can occasionally become unrealistically high. To avoid this issue, we compute an upper bound for $T_{s,daily}$ by assuming that the net radiation at the soil surface cannot be negative:

$$\varepsilon\sigma T_{s,daily}{}^4 \leq \tau_S SW_n + \tau_L LW_{atm} + (1 - \tau_L)\varepsilon\sigma T_{c,daily}{}^4 \quad (12)$$

where τ_S is the daily shortwave transmissivity, SW_n is the daily net shortwave radiation (MJ m^{-2} d^{-1}) and LW_{atm} is incoming longwave radiation MJ m^{-2} d^{-1}.

If estimated $T_{s,daily}$ violates Inequality (12), we set $T_{s,daily}$ to its upper limit based on the right-hand side of Inequality (12).

3.4.3. Daily net radiation

Consistent with the radiative skin-temperature framework introduced above, daily net radiation is derived from Landsat optical and thermal observations combined with gridded meteorological forcing. Daily net shortwave radiation (SW_n) is expressed as:

$$SW_n = SW_{in}(1 - \alpha) \tag{13}$$

where SW_{in} is the gridMET daily incoming solar radiation (MJ m^{-2} d^{-1}), and α is Landsat-derived broadband albedo (Liang, 2001). The effective shortwave transmissivity follows Beer's law:

$$\tau_S = \exp(-\kappa_S LAI) \tag{14}$$

where $\kappa_S = 0.56$ represents a representative extinction coefficient across diverse ecosystems (Zhang et al., 2014).

Incoming longwave radiation (LW_{atm}) is estimated using the Stefan–Boltzmann law with an effective atmospheric emissivity:

$$LW_{atm} = \varepsilon_{atm}\sigma {T_{a,daily}}^4 \tag{15a}$$

$$\varepsilon_{atm} = \varepsilon\left[1 - \left(1.35\frac{SW_{in}}{R_{so}} - 0.35\right)\left(0.34 - 0.14\sqrt{e_a}\right)\right] \tag{15b}$$

following Allen et al. (2005), where R_{so} is the calculated clear-sky radiation (MJ m^{-2} d^{-1}) and $T_{a,daily}$ is expressed in Kelvin. Daily mean air temperature is used to maintain thermodynamic consistency with the radiative temperature framework used to compute LW_{out} (Equation 9).

Net radiation partitioning between canopy and soil components, assuming equal emissivity and albedo, is expressed as:

$$R_{nc} = (1 - \tau_S)SW_n + (1 - \tau_L)[LW_{atm} + \varepsilon\sigma {T_{s,daily}}^4 - 2\varepsilon\sigma {T_{c,daily}}^4] \tag{16a}$$

$$R_{ns} = \tau_S SW_n + \tau_L LW_{atm} + (1 - \tau_L)\varepsilon\sigma {T_{c,daily}}^4 - \varepsilon\sigma {T_{s,daily}}^4 \tag{16b}$$

$$R_n = R_{nc} + R_{ns} \tag{16c}$$

where R_n is net radiation (MJ m^{-2} d^{-1}). Evaluation against flux-tower observations (Figure S2) shows slightly lower skill than outgoing longwave radiation (R^2 ranges from 0.66 to 0.85), likely reflecting uncertainties in incoming radiation estimates, yet indicating physically consistent and operationally robust net radiation retrievals.

3.4.4. Daily soil heat flux

At daily time scales, net soil heat storage is generally small relative to available energy because daytime conductive warming is largely offset by nocturnal release of subsurface heat. Accordingly, the daily mean soil heat flux G (MJ m^{-2} d^{-1}) is estimated as:

$$G = 0.35R_{ns} - 1.5 \quad (17)$$

The first term in Equation (17) links daytime soil heat flux to soil net radiation (Norman et al. (1995), while the constant offset represents compensating nocturnal conductive release. Its magnitude is selected so that median daily soil heat flux approaches zero, consistent with weak net ground heat storage at daily time scales.

3.4.5. Leaf Area Index

Leaf area index (LAI) is estimated using the Landsat two-band Enhanced Vegetation Index (EVI2) (Jiang et al., 2008). EVI2-based LAI has demonstrated improved agreement with in situ observations and has been widely applied in satellite-based ET modeling (Kang et al., 2016; Jaafar et al., 2022). The formulation follows:

$$LAI_{EVI2} = (2.92\sqrt{EVI_2} - 0.43)^2 \quad (18)$$

where LAI_{EVI2} is constrained within [0,8] (Jaafar et al., 2022).

Vegetation index-based LAI may be overestimated over artificial green surfaces, so the normalized difference moisture index (NDMI) (Gao, 1996) is used to scale LAI when NDMI becomes negative:

$$LAI = LAI_{EVI2}NDMI_{scaled} \quad (19a)$$

$$NDMI_{scaled} = \frac{NDMI - NDMI_{min}}{0 - NDMI_{min}} \quad (19b)$$

$NDMI_{scaled}$ is constrained within [0,1]. Based on the typical NDMI range, $NDMI_{min} = -0.3$ (Gao, 1996). For actively transpiring vegetation, NDMI is typically positive and LAI remains unchanged, whereas negative NDMI values reduce spuriously high LAI estimates over non-vegetated surfaces. This LAI estimate defines canopy radiative transmissivity and thereby links radiometric temperature decomposition to canopy–soil partitioning of net radiation.

3.4.6. Soil surface relative humidity

Introducing the DIF hypothesis ensures mathematical closure of the soil surface energy balance without requiring additional parameterizations of soil surface relative humidity (RH_s). Accordingly, rearranging the soil evaporation component of ET_{DIF} yields an analytical expression for RH_s (see Appendix D for derivation):

$$RH_s = \frac{e_a}{e^*(T_a) + \Delta(T_s - T_a)\frac{\mu_s - 1}{\mu_s}} \quad (20)$$

When $\mu_s \to 1$, corresponding to strong land–atmosphere coupling, RH_s reduces to the atmospheric relative humidity (i.e., $\frac{e_a}{e^*(T_a)}$). Conversely, as $\mu_s \to \infty$, RH_s approaches $\frac{e_a}{e^*(T_s)}$. Equation (20) therefore constrains RH_s between $\frac{e_a}{e^*(T_a)}$ and $\frac{e_a}{e^*(T_s)}$, with μ_s governing the transition between these states. The estimated RH_s from Equation (20) is applied across all land cover types, except open water, for which RH_s is set to 1.

3.4.7. Computational procedure for ET_{DIF}

Partitioning *LST* into canopy and soil temperatures introduces a weak dependency on μ_c and μ_s. Similarly, estimation of RH_s depends on μ_s. Rather than iterating toward numerical convergence, ET_{DIF} is solved through a diagnostic closure in which μ_c and μ_s are evaluated under fully coupled conditions (μ_c=μ_s=1), yielding an initial estimate of T_c, T_s, RH_s, and energy balance. The thermodynamic state is then used to update μ_c and μ_s, after which the final ET_{DIF} solution is obtained. Additional updates produce negligible changes in ET, reflecting the second-order influence of μ_c and μ_s on daily radiative temperature partitioning; accordingly, a single diagnostic adjustment is sufficient.

3.4.8. Parameters for the aerodynamic term

The aerodynamic modulation term in Equation (5) is represented through land-cover and surface wetness factors that describe conditions under which advective enhancement becomes dynamically relevant. The indicator δ_{LC} identifies land-cover classes where surface–atmosphere coupling and advective exchanges are expected to be strong, following USGS NLCD classifications.

$$\delta_{LC} = \begin{cases} 1, & LC \in \{\text{cultivated, open water, wetland, woody wetland with LAI<1}\} \\ 0, & LC \notin \{\text{cultivated, open water, wetland, woody wetland with LAI<1}\} \end{cases} \quad (21)$$

The surface wetness factor δ_{wet} in is expressed as:

$$\delta_{WET} = f_c + (1 - f_c) f_{sm} f_{sT} \quad (22a)$$

$$f_{sm} = RH_s^{\,VPD_s} \quad (22b)$$

$$f_{sT} = \frac{1}{1 + e^{10 - LST_{soil} + 273.15}} \quad (22c)$$

where f_{sm} and f_{sT} represent soil moisture and temperature limitations.

Increasing canopy fraction f_c, derived from NDMI-constrained LAI (Equation 19), reflects a larger fraction of actively transpiring vegetation. Over sparsely vegetated surfaces (1-f_c), wetness is regulated independently through soil humidity and thermal state, with f_{sm} estimated from RH_s and soil surface vapor pressure deficit (VPD_s) following Fisher et al. (2008). Because near-saturation conditions at low temperature may otherwise inflate wintertime fluxes, a sigmoidal soil temperature limitation f_{sT} is introduced, conceptually consistent with García et al. (2013).

Aerodynamic transport is represented using the traditional empirical wind function of Penman (1948)

$$f(u) = 2.6(1 + 0.54u_2) \quad (23)$$

where u_2 is windspeed at 2 m height (m s^{-1}) and contributes to the aerodynamic drying term ($\frac{\gamma f(u) VPD_a}{\Delta+\gamma}$) in Equation (5) consistent with complementary relationship formulations and Penman-type frameworks (Comini de Andrade et al., 2025).

3.4.9. Topographic effects

To represent topographic influences on near-surface meteorological forcing, elevation-dependent adjustments were applied to daily air temperature and incoming solar radiation within RADET. Minimum and maximum air temperatures from gridMET were downscaled using elevation differences between the 30 m SRTM topography (Farr et al., 2007) and 4 km gridMET surface with a dry adiabatic lapse rate of −6.5 K km^{-1}, producing terrain-consistent daily air temperature fields that maintain thermodynamic coherence with the radiative temperature framework used throughout the model.

Topographic modulation of surface shortwave radiation was incorporated to account for slope and aspect effects. Daily solar radiation on inclined terrain was estimated using the analytical integrated formulations of Allen et al. (2006), which partition global radiation into direct, diffuse, and reflected components. Consistent with the analytical simplifications adopted in RADET, differences in direct-beam transmissivity between sloped and horizontal surfaces were neglected.

These adjustments provide terrain-consistent temperature and radiative forcing while preserving analytical continuity with the radiative surface temperature energy balance framework. Neighborhood shadowing and terrain-induced modifications to local air temperature are not explicitly resolved and therefore represent a higher-order source of uncertainty in complex terrain.

3.5. Temporal interpolation for monthly RADET

The RADET model directly estimates daily ET and therefore does not require instantaneous-to-daily scaling. However, estimates are available only on Landsat overpass dates (8–16 day intervals), with additional gaps during cloud contamination; temporal interpolation is applied to derive temporally continuous daily and monthly ET. Many Landsat-based ET frameworks interpolate normalized evaporative metrics between image dates. Five of the six OpenET models interpolate the ratio of ET to ASCE reference ET (ETo) (Allen et al., 2005), expressed as the fraction of ETo (EToF) (crop coefficient). In these approaches, EToF is typically interpolated using piecewise linear schemes and subsequently multiplied by ETo to obtain daily ET. The ALEXI/DisALEXI framework adopts an analogous strategy but substitutes incoming shortwave radiation for ETo. While ETo-based interpolation performs well under advective conditions over well-watered surfaces, regional-scale analyses often reveal complementary behavior between ET and evaporative demand (Bouchet, 1963; Brutsaert and Stricker, 1979).

Consistent with this thermodynamic perspective, RADET adopts a radiation-based interpolation similar to ALEXI/DisALEXI, using the ratio between ET and incoming shortwave radiation as the scaling variable. Radiation-based scaling has demonstrated performance comparable to alternative schemes (Brutsaert and Sugita, 1992; Cammalleri et al., 2014) Sensitivity tests using fractions of ETo, potential shortwave radiation, net radiation, SFE ET, and Priestley-Taylor ET produce noticeable differences at daily scales but only marginal differences at monthly scales because biases compensate through temporal aggregation. For operational scalability while reducing sensitivity to errors in ETo or alternative scaling variables that can otherwise introduce potentially large interpolation biases (Blankenau et al., 2020; Volk et al., 2026), incoming shortwave radiation is adopted, providing a parsimonious yet physically consistent interpolation pathway. Under this formulation, temporal interpolation follows the evolution of available energy rather than prescribed evaporative demand, thereby maintaining consistency with the radiative control implicit in the DIF framework.

4. Methods

4.1. RADET inputs and application

The RADET model was applied to estimate ET at 30 m resolution across selected regional domains and at 145 flux tower locations used solely for evaluation and intercomparison, providing a common spatial and observational basis for model assessment. Primary inputs to the RADET model are summarized in Table 1. The analysis period spans 2000–2020 and uses Landsat 5, 7, and 8 Collection 2 Level-2 optical and thermal products (US Geological Survey, 2021; Crawford et al., 2023). Landsat-derived albedo, EVI2, and NDMI were

computed in GEE (Gorelick et al., 2017). For comparisons with flux tower measurements, land surface temperature, emissivity, albedo, EVI2, and NDMI were extracted by spatially averaging pixels within 7 × 7 (210 x 210 m) Landsat-grid static- footprints around each flux tower to approximate the effective source. (Volk et al., 2024)Details on flux tower sites and the 7 × 7 footprint approach, including its comparable performance relative to dynamic other footprint methods, are provided in Volk et al. (2023a).

Daily meteorological forcing was obtained from the gridMET dataset (Abatzoglou, 2013). The required variables include specific humidity, minimum and maximum air temperature, downward shortwave radiation, and wind speed at 10 m height. Air pressure required for vapor pressure calculations is not provided by gridMET and was therefore estimated from SRTM elevation following the ASCE PM formulation (Allen et al., 2005) using standard atmospheric assumptions. Wind speed at 10 m height provided by gridMET was adjusted to 2 m height for input to the Penman wind function following the ASCE PM formulation (Allen et al., 2005).

Land cover information was obtained from the annually updated USGS NLCD dataset (US Geological Survey, 2024), accessed through the Awesome GEE Community Catalog (Roy et al., 2025) and extracted for each flux tower location to provide a consistent characterization of advective regimes and surface states across all sites.

Table 1 Primary inputs to the RADET model.

Data (sources)	Native spatial resolution (temporal scale)	Primary usage	References
Land surface temperature (Landsat-5, 7 & 8)	60 – 120 m (instantaneous)	Canopy and soil surface temperature	US Geological Survey (2021)
Surface reflectance (Landsat-5, 7 & 8)	30 m (instantaneous)	Albedo, EVI2, and NDMI	US Geological Survey (2021)
Solar radiation, specific humidity, minimum and maximum air temperature, wind speed (gridMET)	4 km (daily average)	Meteorological forcing for the RADET model	Abatzoglou (2013)
Elevation (SRTM)	30m (constant)	Estimating air pressure, terrain adjustment air temperature and solar radiation	Farr et al. (2007)
Land cover (USGS NLCD)	30 m (annually updated constant)	Identifying advective conditions	US Geological Survey (2024)

4.2. OpenET data

We used OpenET ET estimates (Melton et al., 2022; Collection 2.0) to evaluate RADET relative to the six OpenET models and the ensemble value. OpenET daily (overpass-dates) and monthly time series were taken from the benchmark dataset compiled for the OpenET Intercomparison and Accuracy Assessment (Volk et al., 2024). In that analysis, OpenET pixels were sampled at flux towers using flux footprints: temporally dynamic footprints based on (Kljun et al., 2015) when site parameters were available (about half of the sites) and otherwise using static Landsat-grid footprints (typically 7 × 7) shifted slightly to capture the dominant source area based on day-time wind direction. (Volk et al., 2024)

For RADET, we sampled pixels around each flux tower using the static 7 × 7 Landsat grids that were developed by (Volk et al., 2023a) because this approach was readily available for the data processing workflow. The prior analysis on footprint method comparisons indicated that the 7 × 7 static grids generally overlap the dynamic footprints on average (74% daily and 83% monthly true-positive overlap). Due to those results and previous comparisons of OpenET using different footprint methods, the impacts on aggregate statistics (highlighted in this study) based on 7 ×7 vs dynamic footprints should be modest. At a subset of sites with heterogeneous land cover where OpenET used dynamic or smaller gridded footprints, the differences may be more important.

4.3. MODIS based ET products

We additionally evaluated RADET against ET products derived from the Moderate Resolution Imaging Spectroradiometer (MODIS), which provide coarser (~1 km) spatial resolution but higher temporal sampling through daily observations aggregated into 8-day ET composites providing an independent satellite-based benchmark with contrasting spatial–temporal scaling. Specifically, we used the MOD16 ET Collection 6.1 product, MOD16A2GF v6.1 (Running et al., 2021), and the PML-V2 v0.1.8 ET dataset (Zhang et al., 2019) extracted from GEE at the central pixel of each flux tower footprint. The 8-day ET values were then redistributed to daily values using uniform allocation and aggregated to monthly totals to maintain temporal consistency with RADET outputs and OpenET comparisons.

A recent study by Endsley et al. (2025) introduced an updated and recalibrated MOD16 formulation anticipated for MODIS Collection 7. We obtained the corresponding 8-day ET products directly from the authors; however, these data relied on Collection 6.1 FPAR/LAI inputs rather than Collection 7. To ensure consistency and avoid calibration bias, comparisons were limited to the same 61 flux tower sites used by Endsley et al. (2025), excluding sites used in MOD16 calibration or validation thereby maintaining independence between calibration and evaluation datasets.

4.4. In situ ET data

To evaluate RADET model performance, we used in situ flux measurements as a benchmark reference dataset. Specifically, we employed the dataset compiled by Volk et al. (2023b), which aggregates ET measurements across the contiguous United States (CONUS) from multiple sources, including AmeriFlux, USDA-ARS, and USGS NWSC. This dataset was also used for OpenET performance assessment (Volk et al., 2024) ensuring methodological consistency across model evaluations.

Most of the sites employ the eddy covariance method, while a smaller number rely on Bowen ratio systems or weighing lysimeters. After excluding sites with fewer than five paired ET observations (daily RADET and in situ ET overlaps) during the study period, 145 sites remained for analysis. These comprise 54 cropland, 16 evergreen forest, 27 grassland, 13 mixed forest, 26 shrubland, and 9 wetland/riparian sites (Figure 2).

The eddy covariance method is subject to a systematic uncertainty known as the energy balance imbalance, wherein the sum of turbulent heat fluxes is typically lower than the available energy (Mauder et al., 2020). For model evaluation, we used both energy balance ratio (EBR)–corrected data (results presented in the main text) and EBR–uncorrected data (results provided in the Supplementary Information) to bracket uncertainty. The EBR correction was applied using the Bowen ratio preservation method (Twine et al., 2000; Volk et al., 2023a).

For daily-scale performance assessments, we used quality-controlled, gap-free daily ET observations. Only satellite overpass days were considered, and gap-filled or negative in situ ET values were excluded. To ensure consistency with OpenET models, we included only paired records where RADET estimates, in situ ET observations, and OpenET values were all available for the same day.

For monthly-scale assessments, gap-filled in situ ET data were included. Monthly data were used only when the number of gap-filled days did not exceed five (Volk et al., 2024). While this strict criterion ensures consistent comparison with OpenET, it can exclude many records during rainy months, periods that typically exhibit high ET in water-limited ecosystems such as shrublands. Therefore, as a secondary monthly benchmark, we applied a relaxed criterion requiring at least five observed days per month. This benchmark was used solely to evaluate RADET performance sensitivity and was not used for direct comparison with OpenET models to preserve methodological comparability.

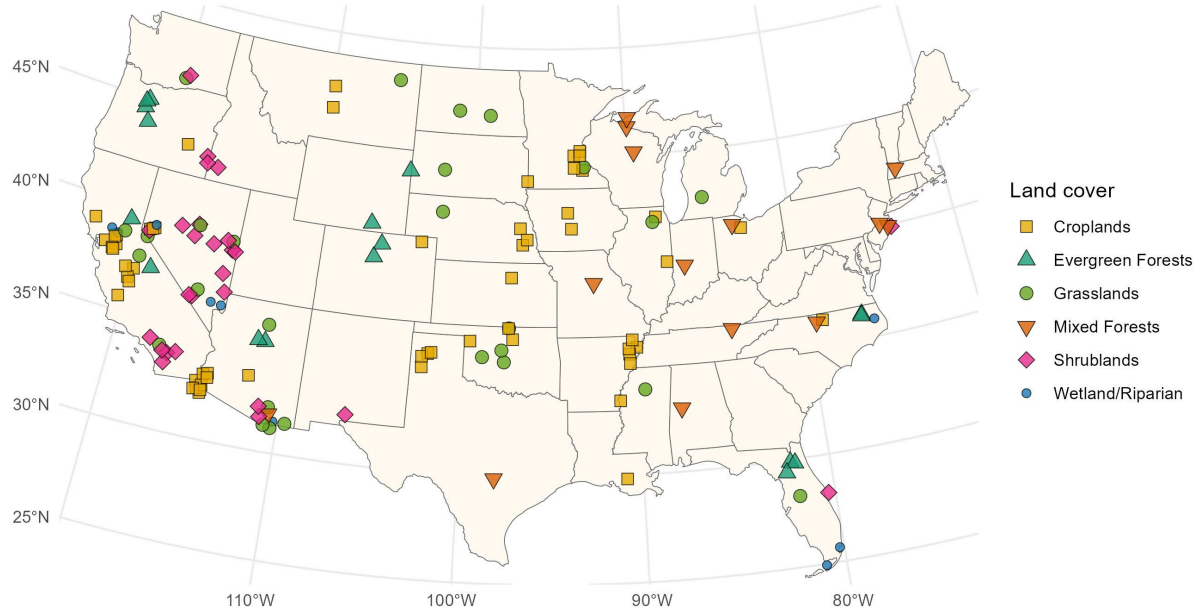

631

632 **Figure 2** Map of in situ ET measurement sites. Symbol color and shape indicates land cover
633 type. The exact site locations are slightly jittered to reduce overlap among closely spaced
634 points.

635 ### 4.5. Model evaluations

636 Building on the theoretical derivation, we first evaluated the RADET model using a
637 hierarchical framework. Model behavior was first examined diagnostically relative to the
638 SFE model ($ET = \frac{1}{L_v}\frac{RH\Delta(R_n-G)}{RH\Delta+\gamma}$) (McColl et al., 2019), to diagnose the influence of the DIF
639 constraint and aerodynamic enhancement within an equilibrium thermodynamic reference
640 context. The SFE model is an equilibrium-based ET formulation dependent on available
641 energy and meteorological forcing (McColl et al., 2019), and often performs comparably to
642 more complex satellite-based ET models (Thakur et al., 2025). We used the same
643 meteorological and satellite inputs for the SFE model as for ET_{DIF} and RADET. Specifically,
644 net radiation (Equation 16c) and soil heat flux (Equation 17) were applied in the SFE
645 calculation to ensure a fair comparison between the SFE and the proposed approach.

646 Model skill was then assessed at daily and monthly timescales through intercomparison
647 with OpenET models and their ensemble value, followed by evaluation against MODIS-
648 based ET products for multi-scale benchmarking across independent datasets.

649 We employed statistical metrics, including Kling-Gupta Efficiency (KGE), Nash–Sutcliffe
650 Efficiency (NSE), Root Mean Square Error (RMSE), Mean Absolute Error (MAE), and Mean
651 Bias Error (MBE). One-to-one comparisons additionally report the coefficient of

determination (R^2) and the least-squares regression slope constrained through the origin to emphasize proportional bias (detailed equations in Appendix F).

Following the OpenET accuracy assessment (Volk et al., 2024), daily accuracy statistics were calculated without gap-filled station ET data for all models, while monthly statistics included only stations with five or fewer gap-filled days per month. Land cover group statistics relied on flux site metadata classification rather than NLCD classifications.

For each flux station, RMSE, MAE, MBE, and NSE were computed individually and then aggregated using a weighted mean. Individual-site KGE and NSE values were constrained within the range of [–1, 1] consistent with the bounded interpretation adopted in Reitz et al. (2025). KGE and NSE were calculated only for sites with a minimum of five paired observations. Group-level statistics were weighted by the square root of the number of paired observations per station following Volk et al. (2024) to balance station influence while preventing long record sites from dominating aggregation metrics.

For comparison with MOD16, we followed the approach of Endsley et al. (2025) by restricting the evaluation to the same 61 flux-tower sites used in their MOD16–OpenET intercomparison, grouping records into cropland and non-cropland categories, and computing performance statistics directly from the pooled paired observations to ensure direct comparability with published MOD16 performance metrics.

5. Results

5.1. Theoretical evaluation of RADET

The performance of the proposed ET_{DIF} formulation (Equation 2) and the RADET model (Equation 5) was first evaluated at the daily timescale for Landsat overpass days through comparison with the SFE model (McColl et al., 2019) using identical available energy and meteorological inputs (Figure 3 for EBR-corrected evaluations and Figure S3 for EBR-uncorrected evaluations). The SFE formulation provides a thermodynamic reference baseline relying solely on available energy and meteorological forcing.

Figure 3 shows that ET_{DIF} generally outperforms the SFE model, even though the two share similarities in their formulations. The SFE model typically underestimates ET under high-ET conditions and overestimates ET when ET is low (Kim et al., 2023; Thakur et al., 2025). ET_{DIF} effectively addresses these systematic deviations, particularly for land cover types where advection is not expected ($\delta_{LC} = 0$). The μ terms reduce ET below equilibrium when LST exceeds air temperature, mitigating positive biases at low ET, while the two-source treatment increases ET with increasing vegetation cover, reflecting a higher equilibrium evaporative fraction of canopy relative to soil.

However, ET_{DIF} still exhibits substantial biases when $\delta_{LC} = 1$, where strong advection can violate the DIF hypothesis. These biases are reduced in RADET, which conditionally incorporates Penman's aerodynamic term when advective enhancement is expected ($\delta_{LC} = 1$). The hierarchical progression from SFE to ET_{DIF} and ultimately RADET is observed consistently for both EBR-corrected (Figure 3) and uncorrected data (Figure S3). These results demonstrate improved agreement with in situ flux observations when aerodynamic enhancement is represented within the RADET framework while preserving thermodynamic consistency.

Together, the progression from equilibrium behavior toward transport-influenced regimes establishes the physical basis for subsequent intercomparisons with in situ flux observations across land cover classes and with operational satellite-based ET products at daily and monthly scales, which build directly on the equilibrium-to-transport framework demonstrated here.

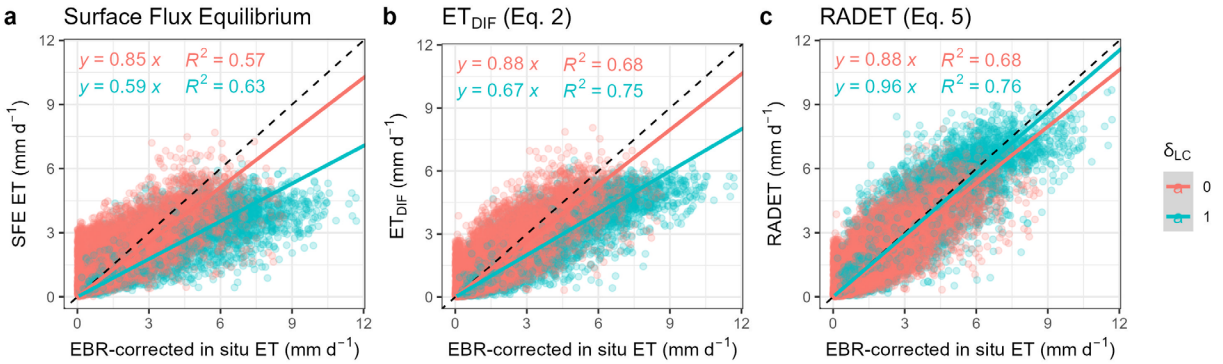

Figure 3 In situ ET observations versus estimated daily ET using the SFE (a), ET_{DIF} (b) and RADET (c) models. Observed ET represents energy balance ratio (EBR)-corrected data. The dashed line indicates the 1:1 line, and point colors differentiate advection-prone land covers ($\delta_{LC} = 0$) from less advection-prone land covers ($\delta_{LC} = 1$) (Equation 21). R^2 and the least-squares linear regression forced through the origin are shown (solid line).

5.2. Daily RADET evaluation

The RADET model was evaluated for Landsat satellite overpass days using only paired RADET–in situ ET observations (see Methods). One-to-one comparisons are shown in Figure 4 (EBR–corrected) and Figure S4 (EBR–uncorrected).

Across all land cover types, R^2 exceeded 0.62 and the regression slopes were slightly below unity when evaluated against the EBR-corrected benchmark. Using the EBR-uncorrected benchmark, R^2 values decreased modestly and slopes generally around unity. Performance is strongest over croplands and mixed forests (slopes of 0.96 and 0.97; R^2 = 0.76 and 0.80), consistent with OpenET models (Volk et al., 2024). Evergreen forests, grasslands, and

shrublands also show strong correspondence (slopes of 0.9–0.93; R^2 = 0.62–0.66), notable given known challenges for medium-resolution ET models over these ecosystems (Volk et al., 2024). Wetland/riparian sites retain relatively high explanatory power (R^2 = 0.68) but exhibit the lowest slope (0.79).

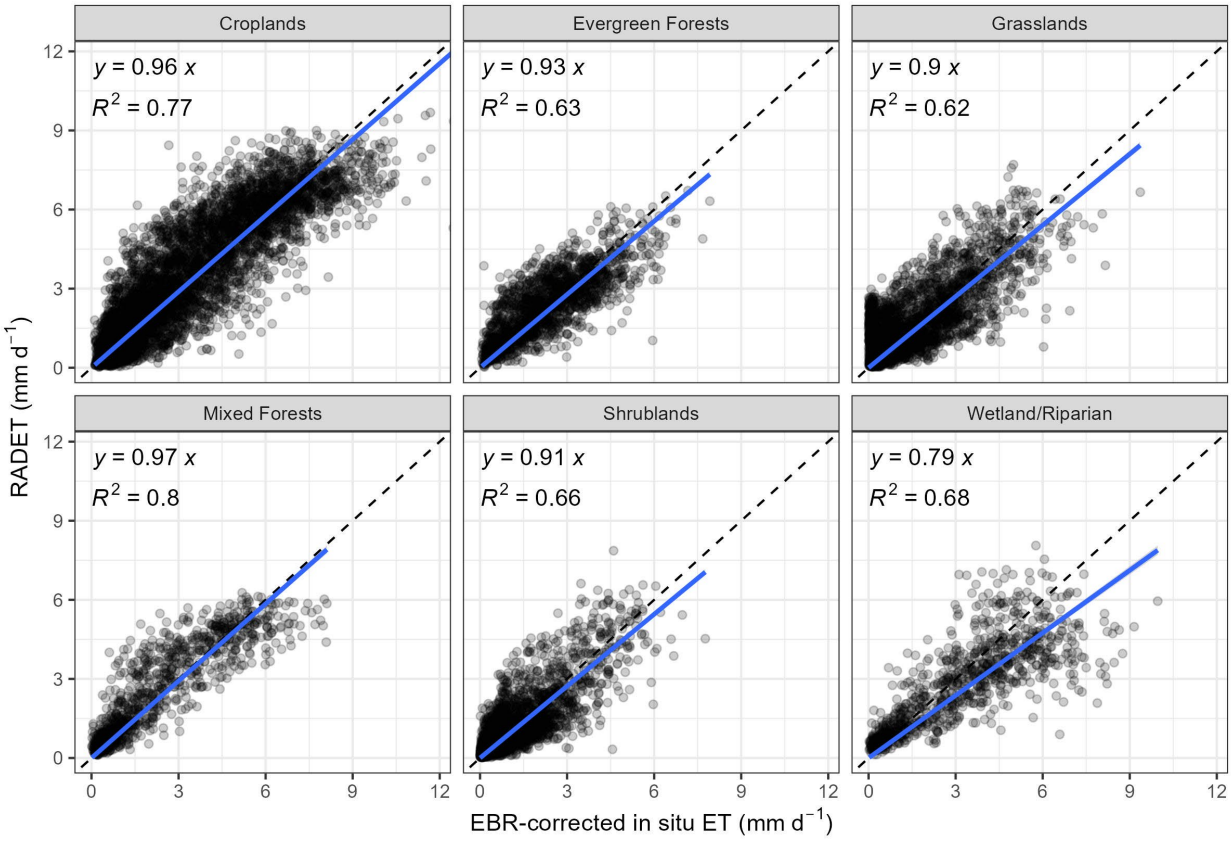

Figure 4 Daily RADET versus in situ ET observations grouped by land cover type based on site metadata (not NLCD classification). Observed ET represents energy balance ratio corrected data. For each land cover group, R^2 and the least-squares linear regression forced through the origin are shown.

5.2.1 Comparison with OpenET models

Next, RADET was compared with individual OpenET models and their ensemble value. For daily analysis, the SIMS model was excluded because it does not account for soil evaporation (Melton et al., 2022; Volk et al., 2024). Figure 5 summarizes the error statistics using EBR–corrected in situ ET, while Figure S5 shows EBR–uncorrected results. Overall, RADET matches or exceeds OpenET model performance across all land cover types and benchmarks.

In croplands, RADET shows performance similar to the best OpenET model under the EBR–corrected benchmark, while substantially reducing the negative bias commonly observed

in OpenET models. Subtype analysis (Figure S6) indicates strongest performance in annual crops and orchards. In vineyards, however, RADET tends to overestimate in situ ET, whereas previous studies reported stronger OpenET performance (Volk et al., 2024).

When the EBR–uncorrected benchmark is used, RADET's performance becomes similar to that of the OpenET models in croplands, primarily due to a larger positive bias (Figure S5). However, the eddy covariance technique does not capture horizontal advection (Mauder et al., 2020), which increases surface energy imbalance particularly over irrigated croplands and potentially introduces low bias in in situ ET when EBR correction is not applied (Volk et al., 2023a).

For evergreen forests, mixed forests, grasslands, and shrublands, RADET consistently outperforms all OpenET models and their ensemble across statistical metrics. This result is consistent for both EBR–corrected and uncorrected benchmarks. Improvements are particularly strong over evergreen forests and shrublands, where OpenET models exhibited negative NSE values, with NSE = 0 marking the transition from useful to noise-dominated simulations (Duc and Sawada, 2023), whereas RADET NSE values remained positive. Although higher thresholds (e.g., NSE > 0.5) are common in streamflow modeling with large observational variance (N. Moriasi et al., 2007), NSE > 0 is a more appropriate signal-to-noise benchmark, particularly under low-variance conditions such as shrubland ET (Duc and Sawada, 2023). Similar results are seen for KGE, where values around 0.5 indicate the transition from signal to noise dominance, with an ideal score of 1 (Gupta et al., 2009; Duc and Sawada, 2023). OpenET models also show a pronounced positive bias in evergreen forests, which is substantially reduced by the RADET model.

The stronger performance of RADET across structurally complex vegetation appears consistent with its DIF-constrained two-source formulation. Multi-layered and complex canopies introduce radiative-aerodynamic decoupling, internal energy storage, and persistent shading, conditions known to bias bulk single-source energy balance formulations (Brutsaert and Sugita, 1992; Norman et al., 1995; Kustas and Norman, 1999). By resolving canopy and soil energy pathways separately based on the DIF constraint and incorporating aerodynamic enhancement only when advection is expected, RADET reduces systematic deviations associated with bulk surface representations. While DisALEXI also adopts a two-source framework, its reliance on semi-empirical aerodynamic conductance formulations may introduce larger uncertainties than the DIF constraint, particularly over rough forest surfaces, potentially contributing to the performance differences observed here.

For the Wetland/Riparian group, RADET performs comparably to the OpenET models under the EBR-corrected benchmark, with a negative bias apparent for RADET. Figure S6

indicates that RADET underestimates in situ ET at most riparian sites but not wetlands, primarily because the advection term is not applied where riparian areas are not classified as wetlands in the USGS NLCD dataset. Future improvements may include alternative or combined land cover datasets to better represent riparian conditions and associated advective enhancement.

Performance across cropland and natural ecosystems at in situ flux sites provides context for the scene-scale comparisons presented below, which illustrate how differences among model predictions appear spatially across contrasting landscapes.

To examine the spatial pattern of these improvements, Figure 6 illustrates the difference in KGE between RADET and the OpenET ensemble. Although the ensemble provides a representative reference, the proposed RADET model generally improves performance at sites located in natural ecosystems, with occasional degradation in rainfed or deficit irrigation croplands (e.g., vineyards in California).

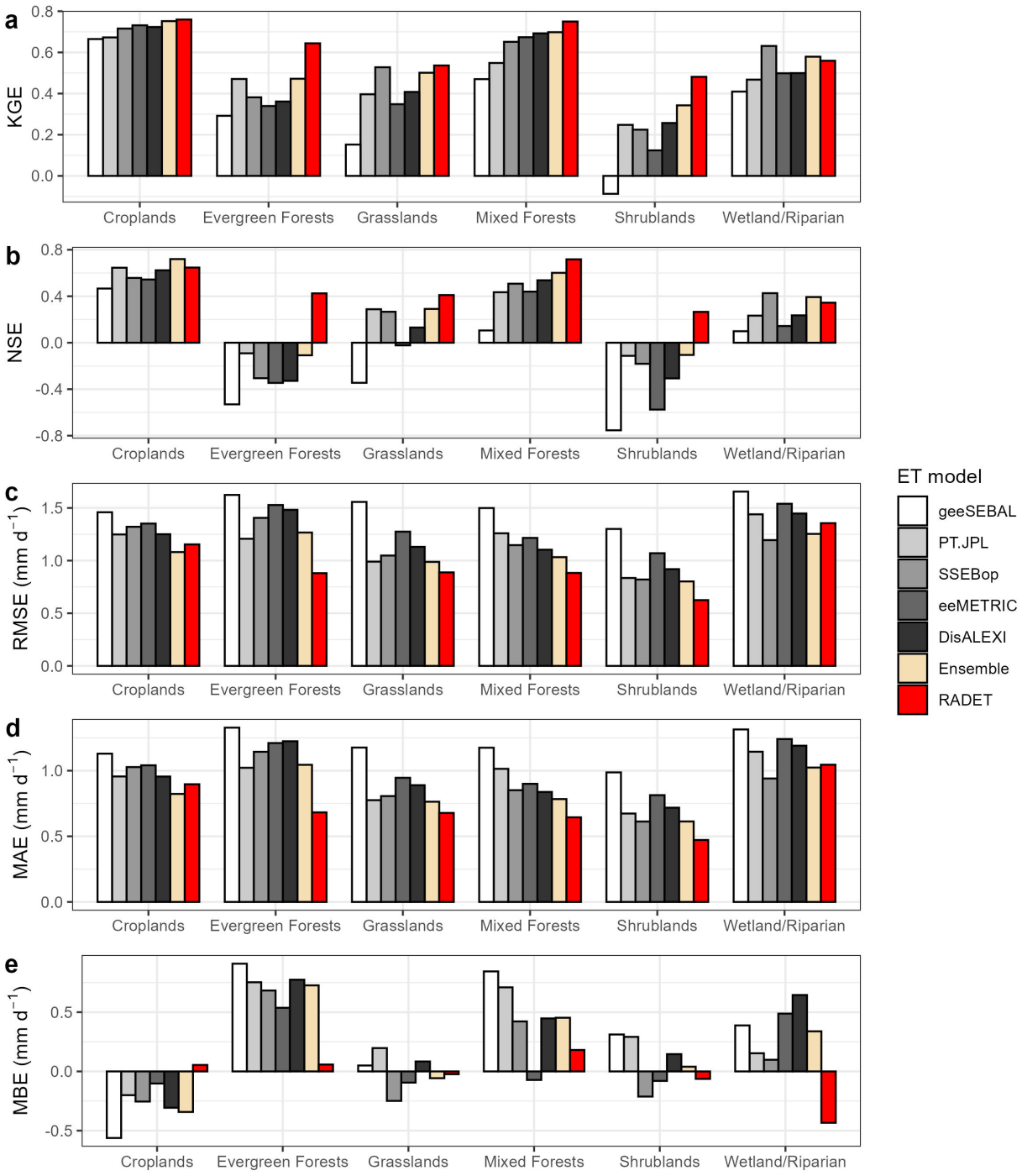

782

783 **Figure 5** Comparison of daily error statistics between RADET and OpenET models, grouped
784 by land cover type. Model evaluations were performed using EBR–corrected in situ ET as
785 the benchmark.

786

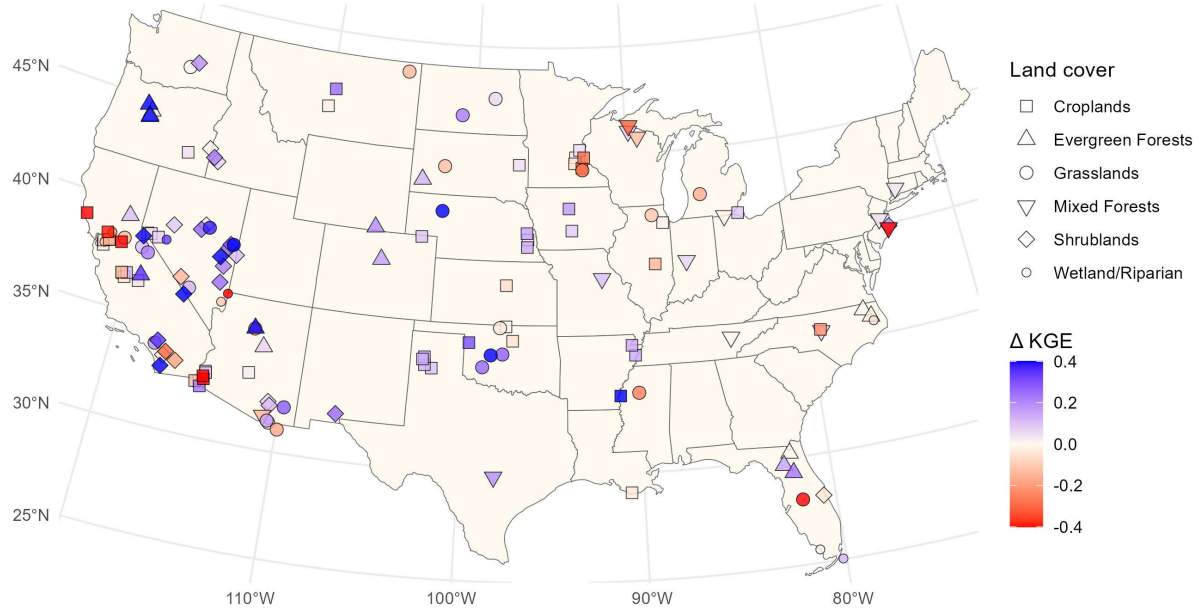

787

788 **Figure 6** Spatial distribution of Kling–Gupta Efficiency (KGE) differences between RADET
789 and the OpenET ensemble at the daily scale (KGE based on EBR-corrected benchmark).
790 Blue indicates improved agreement with in situ ET, whereas red indicates reduced
791 performance relative to the ensemble reference. Values exceeding ±0.4 were truncated to
792 constrain the color scale. Point shapes denote land cover classes, and site locations were
793 slightly offset to reduce overlap.

794 ### 5.2.2 Special case studies

795 As RADET showed improved performance over evergreen forests and shrublands, two
796 representative Landsat scenes were examined: one containing four flux sites located in
797 evergreen forests in Oregon (Figure 7), and another containing two shrubland sites and one
798 grassland site in Nevada (Figure 8).

799 The first scene (Landsat 8; July 26, 2024) covers the Metolius River region in Oregon (Figure
800 7), characterized by a pronounced west-east gradient from dense evergreen forest to
801 shrubland, including forest clearings and localized cropland near the corridor, providing a
802 spatial context for interpreting model behavior across structurally complex, predominantly
803 energy-limited canopies. Four flux tower sites (US-Me1, US-Me2, US-Me5, US-Me6) are
804 located within the scene. Both RADET (Figure 7a) and the OpenET ensemble (Figure 7b)
805 resolve land cover transitions at 30 m resolution, although OpenET generally produces
806 higher ET over evergreen forests. Flux observations indicate RADET agrees more closely
807 with observations (e.g., KGE = 0.64 vs. 0.32 for the OpenET ensemble; Figure S7a), primarily
808 due to reduced positive bias.

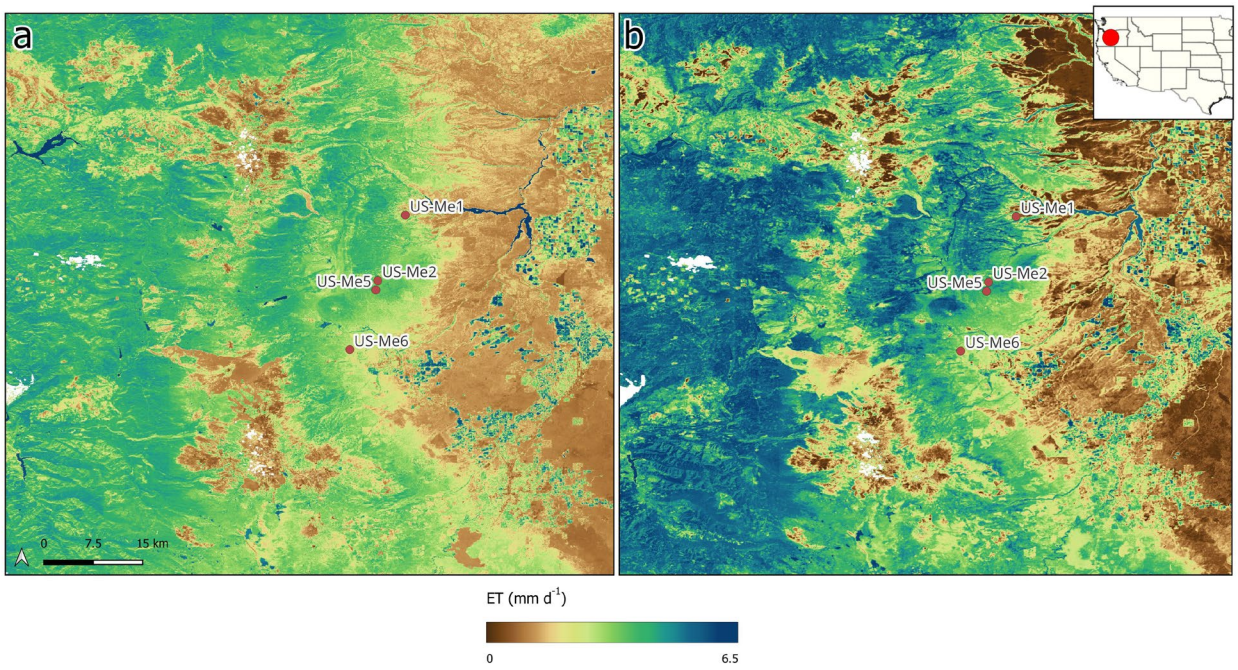

Figure 7. Daily ET estimated by (a) RADET and (b) the OpenET ensemble for a Landsat 8 scene acquired on July 26, 2024, in central Oregon near the Metolius River. The four red markers denote evergreen forest flux towers US-Me1, US-Me2, US-Me5, and US-Me6. White areas indicate cloud masking.

The second scene (Landsat 8; July 14, 2023) spans the semi-arid Spring Valley region of eastern Nevada (Figure 8), including two shrubland sites (SV-5, SV-6) and one grassland site (SPV-3). The scene is characterized by strong elevational gradients spanning low-elevation semi-arid shrubland and localized cropland in the central–eastern valley floor to structurally complex mountain canopies within predominantly water-limited landscapes where equilibrium assumptions and aerodynamic enhancements may diverge. Across extensive shrublands, the OpenET ensemble produces ET values close to zero, whereas RADET yields higher estimates consistent with flux observations. Agreement with in situ ET improves substantially (e.g., KGE = 0.71 for RADET vs. 0.43 for the OpenET ensemble; Figure S7b) largely by reducing underestimation bias.

Together, Figures 7 and 8 illustrate how differences among model formulations emerge across contrasting hydroclimatic and structural regimes, providing spatial context for the statistical improvements observed in flux-tower evaluations while maintaining consistency with the equilibrium-to-transport transition reflected in the progression from the DIF formulation to the RADET framework. Although inference beyond the scenes shown here remains limited, qualitative inspection of additional scenes with contrasting landscapes, including locations where OpenET struggles to accurately estimate ET, indicated that RADET performs reasonably well, consistent with the flux site statistical metrics presented

herein. Figures S8–S10 illustrate these challenging cases, where the OpenET ensemble exhibits artifacts over developed, volcanic, or salt-crusted surfaces, whereas RADET substantially reduces these errors.

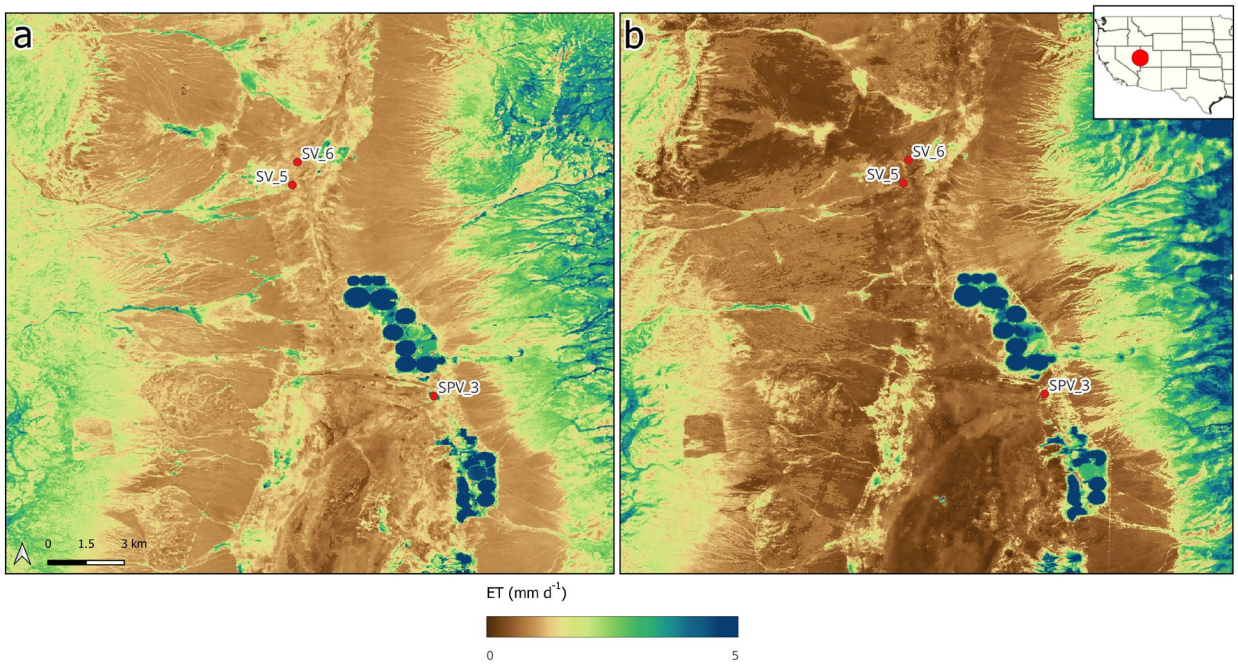

Figure 8. Daily ET estimated by (a) RADET and (b) the OpenET ensemble for a Landsat 8 scene acquired on July 14, 2023 in Spring Valley, Nevada. The three red markers denote flux towers SV-5, SV-6 (shrubland) and SPV-3 (grassland).

5.3 Monthly RADET evaluation

We evaluated monthly RADET performance using one-to-one comparisons between RADET and in situ ET observations (Figure 9: EBR–corrected; Figure S11: EBR–uncorrected). Two EBR-corrected benchmarks were considered: a strict quality-control criterion (≤ 5 gap-filled days) and a relaxed criterion (≥ 5 observed days). For the EBR–uncorrected comparison, only the strict criterion was applied because the gap-filling scheme of (Volk et al., 2023a) applies exclusively to EBR–corrected ET data.

For the EBR–corrected benchmark under the relaxed criterion, RADET achieved R^2 values exceeding 0.7 across all land cover types, with regression slopes close to unity. Croplands showed slightly improved performance under the strict criterion, whereas some dry ecosystems showed the opposite behavior. For example, shrubland R^2 decreased from 0.76 under the relaxed criterion to 0.68 under the strict criterion. This likely reflects removal of precipitation-driven high ET months that were retained in the relaxed benchmark and well captured by RADET. The EBR–uncorrected benchmark showed comparable R^2 values but generally higher regression slopes.

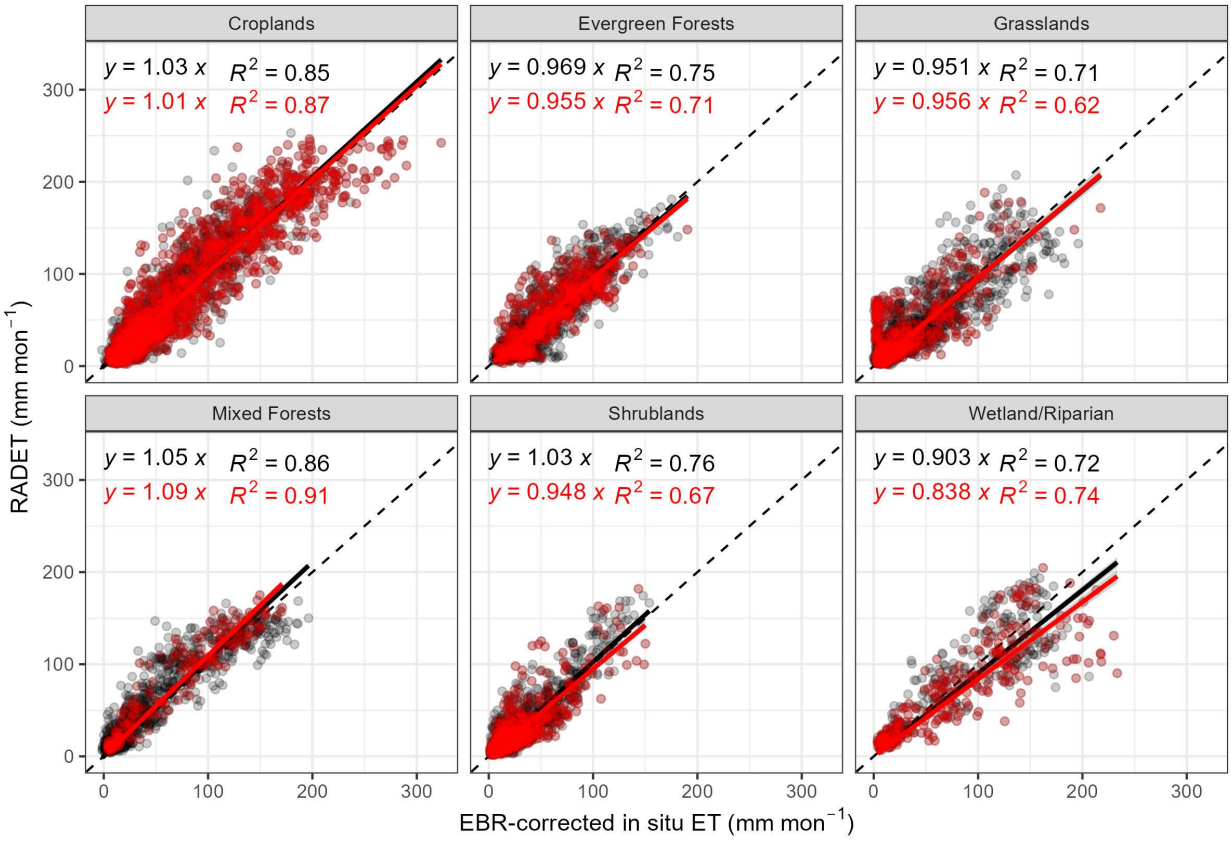

Figure 9 Monthly RADET versus in situ ET observations grouped by land cover type. Observed ET represents EBR corrected data. Red points indicate results under the strict benchmark criterion (≤5 gap-filled days), while black points indicate the relaxed benchmark criterion (≥5 observed days). For each land cover group, R^2 and the least-squares linear regression forced through the origin are shown.

5.3.1 Comparison with OpenET models

To assess model differences at an aggregated time scale, RADET performance was compared with individual OpenET models and their ensemble value at the monthly scale. Figure 10 summarizes error statistics using EBR–corrected in situ ET, and Figure S12 shows EBR-uncorrected results. Also, Figure 11 illustrates the difference in KGE between RADET and the OpenET ensemble, and one-to-one comparisons with in situ ET are provided in Figures S13–S18. Overall, RADET performs comparably to or better than OpenET across land covers and benchmarks, consistent with the daily scale evaluation.

For croplands, RADET performs similarly to the best OpenET model under the EBR-corrected benchmark but shows reduced skill under the EBR-uncorrected benchmark, reflecting known energy balance closure limitations of in situ measurements under advective conditions in irrigated croplands.

Across other land cover types, including evergreen forests, mixed forests, grasslands, and shrublands, RADET consistently yields the strongest performance metrics. Improvements are particularly pronounced in evergreen forests and shrublands. In shrublands, monthly NSE values were generally negative for all models, primarily because observed ET exhibits very low temporal variability, causing NSE to penalize even small absolute errors. However, RADET maintains positive NSE values, indicating improved sensitivity to subtle month-to-month changes. When evaluated using EBR-uncorrected data, NSE values for the OpenET models remain mostly negative across all natural land cover types, whereas RADET remains positive.

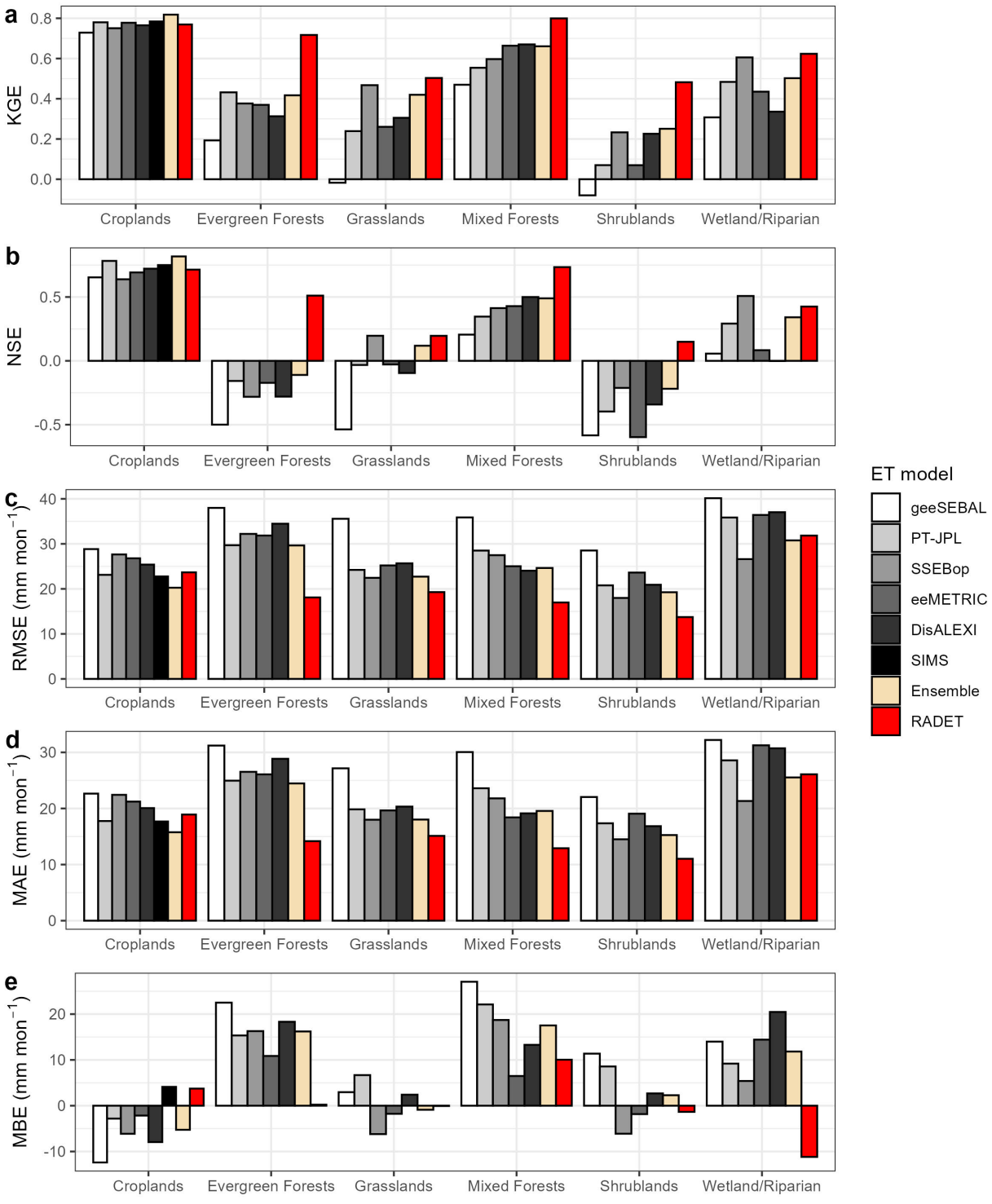

881

882 **Figure 10.** Monthly error statistics for RADET and OpenET models grouped by land cover
883 type. Model evaluations use EBR–corrected in situ ET under the strict quality-control
884 criterion (≤5 gap-filled days). Statistics summarize performance across flux tower sites and
885 provide context for spatial patterns shown in Figure 11. The SIMS model is included only for
886 croplands because it produces ET estimates exclusively over cropland areas.

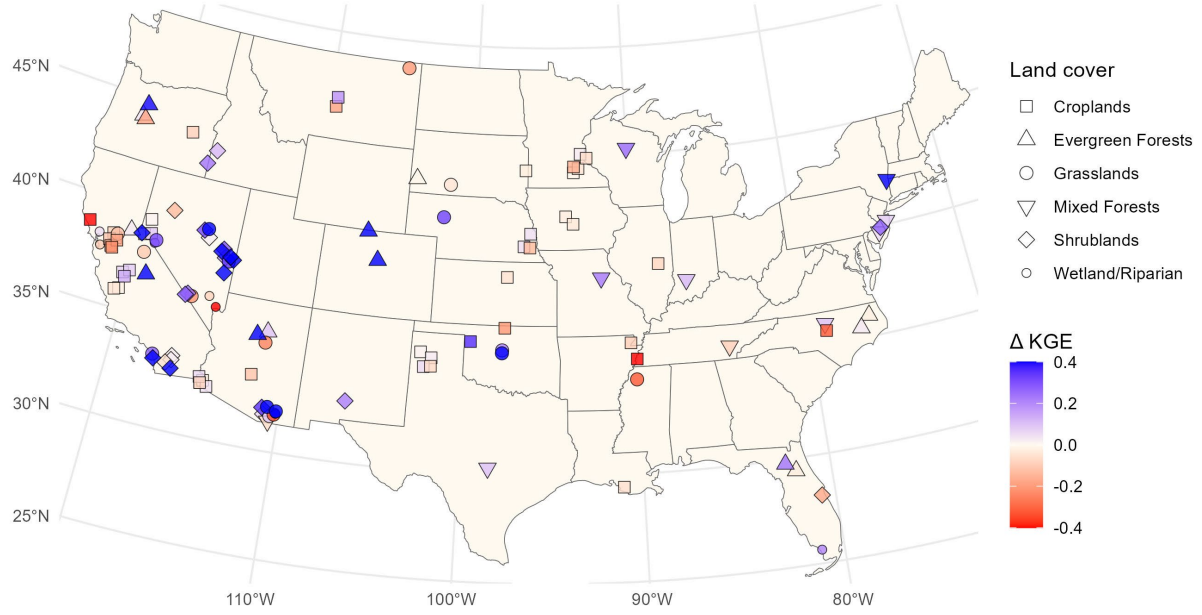

Figure 11 Spatial distribution of KGE differences between RADET and the OpenET ensemble at the monthly scale. Blue indicates improved agreement with in situ ET, whereas red indicates reduced performance relative to the ensemble reference. Values exceeding ±0.4 were truncated to constrain the color scale. Point shapes denote land cover classes, and site locations were slightly offset to reduce overlap.

5.3.2 Comparison with MODIS-based models

We evaluated the monthly performance of RADET against the PML-V2 product, the current operational MOD16 Collection 6.1 ET product, and the recently updated MOD16 version anticipated for MODIS Collection 7 (Table 2). Following the MOD16–OpenET intercomparison framework of Endsley et al. (2025), we used the same set of 61 flux tower sites and computed performance metrics from pooled cropland and non-cropland records without site-level weighting, ensuring methodological consistency. These sites were not used for MOD16 calibration, preserving independence. It is noted that our reproduction of the Endsley et al. (2025) statistics showed minor numerical differences, likely due to additional filtering associated with inclusion of RADET and PML-V2 datasets.

Among the MODIS-based products, PML-V2 and the updated MOD16 version performed substantially better than the operational MOD16 Collection 6.1 for croplands and non-croplands, consistent with previous evaluations (Zhang et al., 2019; Endsley et al., 2025). Despite these improvements, RADET maintained the strongest overall performance. Over croplands, RADET reduced error magnitude and bias relative to all MODIS-based products,

while over non-cropland sites RADET exhibited equal or improved agreement relative to the more advanced MODIS formulations.

Table 2. Monthly performance metrics for RADET, the OpenET ensemble, PML-V2, operational MOD16 Collection 6.1, and the updated MOD16 (anticipated Collection 7). Metrics follow the Endsley et al. (2005) evaluation framework using 61 flux tower sites. Results are summarized separately for croplands and non-cropland sites.

	Model	RMSE (mm mon^{-1})	MBE (mm mon^{-1})	Correlation	KGE
Croplands	RADET	24.7	+4.6	0.93	0.87
	OpenET Ensemble	19.1	-6.9	0.96	0.90
	PML-V2	36.0	-16.2	0.86	0.53
	C6.1 MOD16	51.6	-29.9	0.76	-0.08
	C7 MOD16	34.2	-13.0	0.86	0.61
Non-crop	RADET	19.4	+4.5	0.91	0.84
	OpenET Ensemble	28.2	+8.7	0.84	0.70
	PML-V2	24.2	-0.52	0.84	0.84
	C6.1 MOD16	26.3	-8.23	0.81	0.68
	C7 MOD16	24.6	+3.1	0.83	0.81

Together, daily and monthly scale flux comparisons, OpenET intercomparisons, and MODIS-scale evaluations show that the progression from equilibrium behavior toward conditionally enhanced transport in RADET produces internally consistent performance gains across spatial and temporal scales, particularly within water-limited natural ecosystems. These cross-scale results provide a physically grounded context for interpreting model behavior, operational considerations, limitations, and potential future improvements discussed below.

6 Discussion

6.1. As simple as possible, but no simpler

The RADET formulation maintains physical realism while reducing structural complexity relative to conventional medium-resolution surface energy balance ET models. Because RADET is grounded in the equilibrium and DIF hypothesis framework (Raupach, 2001) and conceptually analogous to reaction-limited and transport-controlled regimes described by classical diffusion and transport theory (Levenspiel, 1999; Bird et al., 2002), it does not require aerodynamic conductance or surface conductance parameterizations. Such

parameters often introduce semi-empirical calibration and canopy-dependent uncertainty (Polhamus et al., 2013; Trebs et al., 2021; Mallick et al., 2022). The DIF constraint enables a compact analytical solution without site-specific tuning.

Computational demands remain modest because explicit iterative energy balance closure is not required (Allen et al., 2007; Anderson et al., 2012) nor coupled conductance solving (Mallick et al., 2014). In Figure S19, we compare the runtime of RADET with OpenET models across multiple scenes in GEE and find that its runtime is comparable to PT-JPL. Because PT-JPL is one of the most computationally efficient models within the OpenET ensemble, this result highlights RADET's efficiency and strong potential for large-scale operational implementation.

Despite this numerical simplicity, RADET retains mechanistic process representation. Its two-source and radiatively coupled equilibrium formulation informed by optical and thermal remote sensing, and the conditional inclusion of Penman's aerodynamic term extend equilibrium formulations into regimes where transport effects become important (Figure 3).

6.2 Spatial-temporal resolution constraints

Satellite ET retrievals typically balance spatial detail against revisit frequency. Medium-resolution sensors (10–100 m; e.g., Landsat, Sentinel-2) provide spatial heterogeneity, whereas moderate-resolution sensors (250 m–1 km; e.g., MODIS, VIIRS) provide more frequent observations and temporal continuity. In heterogeneous croplands, medium-resolution thermal and optical data capture field-scale contrasts effectively (Radeloff et al., 2024), and medium-resolution energy balance models often outperform coarse ET products (Endsley et al., 2025). Conversely, moderate- to coarse-resolution products frequently perform well over homogeneous natural ecosystems, where canopy and atmospheric controls dominate (Chen and Liu, 2020). Frequent sampling reduces temporal interpolation error, providing an advantage in forests, grasslands, and shrublands.

RADET partially relaxes this conventional trade-off particularly in natural land covers. Despite relying solely on Landsat revisit intervals, RADET matches the best OpenET models in croplands and exceeds MODIS-based products across natural ecosystems at monthly timescales. The results suggest that accurate physical representation can partially compensate for reduced temporal sampling density.

Medium-resolution ET enables detection of fine-scale disturbances, heterogeneous vegetation, and small watershed hydrologic processes such as ET from riparian systems and groundwater dependent ecosystems (e.g., Figures 7 and 8) (Radeloff et al., 2024). Within the context of medium-resolution remote sensing applications, models that

preserve spatial detail without sacrificing physical consistency remain essential; RADET addresses need by maintaining skill across agricultural and natural systems at 30 m resolution using a framework based on established energy balance, thermodynamic, and transport theory.

6.3 Room for Improvement and Future Applications

Despite strong performance, several limitations remain. First, the current implementation relies on land cover classification and δ-based wetness indicators to determine advective enhancement. For example, several riparian sites were not labeled as wetlands in the NLCD, resulting in the aerodynamic term not being applied and leading to ET underestimation (Figure S6). Conversely, RADET tended to overestimate ET at vineyard sites, likely because deficit irrigation reduces actual ET (Volk et al., 2024), while advective enhancement was triggered based on land cover classification (Figure S6). Our qualitative inspection of RADET scenes over rainfed croplands and adjacent forested areas in the eastern US suggests potential artifacts associated with the advection term over croplands when the surrounding environment is not dry. Future improvements could include incorporating irrigation status information (Ketchum et al., 2020; Xie and Lark, 2021) explicitly identifying valley bottom, riparian corridors, and wetlands (Gilbert et al., 2016; US Fish & Wildlife Service, 2018; Woodward et al., 2018), or developing thermally and soil moisture derived advection diagnostics.

Second, Landsat revisit intervals require temporal interpolation. Testing indicated modest sensitivity among interpolation strategies, but temporal interpolation remains a key component, particularly prior to 2000. Physically informed interpolation frameworks (Riba et al., 2025) may further reduce sampling error. Also, although RADET is demonstrated here with Landsat data, the framework is sensor-agnostic. Integration with Harmonized Landsat–Sentinel (HLS) data and downscaled VIIRS–HLS products (Xue et al., 2020; Jaafar et al., 2022) could increase revisit frequency, while higher-resolution thermal missions (e.g., ECOSTRESS, Hydrosat, TRISHNA) may further improve performance and spatial detail.

Third, the physical realism of RADET can be further improved. The current framework does not explicitly represent open-water heat storage, which could be addressed explicitly (Zhao et al., 2024). The soil heat flux sub-model may also be refined, particularly over bare soil where its contribution is significant. In addition, snow processes, such as latent heat of sublimation, could be incorporated in the next version. Also, testing across tropical forests, coastal regions, and strongly advective environments, where DIF assumptions may weaken, would help identify additional areas for improvement.

RADET shows operational potential due to its compact formulation and modest computational demand (Figure S19). The open-source Python pipeline and configuration of RADET align with OpenET architecture, supporting transparency, reproducibility, and scalable deployment (https://github.com/DRI-RAD/radet-beta). Applications extend beyond irrigation accounting to water balance assessment, groundwater dependent ecosystems, drought monitoring, and regional hydrology. Performance gains across forested and shrubland systems highlight potential for water availability assessments. Future work should include watershed-to-basin scale water balance evaluations to assess hydrologic consistency (Khand et al., 2025).

7 Conclusion

Medium-resolution remote sensing for ET estimation has advanced rapidly, and several practical products have emerged in recent years. However, as highlighted by Radeloff et al. (2024), a major remaining challenge is developing formulations that maintain physical consistency and accuracy across contrasting land cover types and hydroclimatic regimes Currently available approaches generally struggle to achieve this balance. This study introduces RADET, a medium-resolution ET model designed to address this gap by providing physically constrained and skillful ET estimates across diverse environments.

RADET is grounded in a thermodynamically constrained equilibrium framework and applies aerodynamic enhancement when equilibrium assumption breaks down under advective conditions. The model demonstrates consistent performance improvements in natural land cover types relative to existing medium-resolution models that rely on Landsat data and moderate-resolution products based on MODIS that benefit from more frequent revisit intervals. This performance is achieved without any land cover calibration or iterative computations that are common in many surface energy balance models, reducing structural complexity and computational demand while maintaining physical interpretability.

Several directions remain for future work. These include refining advection detection and land-surface classification assumptions, extending and testing RADET beyond CONUS, applying the formulation to additional satellite sensors, and generating fully operational products. At the same time, future studies should explore the practical advantages of RADET. By providing stable cross-scale ET estimates at medium-resolution, RADET enables new analyses of heterogenous landscapes, including improved water resources assessment and management. Advancing RADET toward broader real-world application will require continued evaluation across climatic gradients, integration with multi-sensor

data streams, and demonstration of operational value within medium-resolution ET frameworks.

Findings from this study suggest that satellite-based equilibrium formulations with conditional transport enhancement can provide physically consistent ET estimates across spatial and temporal scales, establishing a reproducible and transparent pathway for medium-resolution ET modeling, intercomparison, and operational deployment.

CRediT authorship contribution statement

Yeonuk Kim: Conceptualization, Data curation, Formal analysis, Investigation, Methodology, Software, Validation, Visualization, Writing-original draft; **Justin L Huntington**: Conceptualization, Funding acquisition, Methodology, Investigation, Resources, Supervision, Writing-original draft, Writing-review & editing; **Bruno Comini de Andrade:** Data curation, Formal analysis, Investigation, Methodology, Software, Validation, Writing-review & editing; **Mark S Johnson:** Conceptualization, Methodology, Supervision, Writing-review & editing; **John M Volk**: Data curation, Investigation, Resources, Writing-review & editing; **Sayantan Majumdar**: Investigation, Software, Visualization, Writing-review & editing; **Charles Morton:** Data curation, Resources, Software, Writing-review & editing; **Peter ReVelle**: Investigation, Writing-review & editing

Data availability

The open-source Python implementation of the RADET model can be found at https://github.com/DRI-RAD/radet-beta. All input data used for RADET are publicly available through the Google Earth Engine Data Catalog (https://developers.google.com/earth-engine/datasets/catalog) and the Awesome GEE Community Catalog (https://gee-community-catalog.org/). R scripts used for intercomparisons and statistical analysis, and Earth Engine Compute Unit (EECU)/runtime analysis Python scripts and outputs are available at https://github.com/DRI-RAD/radet-analysis. RADET data for the flux-tower site locations and the GitHub repositories are archived on Zenodo (https://doi.org/10.5281/zenodo.18793164). The post-processed in situ flux data used for intercomparisons are available at https://zenodo.org/record/7636781. OpenET data extracted for the flux-tower site locations are available at https://doi.org/10.5281/zenodo.10119477. MODIS-based evapotranspiration data are available through the Google Earth Engine Data Catalog or upon request (for the updated MOD16 product provided by Arthur Endsley at the University of Montana).

Acknowledgements

We express our thanks to the data providers including in situ site investigators and technicians. We also thank Maosheng Zhao and Arthur Endsley for sharing the updated MOD16 data. This work was supported by the Maki Postdoctoral Fellowship (Desert Research Institute Maki Endowment), and U.S. Geological Survey Water Resources Research Institute, OpenET Software Tools, Datasets, and Planning Phase II (Grant G22AC00584-00) and Phase III grants (G25AC00180-00).

References

Abatzoglou, J.T., 2013. Development of gridded surface meteorological data for ecological applications and modelling. *Int. J. Climatol.,* 33, 121-131. https://doi.org/10.1002/joc.3413

Allen, R.G., Tasumi, M., Trezza, R., 2007. Satellite-Based Energy Balance for Mapping Evapotranspiration with Internalized Calibration (METRIC)—Model. *J. Irrigat. Drain. Eng.,* 133, 380-394. https://doi.org/10.1061/(asce)0733-9437(2007)133:4(380)

Allen, R.G., Trezza, R., Tasumi, M., 2006. Analytical integrated functions for daily solar radiation on slopes. *Agr. Forest Meteorol.,* 139, 55-73. https://doi.org/10.1016/j.agrformet.2006.05.012

Allen, R.G., Walter, I.A., Elliott, R., Howell, T.A., Itenfisu, D., Jensen, M.E., 2005. The ASCE standardized reference evapotranspiration equation. American Society of Civil Engineers, Reston, VA.

Anderson, M.C., Kustas, W.P., Alfieri, J.G., Gao, F., Hain, C., Prueger, J.H., Evett, S., Colaizzi, P., Howell, T., Chávez, J.L., 2012. Mapping daily evapotranspiration at Landsat spatial scales during the BEAREX'08 field campaign. *Adv. Water Resour.,* 50, 162-177. https://doi.org/10.1016/j.advwatres.2012.06.005

Bastiaanssen, W.G.M., Menenti, M., Feddes, R.A., Holtslag, A.A.M., 1998. A remote sensing surface energy balance algorithm for land (SEBAL). 1. Formulation. *J. Hydrol.,* 212-213, 198-212. https://doi.org/10.1016/S0022-1694(98)00253-4

Bird, R.B., Stewart, W.E., Lightfoot, E.N., 2002. Transport Phenomena, revised 2nd edition. New York, USA: John Wiley & Sons

Blankenau, P.A., Kilic, A., Allen, R., 2020. An evaluation of gridded weather data sets for the purpose of estimating reference evapotranspiration in the United States. *Agric. Water Manag.,* 242, 106376. https://doi.org/10.1016/j.agwat.2020.106376

Bouchet, R.J., 1963. Evapotranspiration réelle et potentielle, signification climatique. *Int. Assoc. Sci. Hydro. Pub.,* 62, 134-142.

Brutsaert, W., 1982. Evaporation into the Atmosphere: Theory, History and Applications. Dordrecht, Netherlands: D. Reidel Publishing Company

Brutsaert, W., Stricker, H., 1979. An advection-aridity approach to estimate actual regional evapotranspiration. *Water Resour. Res.,* 15, 443-450. https://doi.org/10.1029/WR015i002p00443

Brutsaert, W., Sugita, M., 1992. Application of self-preservation in the diurnal evolution of the surface energy budget to determine daily evaporation. *J. of Geophys. Res. Atmos.,* 97, 18377-18382. https://doi.org/10.1029/92JD00255

Cammalleri, C., Anderson, M.C., Kustas, W.P., 2014. Upscaling of evapotranspiration fluxes from instantaneous to daytime scales for thermal remote sensing applications. *Hydrol. Earth Syst. Sci.,* 18, 1885-1894. https://doi.org/10.5194/hess-18-1885-2014

Chen, J.M., Liu, J., 2020. Evolution of evapotranspiration models using thermal and shortwave remote sensing data. *Remote Sens. Environ.,* 237, 111594. https://doi.org/10.1016/j.rse.2019.111594

Claverie, M., Ju, J., Masek, J.G., Dungan, J.L., Vermote, E.F., Roger, J.-C., Skakun, S.V., Justice, C., 2018. The Harmonized Landsat and Sentinel-2 surface reflectance data set. *Remote Sens. Environ.,* 219, 145-161. https://doi.org/10.1016/j.rse.2018.09.002

Comini de Andrade, B., Huntington, J., Volk, J.M., Morton, C., Pearson, C., Albano, C.M., 2025. Multi-Model Intercomparison of the Complementary Relationship of Evaporation Across Global Environmental Settings. *Water Resour. Res.,* 61, e2024WR039740. https://doi.org/10.1029/2024WR039740

Crago, R., Brutsaert, W., 1996. Daytime evaporation and the self-preservation of the evaporative fraction and the Bowen ratio. *J. Hydrol.,* 178, 241-255. https://doi.org/10.1016/0022-1694(95)02803-X

Crawford, C.J., Roy, D.P., Arab, S., Barnes, C., Vermote, E., Hulley, G., Gerace, A., Choate, M., Engebretson, C., Micijevic, E., Schmidt, G., Anderson, C., Anderson, M., Bouchard, M., Cook, B., Dittmeier, R., Howard, D., Jenkerson, C., Kim, M., Kleyians, T., Maiersperger, T., Mueller, C., Neigh, C., Owen, L., Page, B., Pahlevan, N., Rengarajan, R., Roger, J.-C., Sayler, K., Scaramuzza, P., Skakun, S., Yan, L., Zhang, H.K., Zhu, Z., Zahn, S., 2023. The 50-year Landsat collection 2 archive. *Sci. Remote Sens.,* 8, 100103. https://doi.org/10.1016/j.srs.2023.100103

Davarzani, H., Smits, K., Tolene, R.M., Illangasekare, T., 2014. Study of the effect of wind speed on evaporation from soil through integrated modeling of the atmospheric boundary layer and shallow subsurface. *Water Resour. Res.,* 50, 661-680. https://doi.org/10.1002/2013WR013952

de Bruin, H.A.R., Trigo, I.F., Bosveld, F.C., Meirink, J.F., 2016. A Thermodynamically Based Model for Actual Evapotranspiration of an Extensive Grass Field Close to FAO Reference, Suitable for Remote Sensing Application. *J. Hydrometeorol.,* 17, 1373-1382. https://doi.org/10.1175/jhm-d-15-0006.1

Duc, L., Sawada, Y., 2023. A signal-processing-based interpretation of the Nash–Sutcliffe efficiency. *Hydrol. Earth Syst. Sci.,* 27, 1827-1839. https://doi.org/10.5194/hess-27-1827-2023

Endsley, K.A., Zhao, M., Kimball, J.S., Albrethsen, T., Devadiga, S., 2025. Improved Global Estimates of Terrestrial Evapotranspiration Using the MODIS and VIIRS Sensors. *J. Hydrometeorol.,* 26, 817-833. https://doi.org/10.1175/jhm-d-24-0145.1

Farr, T.G., Rosen, P.A., Caro, E., Crippen, R., Duren, R., Hensley, S., Kobrick, M., Paller, M., Rodriguez, E., Roth, L., Seal, D., Shaffer, S., Shimada, J., Umland, J., Werner, M., Oskin, M., Burbank, D., Alsdorf, D., 2007. The Shuttle Radar Topography Mission. *Rev. Geophys.,* 45. https://doi.org/10.1029/2005RG000183

Fisher, J.B., Melton, F., Middleton, E., Hain, C., Anderson, M., Allen, R., McCabe, M.F., Hook, S., Baldocchi, D., Townsend, P.A., Kilic, A., Tu, K., Miralles, D.D., Perret, J., Lagouarde, J.-P., Waliser, D., Purdy, A.J., French, A., Schimel, D., Famiglietti, J.S., Stephens, G., Wood, E.F., 2017. The future of evapotranspiration: Global requirements for ecosystem functioning, carbon and climate feedbacks, agricultural management, and water resources. *Water Resour. Res.,* 53, 2618-2626. https://doi.org/10.1002/2016WR020175

Fisher, J.B., Tu, K.P., Baldocchi, D.D., 2008. Global estimates of the land–atmosphere water flux based on monthly AVHRR and ISLSCP-II data, validated at 16 FLUXNET sites. *Remote Sens. Environ.,* 112, 901-919. https://doi.org/10.1016/j.rse.2007.06.025

Gao, B.-c., 1996. NDWI—A normalized difference water index for remote sensing of vegetation liquid water from space. *Remote Sens. Environ.,* 58, 257-266. https://doi.org/10.1016/S0034-4257(96)00067-3

García, M., Sandholt, I., Ceccato, P., Ridler, M., Mougin, E., Kergoat, L., Morillas, L., Timouk, F., Fensholt, R., Domingo, F., 2013. Actual evapotranspiration in drylands derived from in-situ and satellite data: Assessing biophysical constraints. *Remote Sens. Environ.,* 131, 103-118. https://doi.org/10.1016/j.rse.2012.12.016

Gentine, P., Entekhabi, D., Polcher, J., 2011. The diurnal behavior of evaporative fraction in the soil–vegetation–atmospheric boundary layer continuum. *J. Hydrometeorol.,* 12, 1530-1546. https://doi.org/10.1175/2011jhm1261.1

Gentine, P., Green, J.K., Guérin, M., Humphrey, V., Seneviratne, S.I., Zhang, Y., Zhou, S., 2019. Coupling between the terrestrial carbon and water cycles—a review. *Environ. Res. Lett.,* 14, 083003. https://doi.org/10.1088/1748-9326/ab22d6

Gilbert, J.T., Macfarlane, W.W., Wheaton, J.M., 2016. The Valley Bottom Extraction Tool (V-BET): A GIS tool for delineating valley bottoms across entire drainage networks. *Comput. Geosci.,* 97, 1-14. https://doi.org/10.1016/j.cageo.2016.07.014

Good, E.J., 2016. An in situ-based analysis of the relationship between land surface "skin" and screen-level air temperatures. *J. Geophys. Res. Atmos.,* 121, 8801-8819. https://doi.org/10.1002/2016JD025318

Gorelick, N., Hancher, M., Dixon, M., Ilyushchenko, S., Thau, D., Moore, R., 2017. Google Earth Engine: Planetary-scale geospatial analysis for everyone. *Remote Sens. Environ.,* 202, 18-27. https://doi.org/10.1016/j.rse.2017.06.031

Göttsche, F.-M., Olesen, F.S., (2001). Modelling of diurnal cycles of brightness temperature extracted from METEOSAT data. *Remote Sens. Environ.,* 76, 337-348. https://doi.org/10.1016/S0034-4257(00)00214-5

Gupta, H.V., Kling, H., Yilmaz, K.K., Martinez, G.F., 2009. Decomposition of the mean squared error and NSE performance criteria: Implications for improving hydrological modelling. *J. Hydrol.,* 377, 80-91. https://doi.org/10.1016/j.jhydrol.2009.08.003

Huntington, J., Minor, B., Bromley, M., Pearson, C., Beamer, J., Ingwersen, K., Carrara, K., Atkin, J., Brito, J., Morton, C., Dunkerly, C., Volk, J., Ott, T., ReVelle, P., Fellows, A., Hoskinson, M., 2025. Crop evapotranspiration, consumptive use, and open water evaporation for Oregon. *Desert Research Institute Report,* 41306. https://doi.org/10.82269/DRI-DHS-41306

Jaafar, H., Mourad, R., Schull, M., 2022. A global 30-m ET model (HSEB) using harmonized Landsat and Sentinel-2, MODIS and VIIRS: Comparison to ECOSTRESS ET and LST. *Remote Sens. Environ.,* 274, 112995. https://doi.org/10.1016/j.rse.2022.112995

Jiang, Z., Huete, A.R., Didan, K., Miura, T., 2008. Development of a two-band enhanced vegetation index without a blue band. *Remote Sens. Environ.,* 112, 3833-3845. https://doi.org/10.1016/j.rse.2008.06.006

Kang, Y., Özdoğan, M., Zipper, S.C., Román, M.O., Walker, J., Hong, S.Y., Marshall, M., Magliulo, V., Moreno, J., Alonso, L., Miyata, A., Kimball, B., Loheide, S.P., 2016. How

Universal Is the Relationship between Remotely Sensed Vegetation Indices and Crop Leaf Area Index? A Global Assessment. *Remote Sens.,* 8, 597. https://doi.org/10.3390/rs8070597

Katul, G.G., Oren, R., Manzoni, S., Higgins, C., Parlange, M.B., 2012. Evapotranspiration: A process driving mass transport and energy exchange in the soil-plant-atmosphere-climate system. *Rev. Geophys.,* 50. https://doi.org/10.1029/2011rg000366

Ketchum, D., Jencso, K., Maneta, M.P., Melton, F., Jones, M.O., Huntington, J., 2020. IrrMapper: A Machine Learning Approach for High Resolution Mapping of Irrigated Agriculture Across the Western U.S. *Remote Sens.,* 12, 2328. https://doi.org/10.3390/rs12142328

Khand, K., Senay, G.B., Friedrichs, M., Yi, K., Fisher, J.B., Wang, L., Suvočarev, K., Ahmadi, A., Chu, H., Good, S., Mallick, K., Missik, J., Nelson, J.A., Reed, D.E., Wang, T., Xiao, X., 2025. A novel approach to increase accuracy in remotely sensed evapotranspiration through basin water balance and flux tower constraints. *J. Hydrol.,* 662, 133824. https://doi.org/10.1016/j.jhydrol.2025.133824

Kim, Y., Garcia, M., Andrew Black, T., Johnson, M.S., 2025. Physically-constrained evapotranspiration models with machine learning parameterization outperform pure machine learning: Critical role of domain knowledge. *PLOS ONE,* 20, e0328798. https://doi.org/10.1371/journal.pone.0328798

Kim, Y., Garcia, M., Black, T.A., Johnson, M., 2023. Assessing the complementary role of surface flux equilibrium (SFE) theory and maximum entropy production (MEP) principle in the estimation of actual evapotranspiration. *J. Adv. Model. Earth Syst.,* 15, e2022MS003224. https://doi.org/10.1029/2022MS003224

Kim, Y., Garcia, M., Morillas, L., Weber, U., Black, T.A., Johnson, M.S., 2021. Relative humidity gradients as a key constraint on terrestrial water and energy fluxes. *Hydrol. Earth Syst. Sci.,* 25, 5175-5191. https://doi.org/10.5194/hess-25-5175-2021

Kljun, N., Calanca, P., Rotach, M.W., Schmid, H.P., 2015. A simple two-dimensional parameterisation for Flux Footprint Prediction (FFP). *Geosci. Model Dev.,* 8, 3695-3713. https://doi.org/10.5194/gmd-8-3695-2015

Kumar, S., Imen, S., Sridharan, V.K., Gupta, A., McDonald, W., Ramirez-Avila, J.J., Abdul-Aziz, O.I., Talchabhadel, R., Gao, H., Quinn, N.W.T., Weiss, W.J., Poulose, T., Palmate, S.S., Lee, C.M., Baskaran, L., 2024. Perceived barriers and advances in integrating earth observations with water resources modeling. *Remote Sens. Applications: Society and Environment,* 33, 101119. https://doi.org/10.1016/j.rsase.2023.101119

Kustas, W.P., Norman, J.M., 1999. Evaluation of soil and vegetation heat flux predictions using a simple two-source model with radiometric temperatures for partial canopy cover. *Agr. Forest Meteorol.,* 94, 13-29. https://doi.org/10.1016/S0168-1923(99)00005-2

Levenspiel, O., 1999. Chemical Reaction Engineering, 3rd edition. New York, USA: John Wiley & Sons

Liang, S., 2001. Narrowband to broadband conversions of land surface albedo I: Algorithms. *Remote Sens. Environ.,* 76, 213-238. https://doi.org/10.1016/S0034-4257(00)00205-4

Lindroth, A., Mölder, M., Lagergren, F., 2010. Heat storage in forest biomass improves energy balance closure. *Biogeosciences,* 7, 301-313. https://doi.org/10.5194/bg-7-301-2010

Liu, Y., Hiyama, T., Yasunari, T., Tanaka, H., 2012. A nonparametric approach to estimating terrestrial evaporation: Validation in eddy covariance sites. *Agr. Forest Meteorol.,* 157, 49-59. https://doi.org/10.1016/j.agrformet.2012.01.012

Liu, Z., 2021. The accuracy of temporal upscaling of instantaneous evapotranspiration to daily values with seven upscaling methods. *Hydrol. Earth Syst. Sci.,* 25, 4417-4433. https://doi.org/10.5194/hess-25-4417-2021

Loveland, T.R., Anderson, M.C., Huntington, J.L., Irons, J.R., Johnson, D.M., Rocchio, L.E., Woodcock, C.E., Wulder, M.A., 2022. Seeing our planet anew: fifty years of landsat. *Photogramm. Eng. Remote Sens.,* 88, 429-436.

Mallick, K., Baldocchi, D., Jarvis, A., Hu, T., Trebs, I., Sulis, M., Bhattarai, N., Bossung, C., Eid, Y., Cleverly, J., Beringer, J., Woodgate, W., Silberstein, R., Hinko-Najera, N., Meyer, W.S., Ghent, D., Szantoi, Z., Boulet, G., Kustas, W.P., 2022. Insights Into the Aerodynamic Versus Radiometric Surface Temperature Debate in Thermal-Based Evaporation Modeling. *Geophys. Res. Lett.,* 49, e2021GL097568. https://doi.org/10.1029/2021GL097568

Mallick, K., Jarvis, A.J., Boegh, E., Fisher, J.B., Drewry, D.T., Tu, K.P., Hook, S.J., Hulley, G., Ardö, J., Beringer, J., Arain, A., Niyogi, D., 2014. A Surface Temperature Initiated Closure (STIC) for surface energy balance fluxes. *Remote Sens. Environ.,* 141, 243-261. https://doi.org/10.1016/j.rse.2013.10.022

Martin, D.J., Niswonger, R.G., Regan, R.S., Huntington, J.L., Ott, T., Morton, C., Senay, G.B., Friedrichs, M., Melton, F.S., Haynes, J., Henson, W., Read, A., Xie, Y., Lark, T., Rush, M., 2025. Estimating irrigation consumptive use for the conterminous United States: coupling satellite-sourced estimates of actual evapotranspiration with a national hydrologic model. *J. Hydrol.,* 662, 133909. https://doi.org/10.1016/j.jhydrol.2025.133909

Mauder, M., Foken, T., Cuxart, J., 2020. Surface-Energy-Balance Closure over Land: A Review. *Boundary-Layer Meteorol.,* 177, 395-426. https://doi.org/10.1007/s10546-020-00529-6

McCabe, M.F., Wood, E.F., 2006. Scale influences on the remote estimation of evapotranspiration using multiple satellite sensors. *Remote Sens. Environ.,* 105, 271-285. https://doi.org/10.1016/j.rse.2006.07.006

McColl, K.A., Salvucci, G.D., Gentine, P., 2019. Surface flux equilibrium theory explains an empirical estimate of water-limited daily evapotranspiration. *J. Adv. Model. Earth Syst.,* 11, 2036-2049. https://doi.org/10.1029/2019ms001685

McNaughton, K.G., 1976. Evaporation and advection I: evaporation from extensive homogeneous surfaces. *Q. J. Roy. Meteorol. Soc.,* 102, 181-191. https://doi.org/10.1002/qj.49710243115

Melton, F.S., Huntington, J., Grimm, R., Herring, J., Hall, M., Rollison, D., Erickson, T., Allen, R., Anderson, M., Fisher, J.B., Kilic, A., Senay, G.B., Volk, J., Hain, C., Johnson, L., Ruhoff, A., Blankenau, P., Bromley, M., Carrara, W., Daudert, B., Doherty, C., Dunkerly, C., Friedrichs, M., Guzman, A., Halverson, G., Hansen, J., Harding, J.,

Kang, Y., Ketchum, D., Minor, B., Morton, C., Ortega-Salazar, S., Ott, T., Ozdogan, M., ReVelle, P.M., Schull, M., Wang, C., Yang, Y., Anderson, R.G., 2022. OpenET: Filling a Critical Data Gap in Water Management for the Western United States. *JAWRA J. Am. Water Resour. Assoc.,* 58, 971-994. https://doi.org/10.1111/1752-1688.12956

Melton, F.S., Johnson, L.F., Lund, C.P., Pierce, L.L., Michaelis, A.R., Hiatt, S.H., Guzman, A., Adhikari, D.D., Purdy, A.J., Rosevelt, C., Votava, P., Trout, T.J., Temesgen, B., Frame, K., Sheffner, E.J., Nemani, R.R., 2012. Satellite Irrigation Management Support With the Terrestrial Observation and Prediction System: A Framework for Integration of Satellite and Surface Observations to Support Improvements in Agricultural Water Resource Management. *IEEE J. Sel. Top. Appl. Earth Obs. Remote Sens.,* 5, 1709-1721. https://doi.org/10.1109/JSTARS.2012.2214474

Monteith, J.L., 1965. Evaporation and environment. In, Symposia of the society for experimental biology (pp. 205-234): Cambridge University Press (CUP) Cambridge

Monteith, J.L., 1981. Evaporation and surface temperature. *Q. J. Roy. Meteorol. Soc.,* 107, 1-27. https://doi.org/10.1002/qj.49710745102

Morton, F.I., 1969. Potential Evaporation as a Manifestation of Regional Evaporation. *Water Resour. Res.,* 5, 1244-1255. https://doi.org/10.1029/WR005i006p01244

Mu, Q., Zhao, M., Running, S.W., 2011. Improvements to a MODIS global terrestrial evapotranspiration algorithm. *Remote Sens. Environ.,* 115, 1781-1800. https://doi.org/10.1016/j.rse.2011.02.019

N. Moriasi, D., G. Arnold, J., W. Van Liew, M., L. Bingner, R., D. Harmel, R., L. Veith, T., 2007. Model Evaluation Guidelines for Systematic Quantification of Accuracy in Watershed Simulations. *Trans. ASABE,* 50, 885-900. https://doi.org/https://doi.org/10.13031/2013.23153

Nassar, A., Tarboton, D., Anderson, M., Yang, Y., Fisher, J.B., Purdy, A.J., Baig, F., He, C., Gochis, D., Melton, F., Volk, J., 2025. Intercomparison of the U.S. National Water Model with OpenET over the Bear River Basin, U.S. *J. Hydrol.,* 656, 132826. https://doi.org/10.1016/j.jhydrol.2025.132826

Norman, J.M., Kustas, W.P., Humes, K.S., 1995. Source approach for estimating soil and vegetation energy fluxes in observations of directional radiometric surface temperature. *Agr. Forest Meteorol.,* 77, 263-293. https://doi.org/10.1016/0168-1923(95)02265-Y

Oki, T., Kanae, S., 2006. Global hydrological cycles and world water resources. *Science,* 313, 1068-1072. https://doi.org/10.1126/science.1128845

Ott, T.J., Majumdar, S., Huntington, J.L., Pearson, C., Bromley, M., Minor, B.A., ReVelle, P., Morton, C.G., Sueki, S., Beamer, J.P., Jasoni, R.L., 2024. Toward field-scale groundwater pumping and improved groundwater management using remote sensing and climate data. *Agric. Water Manag.,* 302, 109000. https://doi.org/10.1016/j.agwat.2024.109000

Pan, X., Yang, Z., Liu, Y., Yuan, J., Wang, Z., Liu, S., Yang, Y., 2024. A non-parametric method combined with surface flux equilibrium for estimating terrestrial evapotranspiration: Validation at eddy covariance sites. *J. Hydrol.,* 631, 130682. https://doi.org/10.1016/j.jhydrol.2024.130682

Pearson, C., Minor, B., Morton, C., Volk, J., Dunkerly, C., Jensen, E., ReVelle, P., Kilic, A., Allen, R., Huntington, J.L., 2024. Historical evapotranspiration and consumptive use of irrigated areas of the Upper Colorado River Basin. *Desert Research Institute Report No. 41304, prepared for the U.S. Bureau of Reclamation*. https://doi.org/10.13140/RG.2.2.31069.63206

Penman, H.L., 1948. Natural evaporation from open water, bare soil and grass. *Proceedings of the Royal Society of London. Series A. Mathematical and Physical Sciences,* 193, 120-145.

Polhamus, A., Fisher, J.B., Tu, K.P., 2013. What controls the error structure in evapotranspiration models? *Agr. Forest Meteorol.,* 169, 12-24. https://doi.org/10.1016/j.agrformet.2012.10.002

Priestley, C.H.B., Taylor, R.J., 1972. On the assessment of surface heat flux and evaporation using large-scale parameters. *Mon. Weather Rev.,* 100, 81-92. https://doi.org/10.1175/1520-0493(1972)100<0081:otaosh>2.3.co;2

Radeloff, V.C., Roy, D.P., Wulder, M.A., Anderson, M., Cook, B., Crawford, C.J., Friedl, M., Gao, F., Gorelick, N., Hansen, M., Healey, S., Hostert, P., Hulley, G., Huntington, J.L., Johnson, D.M., Neigh, C., Lyapustin, A., Lymburner, L., Pahlevan, N., Pekel, J.-F., Scambos, T.A., Schaaf, C., Strobl, P., Woodcock, C.E., Zhang, H.K., Zhu, Z., 2024. Need and vision for global medium-resolution Landsat and Sentinel-2 data products. *Remote Sens. Environ.,* 300, 113918. https://doi.org/10.1016/j.rse.2023.113918

Rana, G., Katerji, N., 2000. Measurement and estimation of actual evapotranspiration in the field under Mediterranean climate: a review. *Eur. J. Agron.,* 13, 125-153. https://doi.org/10.1016/S1161-0301(00)00070-8

Raupach, M.R., 2001. Combination theory and equilibrium evaporation. *Q. J. Roy. Meteorol. Soc.,* 127, 1149-1181. https://doi.org/10.1002/qj.49712757402

Reitz, M., Volk, J.M., Ott, T., Anderson, M., Senay, G.B., Melton, F., Kilic, A., Allen, R., Fisher, J.B., Ruhoff, A., Purdy, A.J., Huntington, J., 2025. Performance Mapping and Weighting for the Evapotranspiration Models of the OpenET Ensemble. *Water Resour. Res.,* 61, e2024WR038899. https://doi.org/10.1029/2024WR038899

Riba, A., Garcia, M., Tarquís, A.M., Domingo, F., Antala, M., Feng, S., Liu, J., Johnson, M.S., Kim, Y., Wang, S., 2025. Integrating Remotely Sensed Thermal Observations for Calibration of Process-Based Land-Surface Models: Accuracy, Revisit Windows, and Implications in a Dryland Ecosystem. *Remote Sens.,* 17, 3630. https://doi.org/10.3390/rs17213630

Romera, D., Silver, S., 2025. Technical Memorandum: Method for Determining Consumptive Use on Irrigated Acreage in the Lower Rio Grande, New Mexico. *Appendix C to the Groundwater Settlement Agreement between the United States and the State of New Mexico, Attachment B to Joint Motion to Dismiss, Texas v. New Mexico, No. 141, Original. U.S. Supreme Court*.

Roy, S., Jensen, E., Majumdar, S., Saah, A., 2025. samapriya/awesome-gee-community-datasets: Community Catalog (3.8.0). In: Zenodo. https://doi.org/10.5281/zenodo.17641528

Running, S., Mu, Q., Zhao, M., Moreno, A., 2021. MODIS/Terra Net Evapotranspiration Gap-Filled 8-Day L4 Global 500m SIN Grid V061. In N.E.L.P.D.A.A.C. (DAAC) (Ed.) [dataset]

Salvucci, G.D., Gentine, P., 2013. Emergent relation between surface vapor conductance and relative humidity profiles yields evaporation rates from weather data. *Proc. Natl. Acad. Sci. U.S.A.,* 110, 6287-6291. https://doi.org/10.1073/pnas.1215844110

Seitzinger, S.P., Chuvieco, E., Di Giuseppe, F., Bombelli, A., Cagnazzo, C., Harris, S., Tapper, N., 2026. Relevance of earth observations of essential climate variables in wildfire adaptation. *Remote Sens. Environ.,* 332, 115082. https://doi.org/10.1016/j.rse.2025.115082

Senay, G.B., 2018. Satellite Psychrometric Formulation of the Operational Simplified Surface Energy Balance (SSEBop) Model for Quantifying and Mapping Evapotranspiration. *Appl. Eng. Agric.,* 34, 555-566. https://doi.org/10.13031/aea.12614

Senay, G.B., Bohms, S., Singh, R.K., Gowda, P.H., Velpuri, N.M., Alemu, H., Verdin, J.P., 2013. Operational Evapotranspiration Mapping Using Remote Sensing and Weather Datasets: A New Parameterization for the SSEB Approach. *JAWRA J. Am. Water Resour. Assoc.,* 49, 577-591. https://doi.org/10.1111/jawr.12057

Slatyer, R.O., McIlroy, I.C., 1961. *Practical microclimatology, with special reference to the water factor in soil-plant atmosphere relationships.* CSIRO, Melbourne.

Thakur, H., Raghav, P., Kumar, M., Wolkeba, F., 2025. Surface Flux Equilibrium Theory-Derived Evapotranspiration Estimate Outperforms ECOSTRESS, MODIS, and SSEBop Products. *Geophys. Res. Lett.,* 52, e2025GL114822. https://doi.org/10.1029/2025GL114822

Trebs, I., Mallick, K., Bhattarai, N., Sulis, M., Cleverly, J., Woodgate, W., Silberstein, R., Hinko-Najera, N., Beringer, J., Meyer, W.S., Su, Z., Boulet, G., 2021. The role of aerodynamic resistance in thermal remote sensing-based evapotranspiration models. *Remote Sens. Environ.,* 264, 112602. https://doi.org/10.1016/j.rse.2021.112602

Twine, T.E., Kustas, W.P., Norman, J.M., Cook, D.R., Houser, P.R., Meyers, T.P., Prueger, J.H., Starks, P.J., Wesely, M.L., 2000. Correcting eddy-covariance flux underestimates over a grassland. *Agr. Forest Meteorol.,* 103, 279-300. https://doi.org/10.1016/S0168-1923(00)00123-4

US Fish & Wildlife Service., 2018. National Wetlands Inventory. *US Fish & Wildlife Service*.

US Geological Survey., 2021. Landsat Collection 2 Level-2 Science Products (ver. 2.0, June 2021). *U.S. Geological Survey*. [dataset] https://doi.org/10.5066/P9OGBGM6

US Geological Survey., 2024. Annual National Land Cover Database (NLCD) Collection 1 Products: U.S. Geological Survey data release. [dataset] https://doi.org/10.5066/P94UXNTS

Volk, J., Dunkerly, C., Majumdar, S., Huntington, J., Minor, B., Kim, Y., Morton, C., ReVelle, P., Kilic, A., Melton, F., Allen, R., Pearson, C., Purdy, A., Caldwell, T., 2026. Assessing and Correcting Bias in Gridded Reference Evapotranspiration over Agricultural Lands Across the Contiguous United States. *EarthArXiv (preprint)*. https://doi.org/10.31223/X54F38

Volk, J.M., Huntington, J., Melton, F.S., Allen, R., Anderson, M.C., Fisher, J.B., Kilic, A., Senay, G., Halverson, G., Knipper, K., Minor, B., Pearson, C., Wang, T., Yang, Y., Evett, S., French, A.N., Jasoni, R., Kustas, W., 2023a. Development of a Benchmark Eddy Flux Evapotranspiration Dataset for Evaluation of Satellite-Driven Evapotranspiration Models Over the CONUS. *Agr. Forest Meteorol.,* 331, 109307. https://doi.org/10.1016/j.agrformet.2023.109307

Volk, J.M., Huntington, J.L., Melton, F., Minor, B., Wang, T., Anapalli, S., Anderson, R.G., Evett, S., French, A., Jasoni, R., Bambach, N., Kustas, W.P., Alfieri, J., Prueger, J., Hipps, L., McKee, L., Castro, S.J., Alsina, M.M., McElrone, A.J., Reba, M., Runkle, B., Saber, M., Sanchez, C., Tajfar, E., Allen, R., Anderson, M., 2023b. Post-processed data and graphical tools for a CONUS-wide eddy flux evapotranspiration dataset. *Data Brief,* 48, 109274. https://doi.org/10.1016/j.dib.2023.109274

Volk, J.M., Huntington, J.L., Melton, F.S., Allen, R., Anderson, M., Fisher, J.B., Kilic, A., Ruhoff, A., Senay, G.B., Minor, B., Morton, C., Ott, T., Johnson, L., Comini de Andrade, B., Carrara, W., Doherty, C.T., Dunkerly, C., Friedrichs, M., Guzman, A., Hain, C., Halverson, G., Kang, Y., Knipper, K., Laipelt, L., Ortega-Salazar, S., Pearson, C., Parrish, G.E.L., Purdy, A., ReVelle, P., Wang, T., Yang, Y., 2024. Assessing the accuracy of OpenET satellite-based evapotranspiration data to support water resource and land management applications. *Nat. Water,* 2, 193-205. https://doi.org/10.1038/s44221-023-00181-7

Wang, K., Dickinson, R.E., 2012. A review of global terrestrial evapotranspiration: Observation, modeling, climatology, and climatic variability. *Rev. Geophys.,* 50. https://doi.org/10.1029/2011RG000373

Wobus, C., Nash, C., Culp, P., Kelly, M., Kennedy, K., 2025. Simplified agricultural water use accounting in the Colorado River Basin using OpenET. *Environ. Res. Lett.,* 20, 014020. https://doi.org/10.1088/1748-9326/ad984b

Woodward, B.D., Evangelista, P.H., Young, N.E., Vorster, A.G., West, A.M., Carroll, S.L., Girma, R.K., Hatcher, E.Z., Anderson, R., Vahsen, M.L., Vashisht, A., Mayer, T., Carver, D., Jarnevich, C., 2018. CO-RIP: A Riparian Vegetation and Corridor Extent Dataset for Colorado River Basin Streams and Rivers. *ISPRS Int. J. Geo-Inf.,* 7, 397. https://doi.org/10.3390/ijgi7100397

Xie, Y., Lark, T.J., 2021. Mapping annual irrigation from Landsat imagery and environmental variables across the conterminous United States. *Remote Sens. Environ.,* 260, 112445. https://doi.org/10.1016/j.rse.2021.112445

Xue, J., Anderson, M.C., Gao, F., Hain, C., Sun, L., Yang, Y., Knipper, K.R., Kustas, W.P., Torres-Rua, A., Schull, M., 2020. Sharpening ECOSTRESS and VIIRS land surface temperature using harmonized Landsat-Sentinel surface reflectances. *Remote Sens. Environ.,* 251, 112055. https://doi.org/10.1016/j.rse.2020.112055

Zhang, L., Hu, Z., Fan, J., Zhou, D., Tang, F., 2014. A meta-analysis of the canopy light extinction coefficient in terrestrial ecosystems. *Front. Earth Sci.,* 8, 599-609. https://doi.org/10.1007/s11707-014-0446-7

Zhang, Y., Kong, D., Gan, R., Chiew, F.H.S., McVicar, T.R., Zhang, Q., Yang, Y., 2019. Coupled estimation of 500 m and 8-day resolution global evapotranspiration and gross

primary production in 2002–2017. *Remote Sens. Environ.,* 222, 165-182. https://doi.org/10.1016/j.rse.2018.12.031

Zhao, B., Huntington, J., Pearson, C., Zhao, G., Ott, T., Zhu, J., Weinberg, A., Holman, K.D., Zhang, S., Anderson, R., Strickler, M., Cotter, J., Fernando, N., Nowak, K., Gao, H., 2024. Developing a General Daily Lake Evaporation Model and Demonstrating Its Application in the State of Texas. *Water Resour. Res.,* 60, e2023WR036181. https://doi.org/10.1029/2023WR036181

Appendix A: Canopy ET under the DIF assumption

Canopy ET is primarily driven by transpiration through stomatal pores. Accordingly, we begin our derivation by expressing the canopy latent heat flux as a function of surface and aerodynamic conductances, following the bigleaf model formulation (Monteith, 1965). In contrast, the sensible heat flux is controlled solely by aerodynamic conductance.

$$LE_c = L_v \rho \frac{g_c g_{ac}}{g_c + g_{ac}} \frac{MW_r}{PA} [e^*(T_c) - e_a] \quad (A1)$$

$$H_c = \rho c_p g_{ac} (T_c - T_a) \quad (A2)$$

where LE_c is latent heat flux at the canopy, H_c is sensible heat flux at the canopy, L_v is latent heat of vaporization, c_p is specific heat of dry air at constant pressure, ρ is air density, PA is air pressure, MW_r is molecular weight ratio of water vapor versus dry air (0.622), g_c is canopy surface conductance, g_{ac} is aerodynamic conductance for heat between canopy surface to the reference height, $e^*(T_c)$ is saturation water vapor at the canopy surface temperature T_c, and q_a is reference height water vapor. Here, we assume that g_{ac} is identical for water vapor and heat transfer (Monin and Obukhov, 1954).

By linearizing the saturation vapor pressure curve, the sensible heat flux can be substituted into the latent heat flux equation as follows (Monteith, 1965):

$$LE_c = \frac{g_c}{g_c + g_{ac}} \frac{\Delta}{\gamma} H_c + L_v \rho \frac{g_c g_{ac}}{g_c + g_{ac}} \frac{MW_r}{PA} VPD_a \quad (A3)$$

where Δ is the slope of the saturation vapor pressure curve with respect to air temperature (T_a); γ is the psychrometric constant; VPD_a is vapor pressure deficit at the reference height (i.e., $VPD_a = e^*(T_a) - e_a$).

Next, we express H_c using the canopy surface energy balance,

$$H_c = R_{nc} - LE_c \quad (A4a)$$

$$R_{nc} = (1 - \tau_S) SW_n + (1 - \tau_L)(LW_{atm} + LW_{soil} - 2\varepsilon\sigma {T_c}^4) \quad (A4b)$$

where SW_n is net shortwave radiation, τ_S and τ_L are shortwave and longwave transmissivity, respectively, LW_{atm} is long wave radiation from atmosphere, LW_{soil} is longwave radiation emitted from soil, ε is land surface emissivity, σ is Stefan-Boltzmann constant. In Equation (A4b), the last term on the right-hand side represents the bidirectional longwave radiation emitted from the canopy.

In order to eliminate dependency of R_{nc} on land surface temperature, we introduce the isothermal net radiation (R_{nci}), which is defined as R_{nc} if $T_c = T_a$ (Monteith, 1981; Martin, 1989; Raupach, 2001; McColl, 2020; Kim et al., 2023).

$$R_{nci} = R_{nc} + 8(1-\tau_L)\varepsilon\sigma {T_a}^3 (T_c - T_a) \quad (A5)$$

The last term on the right-hand side of Equation (A5) is a linearized correction accounting for the difference between R_{nc} and R_{nci} due to vertical temperature difference. This term can be expressed using sensible heat flux (Monteith, 1981):

$$8(1-\tau_L)\varepsilon\sigma {T_a}^3 (T_c - T_a) = \frac{g_{Rc}}{g_{ac}} H_c \quad (A6)$$

where $g_{Rc}(= \frac{8(1-\tau_c)\varepsilon\sigma {T_a}^3}{\rho c_p})$ is radiative conductance at canopy surface (see Equation (4a) in the main text). Substituting Equations (A5) and (A6) into (A4) yields:

$$H_c = \frac{g_{ac}}{g_{ac} + g_{Rc}} (R_{nci} - LE_c) \quad (A7)$$

Substituting Equation (A7) into Equation (A3) yields:

$$LE_c = \frac{g_c}{g_c + g_{ac}} \frac{\Delta}{\gamma} [\frac{g_{ac}}{g_{ac} + g_{Rc}} (R_{nci} - LE_c)] + L_v \rho \frac{g_c g_{ac}}{g_c + g_{ac}} \frac{MW_r}{PA} VPD_a \quad (A8)$$

Equation (A8) excludes any meteorological variables at the canopy surface (e.g., surface temperature and humidity), whose values can vary with changes in g_{ac} (Figure 1). Thus, under the DIF assumption (i.e., $\frac{\partial LE_c}{\partial g_{ac}} = 0$), we can consider all variables in Equation (A8), including the flux term, to be independent of g_{ac}. By taking the partial derivative of Equation (A8) with respect to g_{ac} and performing some algebraic manipulation (i.e., multiplying both sides by $\frac{g_{ac}(g_c+g_{ac})}{g_c}$ and then substituting Equation A7), we obtain:

$$0 = [-\frac{g_{ac}}{g_c + g_{ac}} + \frac{g_{Rc}}{g_{ac} + g_{Rc}}] \frac{\Delta}{\gamma} H_c + L_v \rho \frac{g_c g_{ac}}{g_c + g_{ac}} \frac{MW_r}{PA} VPD_a \quad (A9)$$

By subtracting Equation (A9) from Equation (A3), the last term on the right-hand side of Equation (A3) is canceled, yielding:

$$LE_c = \frac{g_{ac}}{g_{ac} + g_{Rc}} \frac{\Delta}{\gamma} H_c \quad (A10)$$

By defining $\mu_c = \frac{g_{ac}+g_{Rc}}{g_{ac}}$ and substituting Equation (A4) (i.e., the canopy energy balance equation), Equation (A10) can be expressed as follows.

$$LE_c = \frac{\Delta}{\Delta + \mu_c \gamma} R_{nc} \tag{A11}$$

Equation (A11) is comparable to the equilibrium ET derivation from the DIF hypothesis by Raupach (2001), and it also represents the canopy component of Equation (2) in the main text. However, μ_c still includes the g_{ac} term, which we aim to eliminate. To address this, we performed additional algebraic manipulation by substituting Equation (A10) into Equations (A4) and (A7), respectively.

$$H_c = R_{nc} - \frac{1}{\mu_c}\frac{\Delta}{\gamma} H_c \tag{A12a}$$

$$H_c = \frac{1}{\mu_c}\left(R_{nci} - \frac{1}{\mu_c}\frac{\Delta}{\gamma} H_c\right) \tag{A12b}$$

Next, we rearranged Equations (A12a) and (A12b) with respect to H_c and substituted them into each other to eliminate H_c.

$$\frac{R_{nc}}{1 + \frac{1}{\mu_c}\frac{\Delta}{\gamma}} = \frac{\frac{1}{\mu_c} R_{nci}}{1 + \frac{1}{{\mu_c}^2}\frac{\Delta}{\gamma}} \tag{A13}$$

By performing some algebraic manipulation, we can write:

$$R_{nc}{\mu_c}^2 - R_{nci}\mu_c - \frac{\Delta}{\gamma}(R_{nci} - R_{nc}) = 0 \tag{A14}$$

By solving Equation (A14) with respect to positive μ_c, we obtain:

$$\mu_c = \frac{R_{nci} + \sqrt{{R_{nci}}^2 + 4\frac{\Delta}{\gamma} R_{nc}(R_{nci} - R_{nc})}}{2R_{nc}} \tag{A15}$$

At this stage, the expression for μ_c no longer depends on g_{ac}. Equation (A15) is equivalent to Equation (3a) in the main text.

Appendix B: Soil ET under the DIF assumption

The derivation of soil ET under the DIF assumption follows a similar procedure to that of the canopy component. Therefore, this section largely repeats the content of Appendix A. However, we provide a standalone Appendix B for the soil component to highlight several key differences. In particular, the parameterization of water stress and the inclusion of soil heat flux introduce slight variations in both the derivation and the resulting equations.

Unlike canopy evapotranspiration, which is primarily regulated by stomatal pores, soil evaporation is constrained by the soil surface water potential. This water potential can be represented by the relative humidity at the surface–air interface (Novak, 2019). Accordingly, we parameterize the latent heat flux at the soil surface as follows (Monteith, 1981; Kim et al., 2021):

$$LE_s = L_v \rho g_{as} \frac{MW_r}{PA} [RH_s e^*(T_s) - e_a] \quad (B1)$$

$$H_s = \rho c_p g_{as} (T_s - T_a) \quad (B2)$$

where LE_s is latent heat flux at the soil, H_s is sensible heat flux at the soil, g_{as} is aerodynamic conductance for heat and water vapor between soil surface to the reference height, RH_s is relative humidity at the soil surface, and T_s is soil surface temperature.

While g_c was assumed to be independent of g_{ac} in the canopy model, RH_s, representing water potential, is similarly assumed to be independent of g_{as} in the soil model. Also, we assume same land surface temperature for canopy and soil at daily time scale.

By linearizing the saturation vapor pressure curve, the sensible heat flux can be substituted into the latent heat flux equation as follows (Monteith, 1981; Kim et al., 2021):

$$LE_s = \frac{RH_s \Delta}{\gamma} H_s + L_v \rho g_{as} \frac{MW_r}{PA} [RH_s e^*(T_a) - e_a] \quad (B3)$$

Next, we express H_s using the soil surface energy balance.

$$H_s = R_{ns} - G - LE_s \quad (B4a)$$

$$R_{ns} = \tau_S SW_n + \tau_L LW_{atm} + (1 - \tau_L) LW_{canopy} - \varepsilon \sigma {T_s}^4 \quad (B4b)$$

where R_{ns} is net radiation at soil surface, G is soil heat flux, LW_{canopy} is longwave radiation emitted from canopy. In Equation (B4b), the last term on the right-hand side represents longwave radiation emitted from the canopy.

As for soil heat flux, we express it using a “one-layer” model (Raupach, 2001; McColl, 2020):

$$G = \frac{k_g}{d_g}(T_s - T_g) \quad (B5)$$

where k_g is the thermal conductivity of the soil, d_g is a soil storage length scale, and T_g is a specified bulk temperature for the thermal store, representing the subsurface temperature. Specifically, d_g and T_g are defined as the depth and corresponding temperature, respectively, below which temperature is not directly influenced by aerodynamic exchange at the daily time scale. Here, $\frac{k_g}{d_g}$ is treated here as an effective conductive exchange coefficient.

The isothermal available energy at the soil surface can be defined as follows model (Raupach, 2001; McColl, 2020):

$$\underbrace{R_{nsi} - G_i}_{AE_{si}} = \underbrace{R_{ns} - G}_{AE_s} + [4\varepsilon\sigma {T_a}^3 + \frac{k_g}{d_g}](T_s - T_a) \quad (B6)$$

where AE_s is available energy at the soil surface, and AE_{si} represents isothermal available energy at the soil surface. The last term on the right-hand side of Equation (B6) is a linearized correction due to vertical temperature difference. This term can be expressed using sensible heat flux:

$$[4\varepsilon\sigma {T_a}^3 + \frac{k_g}{d_g}](T_s - T_a) = \frac{g_{Rs}}{g_{as}} H_s \quad (B7)$$

where $g_{Rs}(= \frac{4\varepsilon\sigma {T_a}^3 + k_g/d_g}{\rho c_p})$ is radiative conductance at soil surface (see Equation (4b) in the main text). Substituting Equations (B6) and (B7) into (B4) yields:

$$H_s = \frac{g_{as}}{g_{as} + g_{Rs}}(AE_{si} - LE_s) \quad (B8)$$

Substituting Equation (B8) into Equation (B3) yields:

$$LE_s = \frac{RH_s\Delta}{\gamma}[\frac{g_{as}}{g_{as} + g_{Rs}}(AE_{si} - LE_s)] + L_v\rho g_{as}\frac{MW_r}{PA}[RH_s e^*(T_a) - e_a] \quad (B9)$$

Equation (B9) excludes any meteorological variables at the soil surface (e.g., surface temperature and humidity), whose values can vary with changes in g_{as} (Figure 1). Thus, under the DIF assumption (i.e., $\frac{\partial LE_s}{\partial g_{as}} = 0$), we can consider all variables in Equation (B9), including the flux term, to be independent of g_{as}. By taking the partial derivative of Equation (B9) with respect to g_{as} and performing some algebraic manipulation (i.e., multiplying both sides by g_{as} and then substituting Equation B8), we obtain:

$$0 = \frac{g_{Rs}}{g_{as} + g_{Rs}} \frac{RH_s\Delta}{\gamma} H_s + L_v \rho g_{as} \frac{MW_r}{PA} [RH_s e^*(T_a) - e_a] \quad (B10)$$

By subtracting Equation (B10) from Equation (B3), the last term on the right-hand side of Equation (B3) is canceled, yielding:

$$LE_s = \frac{g_{as}}{g_{as} + g_{Rs}} \frac{RH_s\Delta}{\gamma} H_s \quad (B11)$$

By defining $\mu_s = \frac{g_{as}+g_{Rs}}{g_{as}}$ and substituting Equation (B4) (i.e., the soil surface energy balance equation), Equation (B11) can be expressed as follows.

$$LE_s = \frac{RH_s\Delta}{RH_s\Delta + \mu_s\gamma} (R_{ns} - G) \quad (B12)$$

Equation (B12) represents the soil component of Equation (2) in the main text.

Next, we eliminate g_{as} from μ_s by performing additional algebraic manipulation. Substituting Equation (B11) into Equations (B4) and (B8), respectively.

$$H_s = AE_s - \frac{1}{\mu_s} \frac{RH_s\Delta}{\gamma} H_s \quad (B13a)$$

$$H_s = \frac{1}{\mu_s} (AE_{si} - \frac{1}{\mu_s} \frac{RH_s\Delta}{\gamma} H_s) \quad (B13b)$$

Rearranging Equations (B13a) and (B13b) with respect to H_s and substituted them into each other to eliminate H_s.

$$\frac{AE_s}{1 + \frac{1}{\mu_s} \frac{RH_s\Delta}{\gamma}} = \frac{\frac{1}{\mu_s} AE_{si}}{1 + \frac{1}{{\mu_s}^2} \frac{RH_s\Delta}{\gamma}} \quad (B14)$$

By performing some algebraic manipulation, we can write:

$$AE_s {\mu_s}^2 - AE_{si}\mu_s - \frac{RH_s\Delta}{\gamma} (AE_{si} - AE_s) = 0 \quad (B15)$$

By solving Equation (B15) with respect to positive μ_s, we obtain:

$$\mu_s = \frac{AE_{si} + \sqrt{{AE_{si}}^2 + 4 \frac{RH_s\Delta}{\gamma} AE_s (AE_{si} - AE_s)}}{2AE_s} \quad (B16)$$

At this stage, the expression for μ_s no longer depends on g_{as}. Equation (B16) is equivalent to Equation (3b) in the main text.

While all variables in this Appendix can be directly derived as described in the main text or other appendices, the effective soil conductive exchange coefficient ($\frac{k_g}{d_g}$, MJ m^{-2} K^{-1} d^{-1}) introduced in Equation (B5) requires an additional model. Here, d_g represents an effective soil thermal damping depth beyond which temperature fluctuations are weakly coupled to atmospheric forcing at daily time scales. Although conceptually straightforward, the corresponding soil storage length scale is not uniquely prescribed by first principles, owing to the continuous nature of subsurface heat conduction and its dependence on soil thermal properties (Kim et al., 2023).

To constrain d_g in a physically consistent yet parsimonious manner, we adopt a steady-state force–restore framework (Bhumralkar, 1975), interpreting d_g as the thermal damping depth associated with periodic surface temperature forcing. Surface–atmospheric exchange introduces high-frequency soil surface temperature variations that decay exponentially with depth through conductive diffusion.

By introducing soil thermal inertia, the ratio of soil thermal conductivity to damping depth can be further simplified as follows (Huang and Wang, 2016):

$$\frac{k_g}{d_g} = I_s\sqrt{\frac{\omega}{2}}\frac{86400}{10^6} \qquad (B17)$$

where I_s is the thermal inertia of the soil (J m^{-2} K^{-1} s$^{-1/2}$), and ω is the fundamental diurnal angular frequency ($\omega = 2\pi/86400\ s^{-1}$).

Observed soil thermal inertia spans a relatively narrow range, with values around 800 for dry soils and up to 1500 for pure water (Bennett et al., 2008; Huang and Wang, 2016). Sensitivity tests conducted over an I_s range of 800-1500 show weak impacts on ET estimates. Accordingly, we adopt a constant value of $I_s = 1000$ J m^{-2} K^{-1} s$^{-1/2}$ for parsimonious estimation.

Appendix C: A constraint for canopy surface temperature (Equation 11)

With given aerodynamic surface temperature (T_{aero}), the daily total sensible heat flux can be written as:

$$H = \rho c_p g_{aH}(T_{aero} - T_a) \quad (C1)$$

where g_{aH} is the daily aerodynamic conductance for heat.

At instantaneous daytime scales, it is well established that radiometric land surface temperature (*LST*) is not strictly equivalent to T_{aero}, due to differences in radiative and aerodynamic source areas. However, when averaged over a daily timescale, these differences are substantially reduced as diurnal variability in surface thermal heterogeneity and turbulent exchange is integrated out. As a result, the discrepancy between T_{aero} and *LST* becomes small. Accordingly, we approximate T_{aero} using *LST* in Eq. (C1).

$$H \approx \rho c_p g_{aH}(LST - T_a) \quad (C2)$$

Here, all variables represent daily average value.

The ratio between the canopy sensible heat flux (Equation A2) and the total sensible heat flux (Equation C2) can then be expressed as:

$$\frac{H_c}{H} = \frac{\rho c_p g_{ac}(T_c - T_a)}{\rho c_p g_{aH}(LST - T_a)} \quad (C3)$$

From the single source perspective, the canopy surface can be considered to function aerodynamically as the land surface itself. In other words, surface temperature is interpreted as the temperature at the displacement height, which is typically 60–70% of canopy height (Knauer et al., 2018). Under this interpretation, the aerodynamic conductance for the whole surface is reasonably approximated by the aerodynamic conductance of the canopy layer. Therefore, we can set $g_{aH} \approx g_{ac}$, and Equation (C3) simplifies to:

$$\frac{T_c - T_a}{LST - T_a} = \frac{H_c}{H} \quad (C4)$$

With the DIF constrain, total and canopy sensible heat fluxes can be written as:

$$H_c = \frac{\mu_c \gamma}{\Delta + \mu_c \gamma} R_{nc} \quad (C5a)$$

$$H = \frac{\mu_c \gamma}{\Delta + \mu_c \gamma} R_{nc} + \frac{\mu_s \gamma}{RH_s \Delta + \mu_s \gamma}(R_{ns} - G) \quad (C5b)$$

Substituting Equations (C5a) and (C5b) into Equation (C4) gives:

$$\frac{T_c - T_a}{LST - T_a} = \frac{\frac{\mu_c \gamma}{\Delta + \mu_c \gamma} R_{nc}}{\frac{\mu_c \gamma}{\Delta + \mu_c \gamma} R_{nc} + \frac{\mu_s \gamma}{RH_s \Delta + \mu_s \gamma} (R_{ns} - G)} \quad (C6)$$

By assuming soil heat flux is relatively negligible at the daily timescale, we can write:

$$\frac{T_c - T_a}{LST - T_a} = \frac{\frac{\mu_c \gamma}{\Delta + \mu_c \gamma} f_c}{\frac{\mu_c \gamma}{\Delta + \mu_c \gamma} f_c + \frac{\mu_s \gamma}{RH_s \Delta + \mu_s \gamma} (1 - f_c)} \quad (C7)$$

where f_c is fractional vegetation cover and represents the fraction of net radiation absorbed by the canopy (Norman et al., 1995).

Rearranging Equation (C7) gives Equations (11a) and (11b) in the main text.

Appendix D: soil surface relative humidity (Equation 18)

We directly derive soil surface relative humidity (RH_s) from the ET_{DIF} formulation to ensure physical consistency. To achieve this, we first substitute Equation (B11) into Equation (B3), which yields:

$$-\frac{\mu_s - 1}{\mu_s}\frac{RH_s\Delta}{\gamma}H_s = L_v\rho g_{as}\frac{MW_r}{PA}[RH_s e^*(T_a) - e_a] \quad (D1)$$

Substituting the soil sensible heat flux formulation (Equation B2) into Equation (D1), we simplify it as follows:

$$-\frac{\mu_s - 1}{\mu_s}RH_s\Delta(T_s - T_a) = RH_s e^*(T_a) - e_a \quad (D2)$$

Rearranging for RH_s yields:

$$RH_s = \frac{e_a}{e^*(T_a) + \Delta(T_s - T_a)\frac{\mu_s - 1}{\mu_s}} \quad (D3)$$

Equation (D3) is equivalent to Equation (20) in the main text.

Appendix E: Reintroducing $\frac{\partial ET}{\partial g_a}$ under relaxation of the DIF hypothesis

We derive the ET formulation obtained when the DIF hypothesis is relaxed. In the canopy derivation (Appendix A), if $\frac{\partial LE_c}{\partial g_{ac}} \neq 0$, then Equation (A11) must retain $\frac{\partial LE_c}{\partial g_{ac}}$ as follows:

$$LE_c = \frac{\Delta}{\Delta + \mu_c \gamma} R_{nc} + \frac{\Delta + \mu_c \gamma^*}{\Delta + \mu_c \gamma} g_{ac} \frac{\partial LE_c}{\partial g_{ac}} \quad (E1a)$$

$$\gamma^* = \gamma(1 + \frac{g_{ac}}{g_c}) \quad (E1b)$$

Similarly, in the soil derivation (Appendix B), if $\frac{\partial LE_s}{\partial g_{as}} \neq 0$, then Equation (B12) becomes:

$$LE_s = \frac{RH_s \Delta}{RH_s \Delta + \mu_s \gamma} (R_{ns} - G) + g_{as} \frac{\partial LE_s}{\partial g_{as}} \quad (E2)$$

Summing the canopy and soil components yields:

$$LE = \underbrace{[\frac{\Delta}{\Delta + \mu_c \gamma} R_{nc} + \frac{RH_s \Delta}{RH_s \Delta + \mu_s \gamma} (R_{ns} - G)]}_{ET_{DIF}} + \underbrace{[\frac{\Delta + \mu_c \gamma^*}{\Delta + \mu_c \gamma} g_{ac} \frac{\partial LE_c}{\partial g_{ac}} + g_{as} \frac{\partial LE_s}{\partial g_{as}}]}_{aerodynamic\ term} \quad (E3)$$

This formulation demonstrates that ET can be expressed as the sum of ET_{DIF} and an additional aerodynamic term when the DIF hypothesis is relaxed. A key challenge, however, is that the aerodynamic term in Equation (E3) depends on both surface and aerodynamic conductances, as well as the sensitivity of ET to aerodynamic conductance, which is difficult to quantify from first principles. To address this limitation, we propose the RADET model, which represents ET as the sum of ET_{DIF} and a Penman's aerodynamic term. In this formulation, PTJPL-style constraint functions are introduced to the aerodynamic term.

Again, when the DIF hypothesis holds, Equation (E3) reduces to:

$$LE = \underbrace{[\frac{\Delta}{\Delta + \mu_c \gamma} R_{nc} + \frac{RH_s \Delta}{RH_s \Delta + \mu_s \gamma} (R_{ns} - G)]}_{ET_{DIF}} + \underbrace{[\frac{\Delta + \mu_c \gamma^*}{\Delta + \mu_c \gamma} g_{ac} \overbrace{\frac{\partial LE_c}{\partial g_{ac}}}^{\frac{\partial LE_c}{\partial g_{ac}} \approx 0} + g_{as} \overbrace{\frac{\partial LE_s}{\partial g_{as}}}^{\frac{\partial LE_s}{\partial g_{as}} \approx 0}]}_{aerodynamic\ term} \quad (E4a)$$

$$\therefore LE = \underbrace{\frac{\Delta}{\Delta + \mu_c \gamma} R_{nc} + \frac{RH_s \Delta}{RH_s \Delta + \mu_s \gamma} (R_{ns} - G)}_{ET_{DIF}} \quad (E4b)$$

indicating that ET is fully determined by ET_{DIF}, without any additional aerodynamic contribution.

Appendix F: Statistical metrics

The Root Mean Square Error (RMSE) was calculated as

$$RMSE = \sqrt{\sum_{i=1}^{n} \frac{(P_i - O_i)^2}{n}} \quad (F1)$$

where O_i is the observed ET, P_i is the model predicted ET, and n is the total number of paired model-measured ET data points.

The Mean Absolute Error (MAE) was calculated as

$$MAE = \frac{1}{n}\sum_{i=1}^{n} |P_i - O_i| \quad (F2)$$

and the Mean Bias Error (MBE) was calculated as

$$MAE = \frac{1}{n}\sum_{i=1}^{n} (P_i - O_i) \quad (F3)$$

The Nash-Sutcliffe Efficiency (NSE) (Nash and Sutcliffe, 1970) was calculated as

$$NSE = 1 - \frac{\sum_{i=1}^{n}(P_i - O_i)^2}{\sum_{i=1}^{n}(\mu_o - O_i)^2} \quad (F4)$$

where μ_o is the observed mean.

The Kling-Gupta Efficiency (KGE) (Gupta et al., 2009) was calculated as

$$KGE = 1 - \sqrt{(r-1)^2 + (\alpha - 1)^2 + (\beta - 1)^2} \quad (F5a)$$

$$\alpha = \frac{\sigma_P}{\sigma_o} \quad (F5b)$$

$$\beta = \frac{\mu_P}{\mu_o} \quad (F5c)$$

where r is the Pearson correlation coefficient, σ_o and σ_P are the standard deviation of the predicted and observed values, respectively, μ_P is the predicted mean.

While the regression slopes were estimated by forcing the model through the origin in one-on-one figures to emphasize proportional bias, the coefficient of determination (R^2) reported were calculated as the square of the Pearson correlation coefficient (r^2).

Appendix Reference

Bennett, W.B., Wang, J., Bras, R.L., 2008. Estimation of Global Ground Heat Flux. *J. Hydrometeorol.,* 9, 744-759. https://doi.org/10.1175/2008JHM940.1

Bhumralkar, C.M., 1975. Numerical experiments on the computation of ground surface temperature in an atmospheric general circulation model. *J. Appl. Meteorol. Climatol.,* 14, 1246–1258. https://doi.org/10.1175/1520-0450(1975)014%3C1246:NEOTCO%3E2.0.CO;2

Gupta, H.V., Kling, H., Yilmaz, K.K., Martinez, G.F., 2009. Decomposition of the mean squared error and NSE performance criteria: Implications for improving hydrological modelling. *J. Hydrol.,* 377, 80-91. https://doi.org/10.1016/j.jhydrol.2009.08.003

Huang, S.-Y., Wang, J., 2016. A coupled force-restore model of surface temperature and soil moisture using the maximum entropy production model of heat fluxes. *J. Geophys. Res. Atmos.,* 121, 7528-7547. https://doi.org/10.1002/2015JD024586

Kim, Y., Garcia, M., Black, T.A., Johnson, M., 2023. Assessing the complementary role of surface flux equilibrium (SFE) theory and maximum entropy production (MEP) principle in the estimation of actual evapotranspiration. *J. Adv. Model. Earth Syst.,* 15, e2022MS003224. https://doi.org/10.1029/2022MS003224

Kim, Y., Garcia, M., Morillas, L., Weber, U., Black, T.A., Johnson, M.S., 2021. Relative humidity gradients as a key constraint on terrestrial water and energy fluxes. *Hydrol. Earth Syst. Sci.,* 25, 5175-5191. https://doi.org/10.5194/hess-25-5175-2021

Knauer, J., El-Madany, T.S., Zaehle, S., Migliavacca, M., 2018. Bigleaf—An R package for the calculation of physical and physiological ecosystem properties from eddy covariance data. *PLOS ONE,* 13, e0201114. https://doi.org/10.1371/journal.pone.0201114

Martin, P., 1989. The significance of radiative coupling between vegetation and the atmosphere. *Agr. Forest Meteorol.,* 49, 45-53. https://doi.org/10.1016/0168-1923(89)90061-0

McColl, K.A., 2020. Practical and theoretical benefits of an alternative to the Penman-Monteith evapotranspiration equation. *Water Resour. Res.,* 56, e2020WR027106. https://doi.org/10.1029/2020wr027106

Monin, A.S., Obukhov, A.M., 1954. Basic laws of turbulent mixing in the surface layer of the atmosphere. *Contrib. Geophys. Inst. Acad. Sci. USSR,* 151, e187.

Monteith, J.L., 1965. Evaporation and environment. In, Symposia of the society for experimental biology (pp. 205-234): Cambridge University Press (CUP) Cambridge

Monteith, J.L., 1981. Evaporation and surface temperature. *Q. J. Roy. Meteorol. Soc.,* 107, 1-27. https://doi.org/10.1002/qj.49710745102

Nash, J.E., Sutcliffe, J.V., 1970. River flow forecasting through conceptual models part I — A discussion of principles. *J. Hydrol.,* 10, 282-290. https://doi.org/https://doi.org/10.1016/0022-1694(70)90255-6

Norman, J.M., Kustas, W.P., Humes, K.S., 1995. Source approach for estimating soil and vegetation energy fluxes in observations of directional radiometric surface temperature. *Agr. Forest Meteorol.,* 77, 263-293. https://doi.org/10.1016/0168-1923(95)02265-Y

Novak, M.D., 2019. Validity of assuming equilibrium between liquid water and vapor for simulating evaporation. *Water Resour. Res.,* 55, 9858-9872. https://doi.org/10.1029/2019WR025113

Raupach, M.R., 2001. Combination theory and equilibrium evaporation. *Q. J. Roy. Meteorol. Soc.,* 127, 1149-1181. https://doi.org/10.1002/qj.49712757402

Supplementary Materials for "Thermodynamically constrained surface energy balance using medium-resolution remote sensing for efficient evapotranspiration mapping"

Yeonuk Kim[a,*], Justin L Huntington[a], Bruno Comini de Andrade[b], Mark S Johnson[c,d], John M Volk[a], Sayantan Majumdar[a], Charles Morton[a], Peter ReVelle[a]

Affiliations

a. Division of Hydrologic Sciences, Desert Research Institute, Reno, Nevada, USA
b. Hydraulic Research Institute, Federal University of Rio Grande do Sul, Porto Alegre, Brazil
c. Institute for Resources, Environment and Sustainability, University of British Columbia, Vancouver, BC, Canada
d. Department of Earth, Ocean and Atmospheric Sciences, University of British Columbia, Vancouver, BC, Canada

***Corresponding author:** Yeonuk Kim (yeonuk.kim@dri.edu)

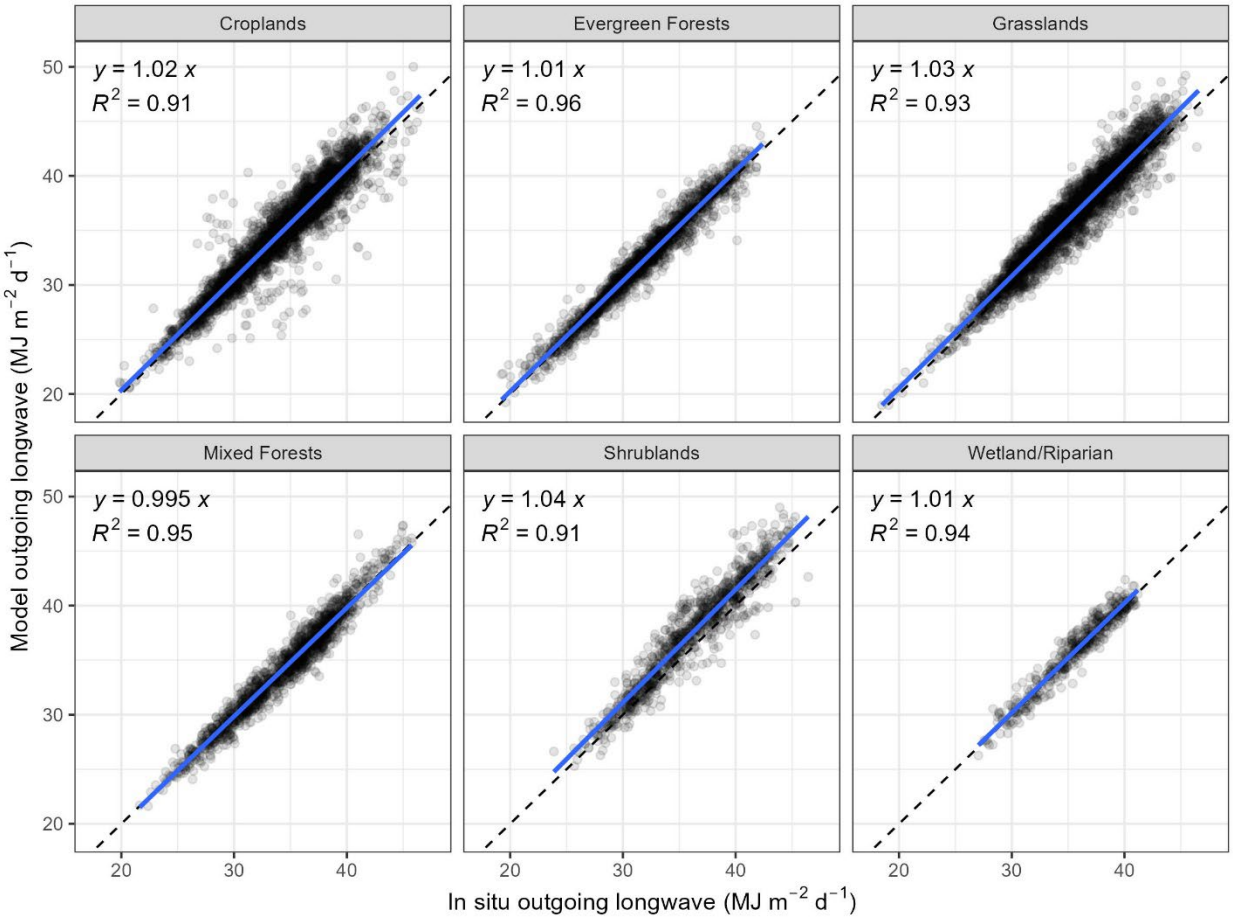

Figure S1 Evaluation of daily mean land surface temperature (LST_{daily}) estimated from satellite observations. The x-axis represents the daily outgoing longwave radiation observed at flux tower sites, while the y-axis represents outgoing longwave radiation calculated from modeled LST_{daily}. Each panel corresponds to a different land cover type. For each land cover group, the least-squares linear regression forced through the origin and R^2 are shown.

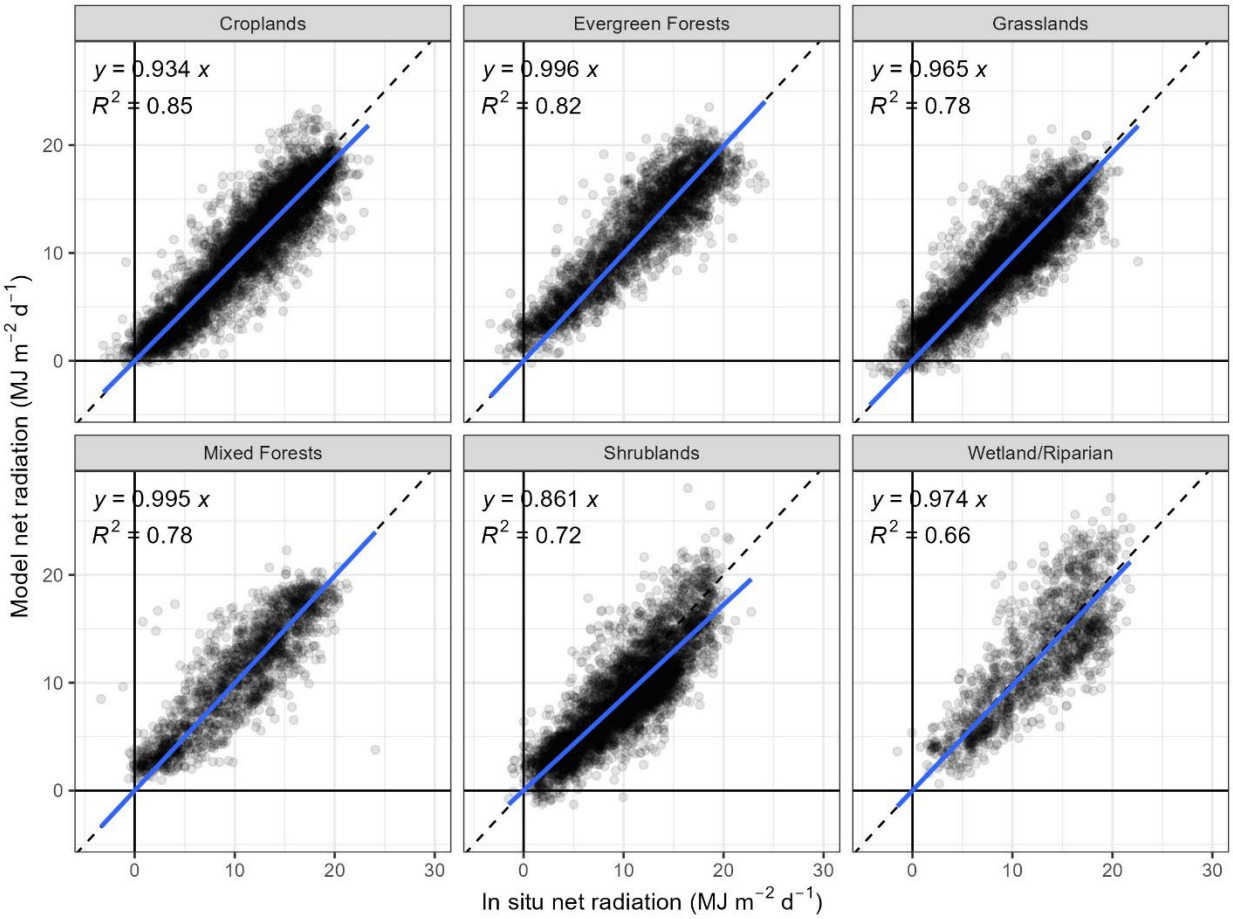

Figure S2 Evaluation of daily net radiation estimated from satellite observations and grid meteorological data. The x-axis represents the daily net radiation observed at flux tower sites, while the y-axis represents estimated daily net radiation based on Landsat scene and gridMET meteorological data. Each panel corresponds to a different land cover type. For each land cover group, the least-squares linear regression forced through the origin and R^2 are shown.

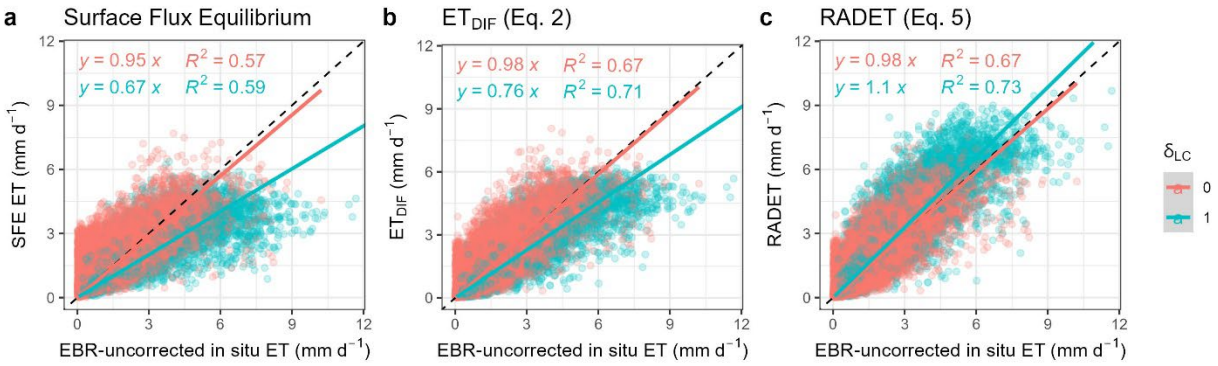

Figure S3 In situ ET observations versus estimated daily ET using the SFE (a), ETDIF (b) and RADET (c) models. Observed ET represents energy balance ratio (EBR) uncorrected data. The dashed line indicates the 1:1 line, and point colors differentiate $\delta_{LC} = 0$ and $\delta_{LC} = 1$. R^2 and the least-squares linear regression forced through the origin are shown (solid line).

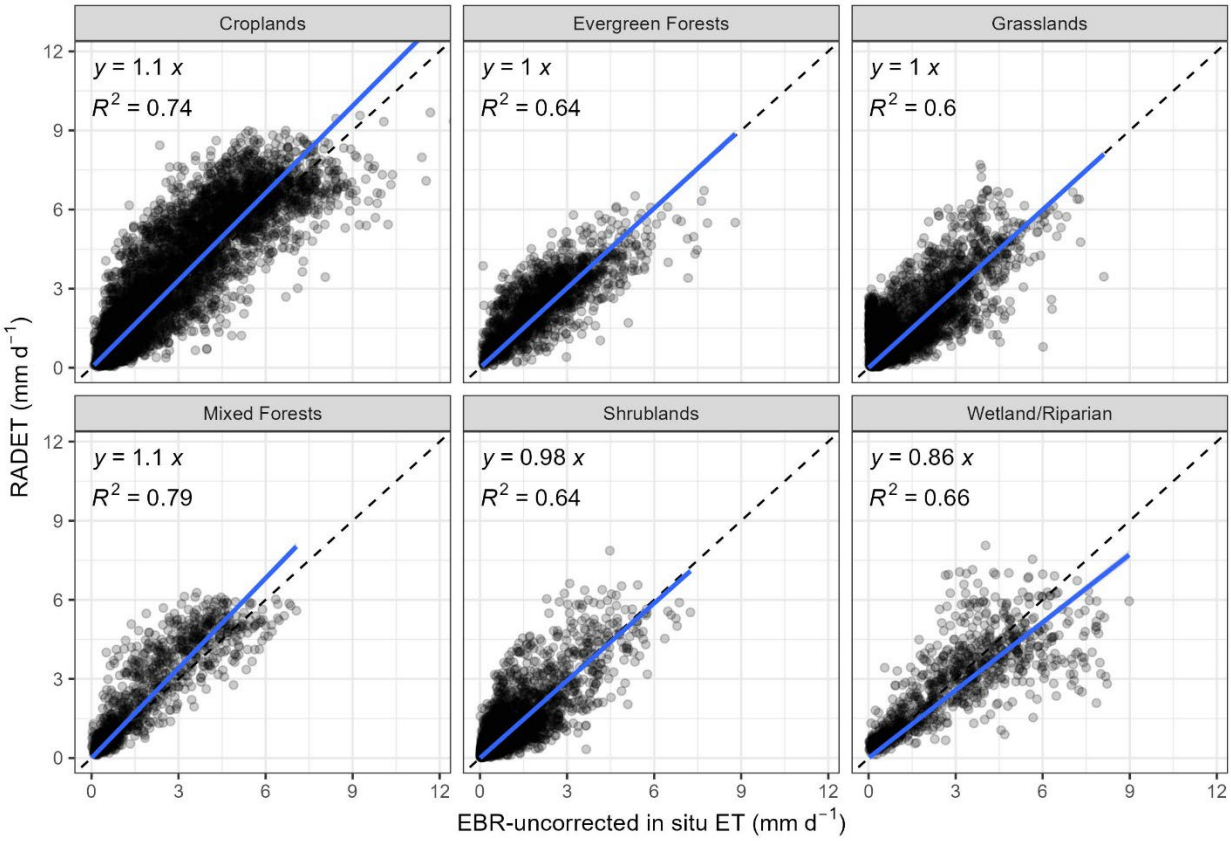

Figure S4 Daily RADET versus EBR-uncorrected in situ ET observations grouped by land cover type. For each land cover group, the least-squares linear regression forced through the origin and R^2 are shown.

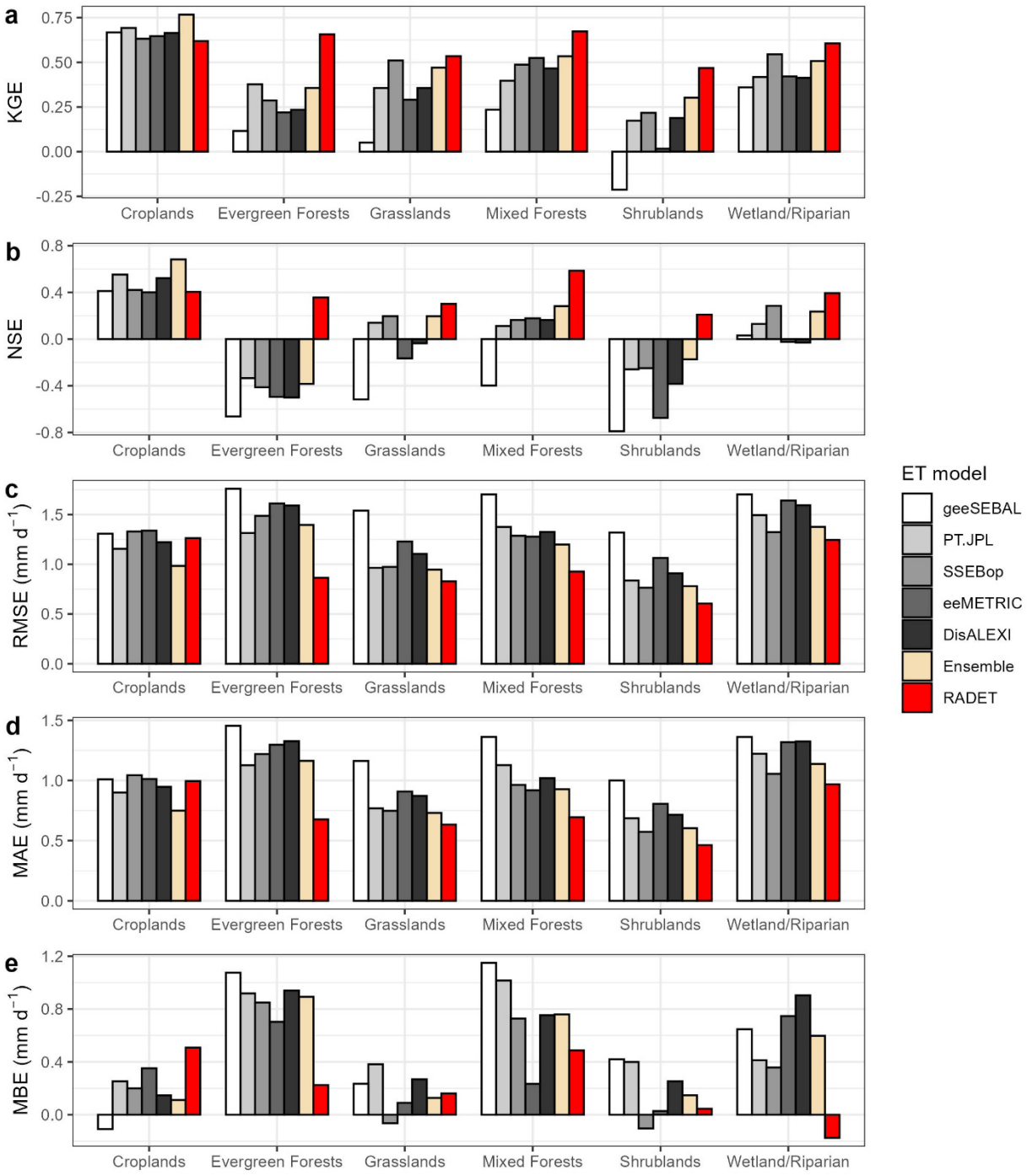

Figure S5 Comparison of daily error statistics between RADET and OpenET models, grouped by land cover type. Model evaluations were performed using EBR–uncorrected in situ ET as the benchmark.

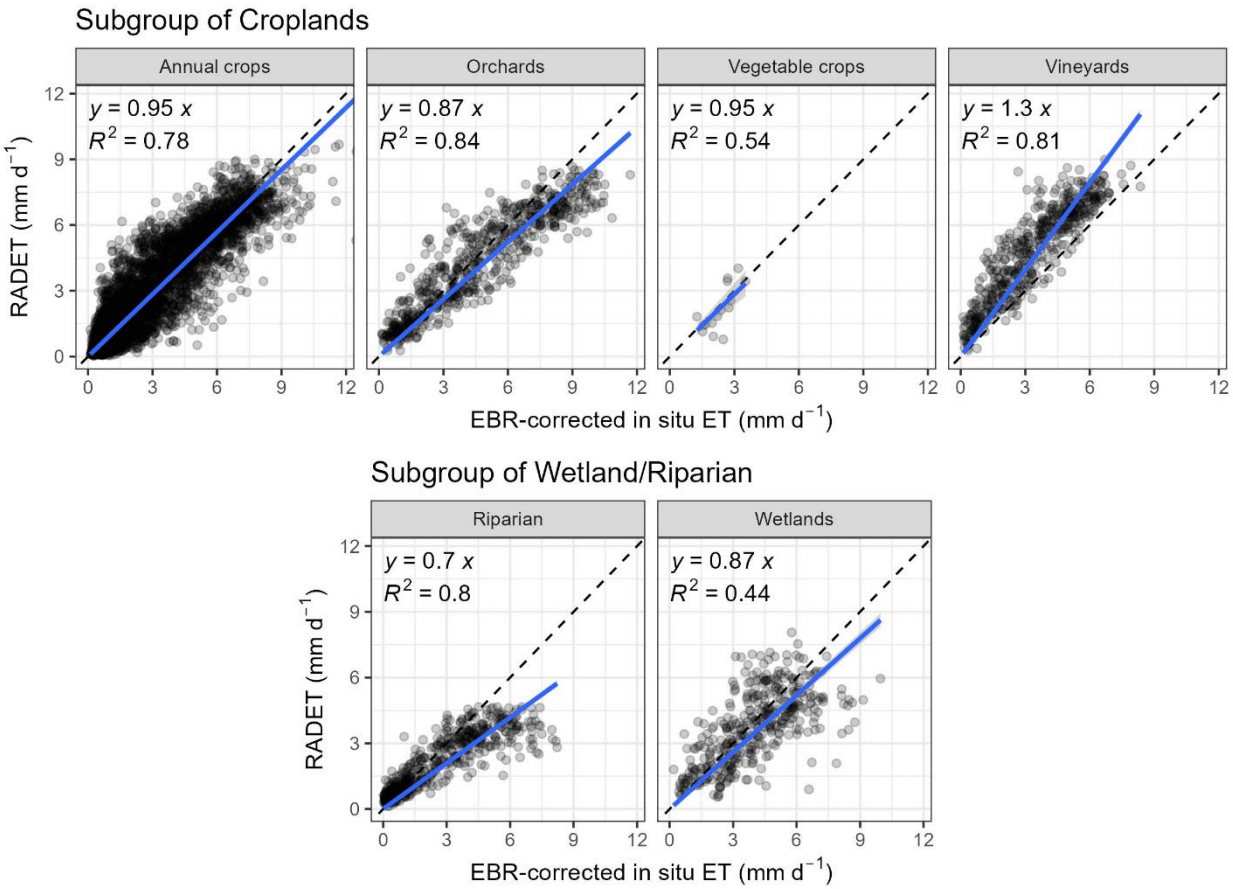

Figure S6 Daily RADET versus EBR-corrected in-situ ET observations grouped by land cover subgroups. For each land cover subgroup, R^2 and the least-squares linear regression forced through the origin are shown.

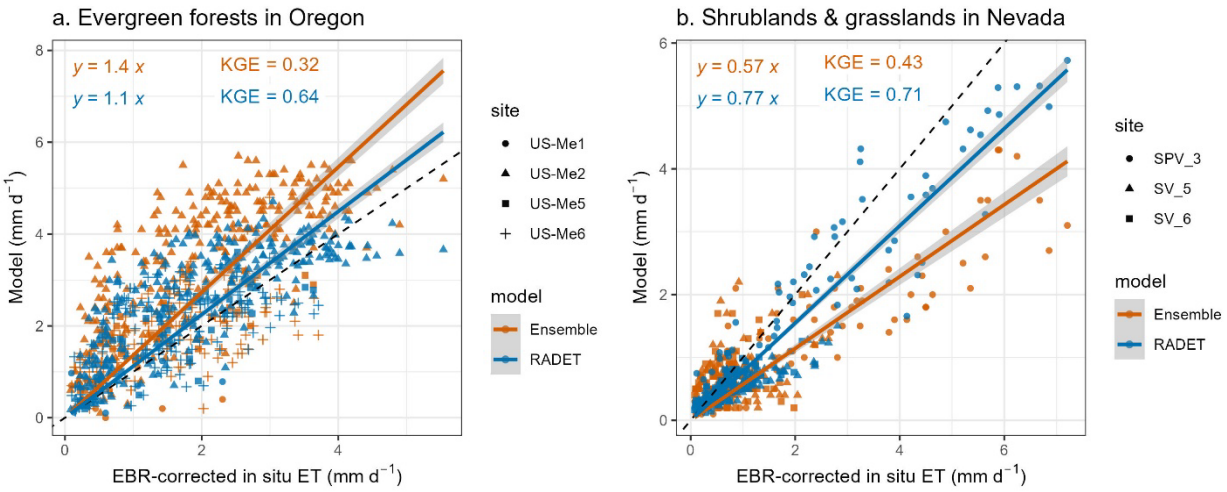

Figure S7 Model estimates versus in situ ET observations (EBR-corrected) for (a) forest sites shown in Figure 5 and (b) shrubland and grassland sites shown in Figure 6. Blue points represent the OpenET ensemble, whereas orange points indicate RADET estimates. Different point shapes correspond to different sites. The dashed line denotes the 1:1 line, and the colored solid lines represent the least-squares regression lines forced through the origin. The Kling-Gupta efficiency (KGE) and regression statistics are also shown.

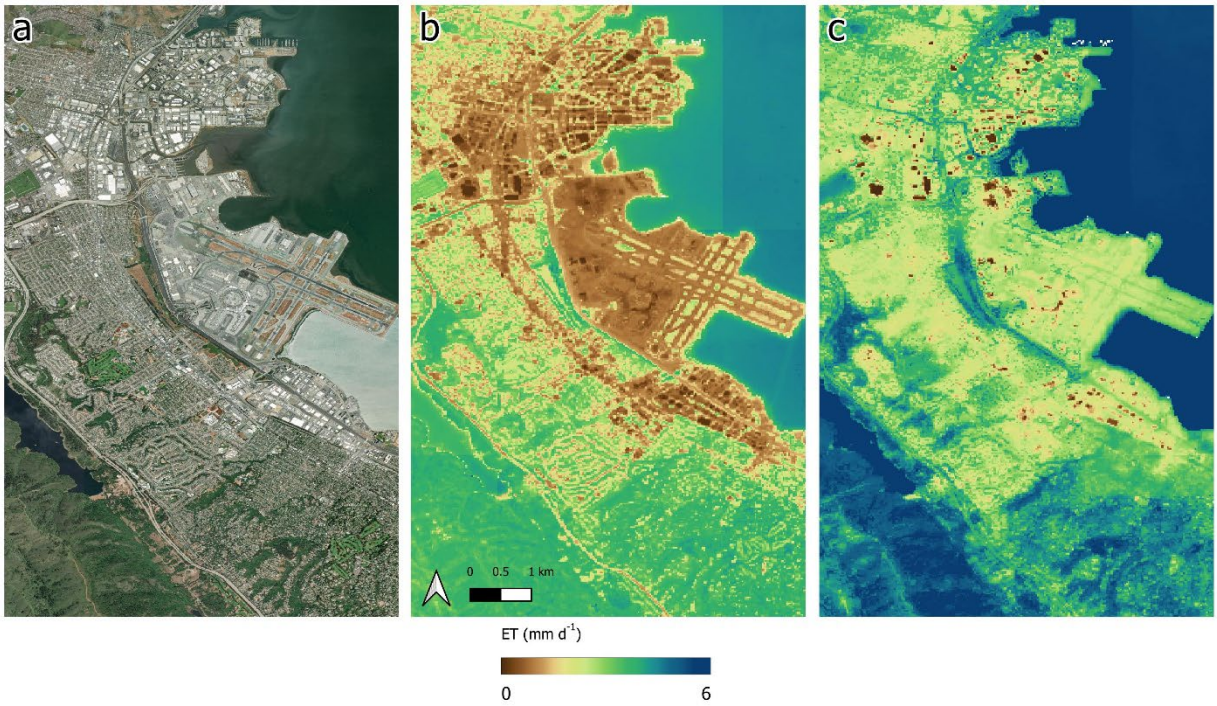

Figure S8 Daily ET patterns over a developed area. (a) World Imagery basemap (Esri, Maxar, Earthstar Geographics, and the GIS User Community), (b) RADET, and (c) OpenET ensemble for a Landsat 8 scene acquired on July 19, 2024, near San Francisco International Airport (37.62°N, 122.37°W). The OpenET ensemble exhibits unrealistically high ET over paved surfaces (e.g., airport runway), whereas RADET does not.

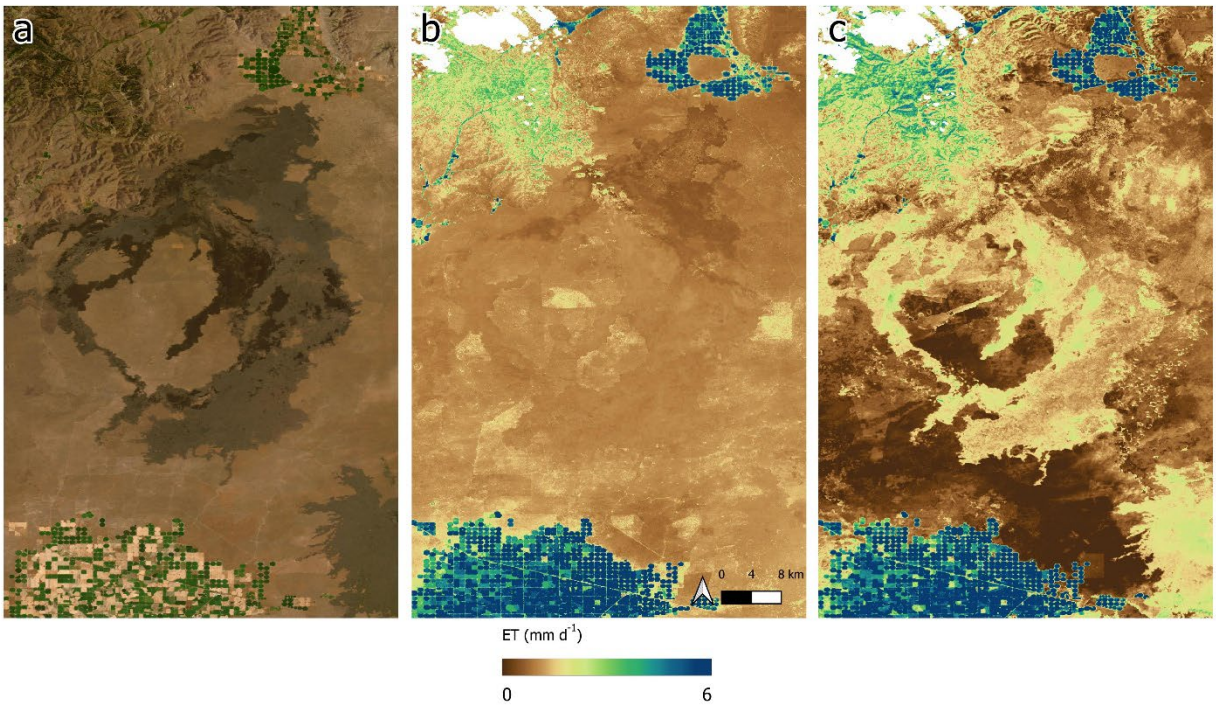

Figure S9 Daily ET patterns over a dark volcanic surface. (a) World Imagery basemap (Esri, Maxar, Earthstar Geographics, and the GIS User Community), (b) RADET, and (c) OpenET ensemble for a Landsat 8 scene acquired on July 23, 2024, near Craters of the Moon, Idaho (43.27°N, 113.46°W). The OpenET ensemble exhibits unrealistically high ET over the dark volcanic surfaces, whereas RADET does not. White areas indicate cloud masking.

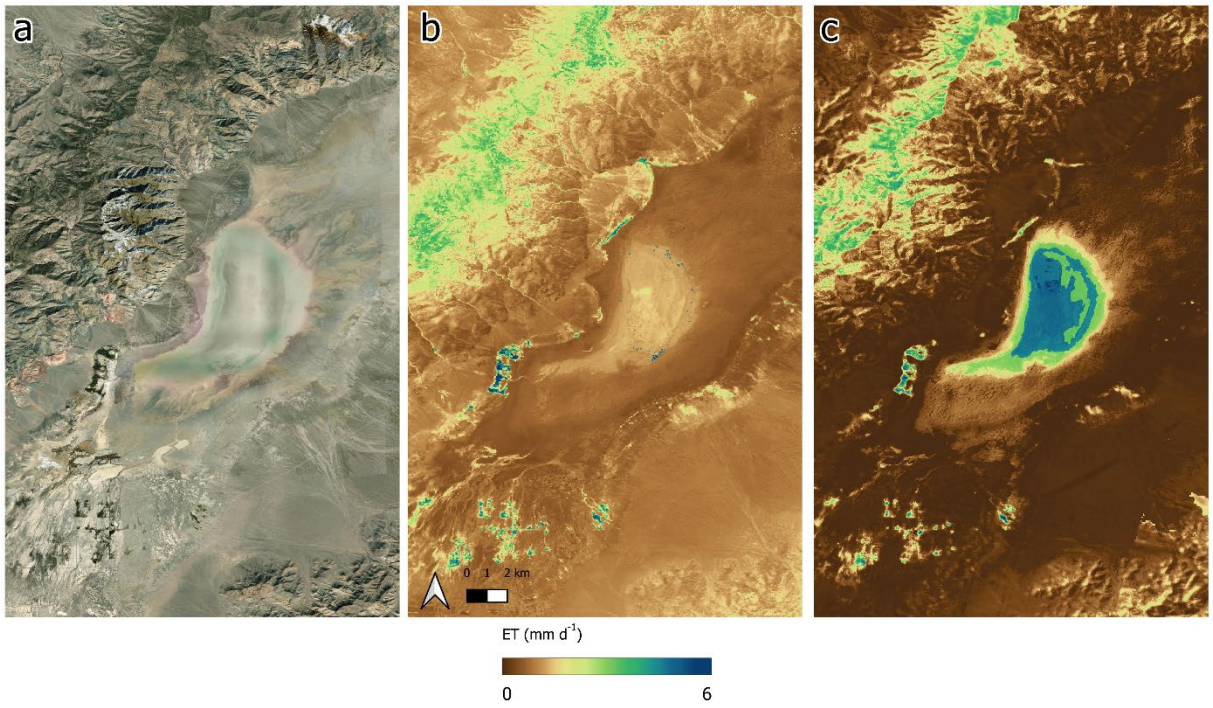

Figure S10 Daily ET patterns over a white salt-crusted surface. (a) World Imagery basemap (Esri, Maxar, Earthstar Geographics, and the GIS User Community), (b) RADET, and (c) OpenET ensemble for a Landsat 8 scene acquired on July 21, 2024, near Dixie Valley playa, Nevada (39.80°N, 117.98°W). The OpenET ensemble exhibits unrealistically high ET over the white salt-crusted surface, whereas RADET reduces this issue.

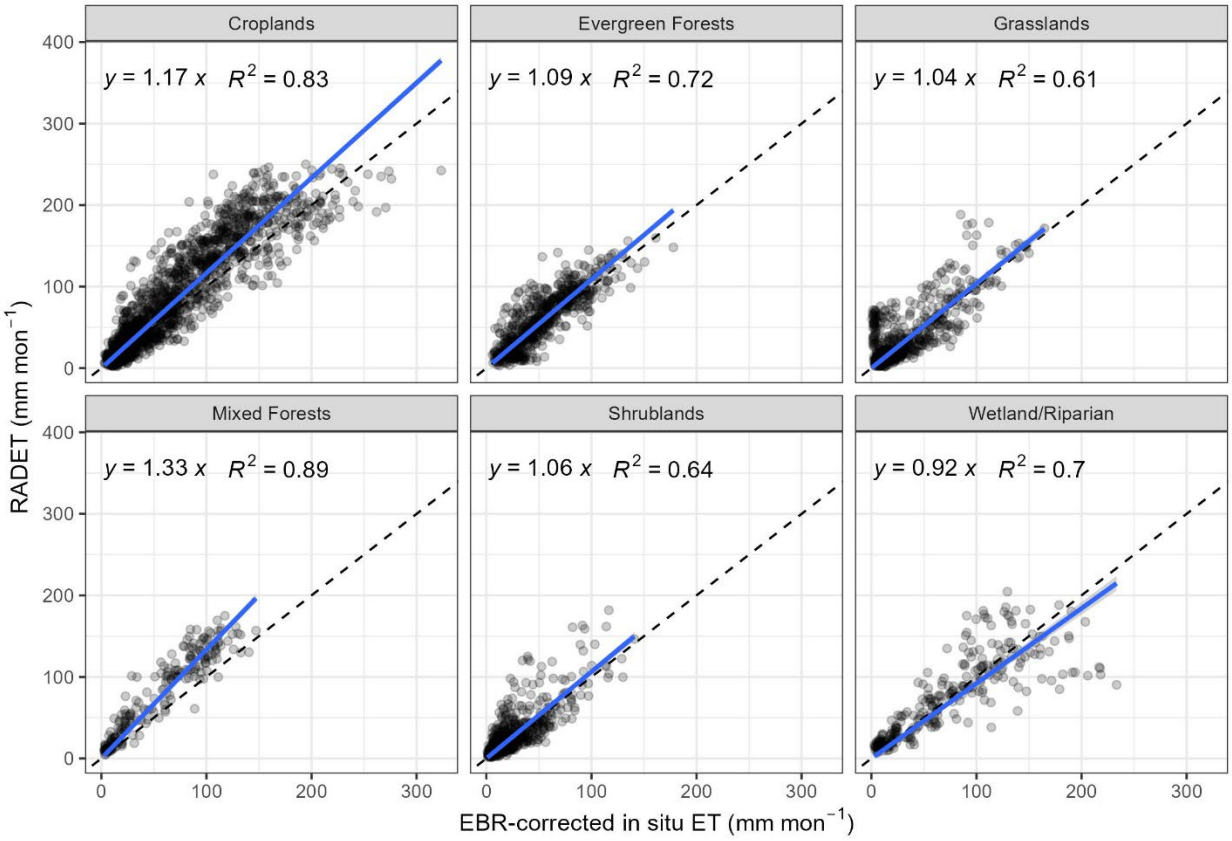

Figure S11 Monthly RADET versus EBR-uncorrected in-situ ET observations grouped by land cover type. Points indicate results under the strict benchmark criterion (≤5 gap-filled days). For each land cover group, R^2 *and* the least-squares linear regression forced through the origin are shown.

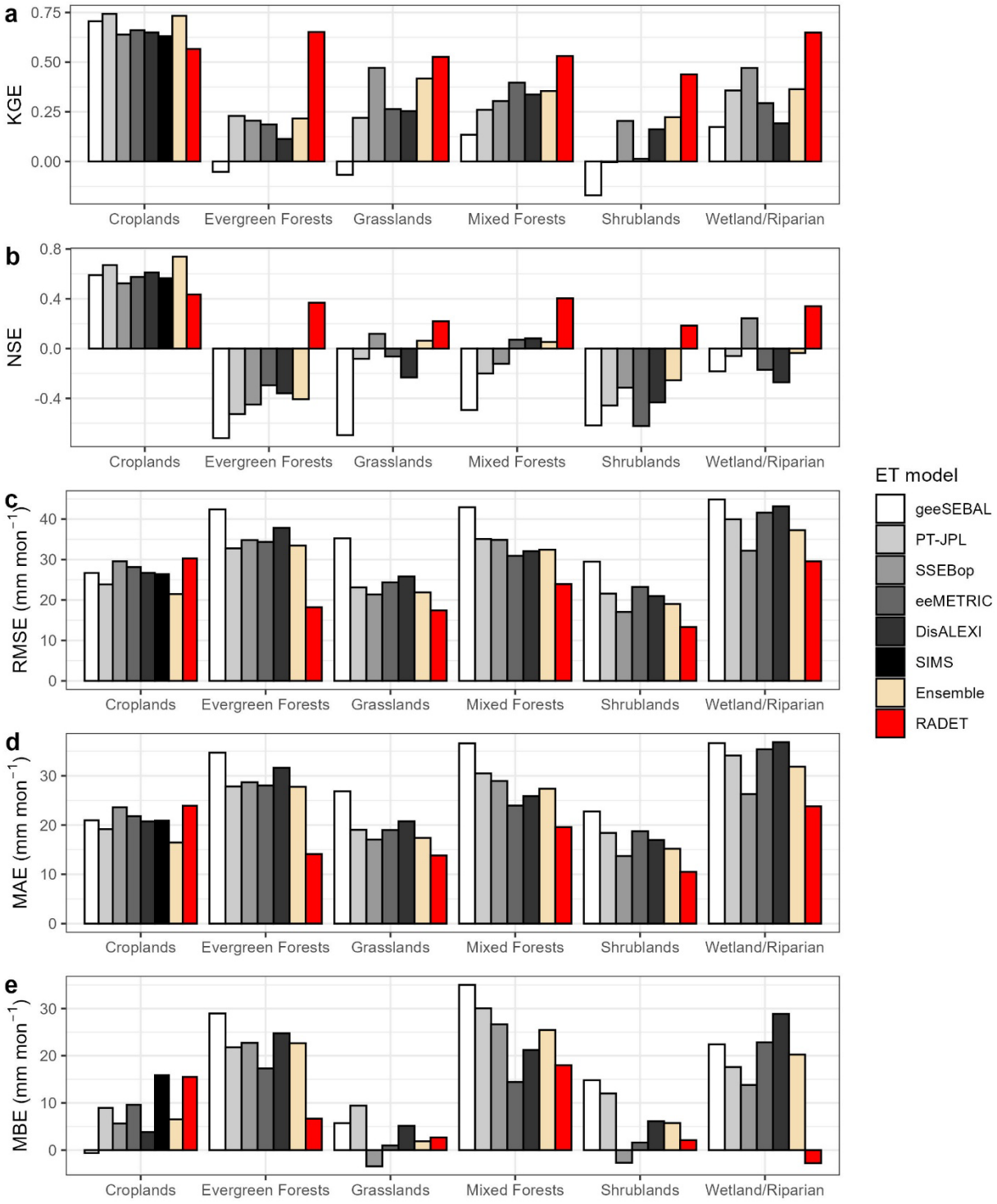

Figure S12 Comparison of monthly error statistics between RADET and OpenET models, grouped by land cover type. Model evaluations were performed using EBR–uncorrected in situ ET as the benchmark.

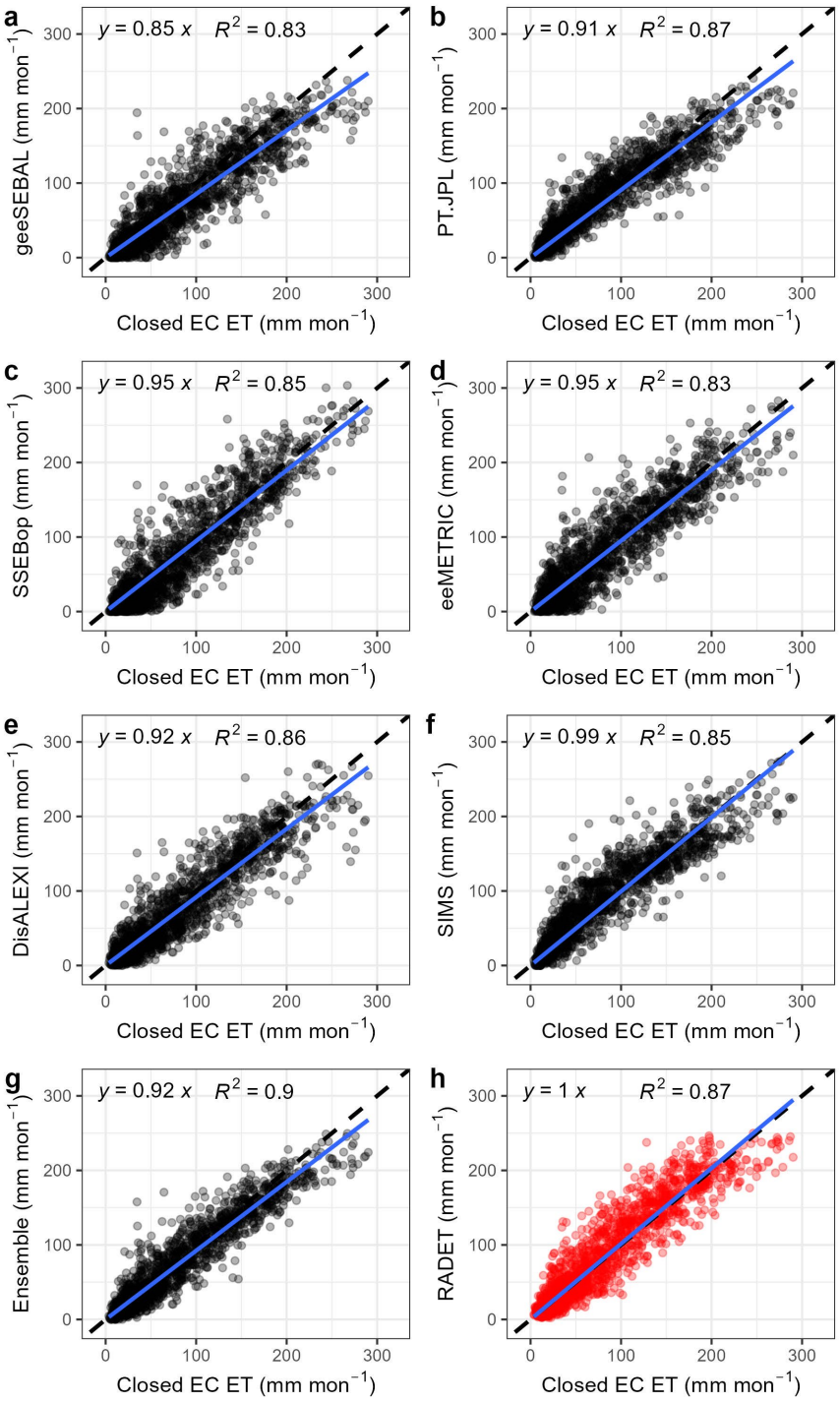

Figure S13 Monthly model estimates versus in situ ET observations (EBR-corrected) over cropland sites. Panels (a)–(f) show individual OpenET model estimates, panel (g) shows the OpenET ensemble, and panel (h) presents RADET. The dashed line denotes the 1:1 line, and the solid lines represent least-squares regression lines forced through the origin.

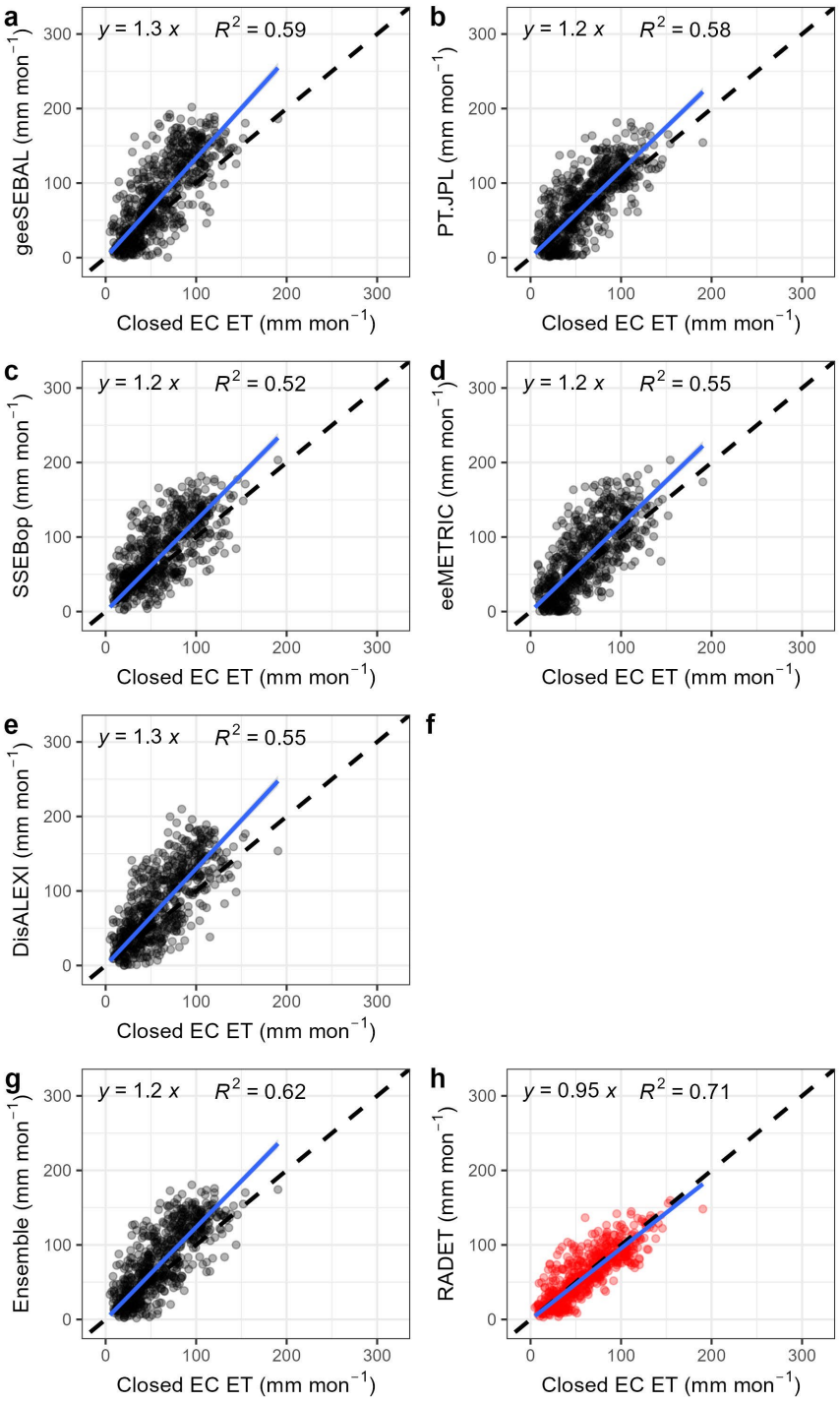

Figure S14 Monthly model estimates versus in situ ET observations (EBR-corrected) over evergreen forest sites. Panels (a)–(f) show individual OpenET model estimates, panel (g) shows the OpenET ensemble, and panel (h) presents RADET. The dashed line denotes the 1:1 line, and the solid lines represent least-squares regression lines forced through the origin.

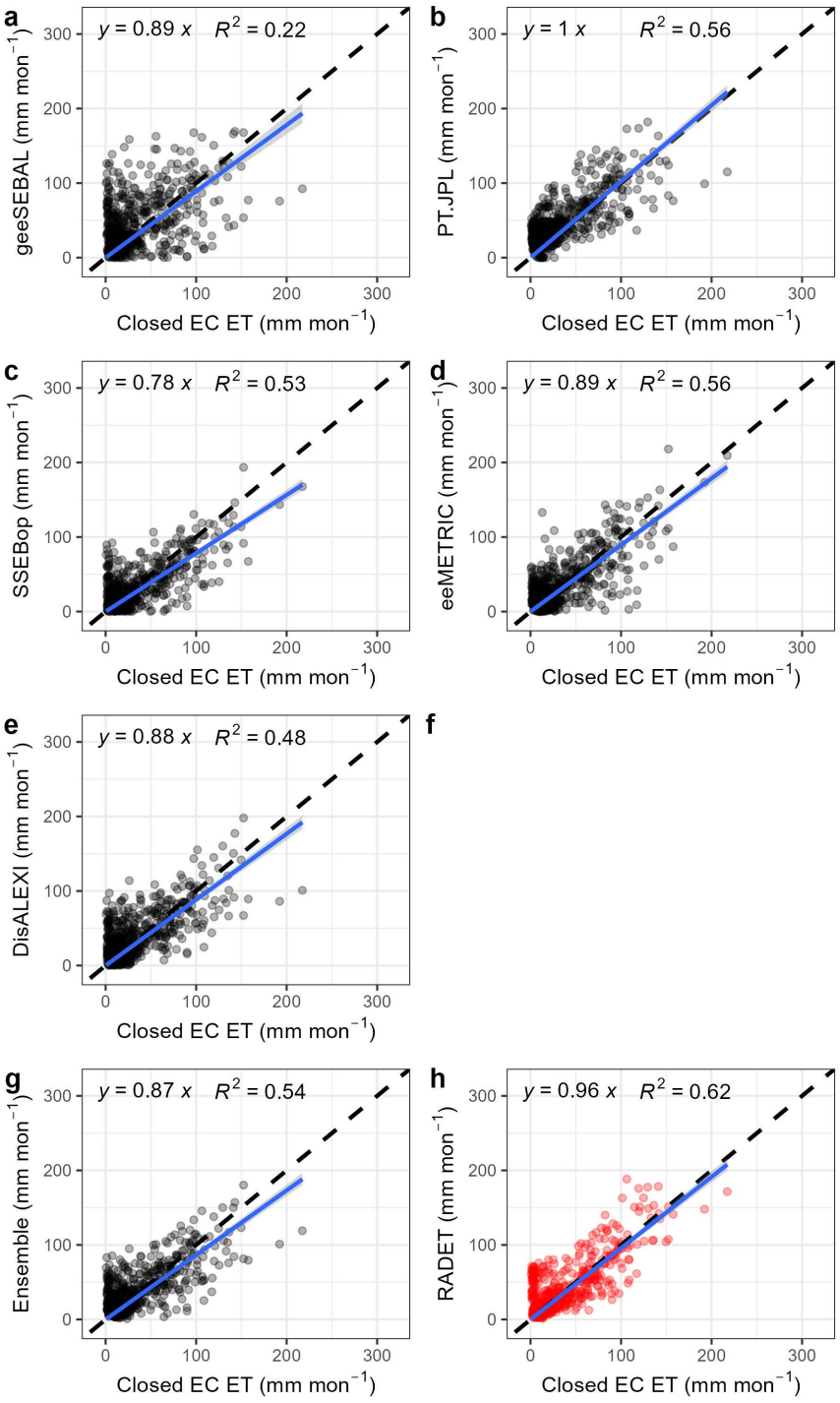

Figure S15 Monthly model estimates versus in situ ET observations (EBR-corrected) over grassland sites. Panels (a)–(f) show individual OpenET model estimates, panel (g) shows the OpenET ensemble, and panel (h) presents RADET. The dashed line denotes the 1:1 line, and the solid lines represent least-squares regression lines forced through the origin.

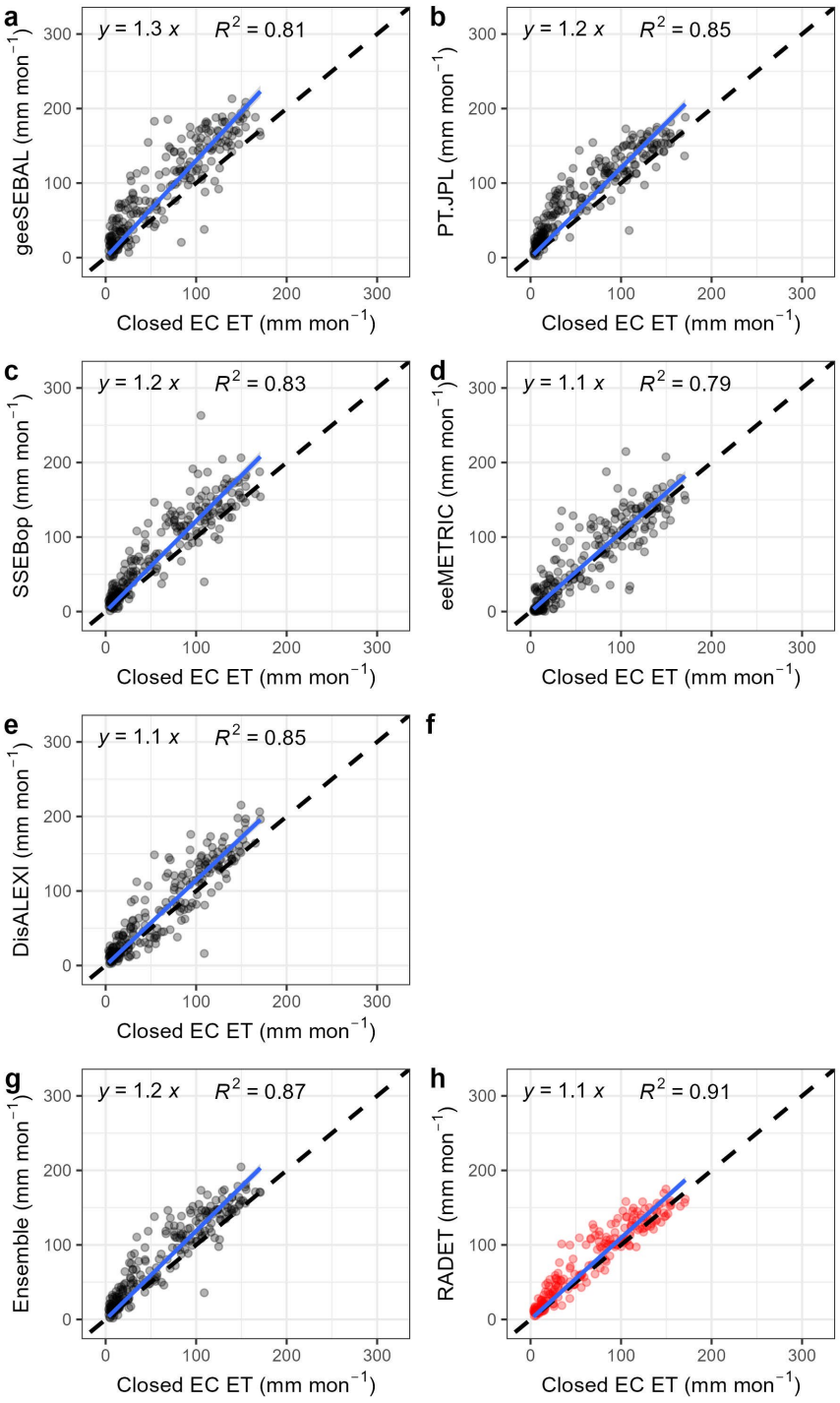

Figure S16 Monthly model estimates versus in situ ET observations (EBR-corrected) over mixed forest sites. Panels (a)–(f) show individual OpenET model estimates, panel (g) shows the OpenET ensemble, and panel (h) presents RADET. The dashed line denotes the 1:1 line, and the solid lines represent least-squares regression lines forced through the origin.

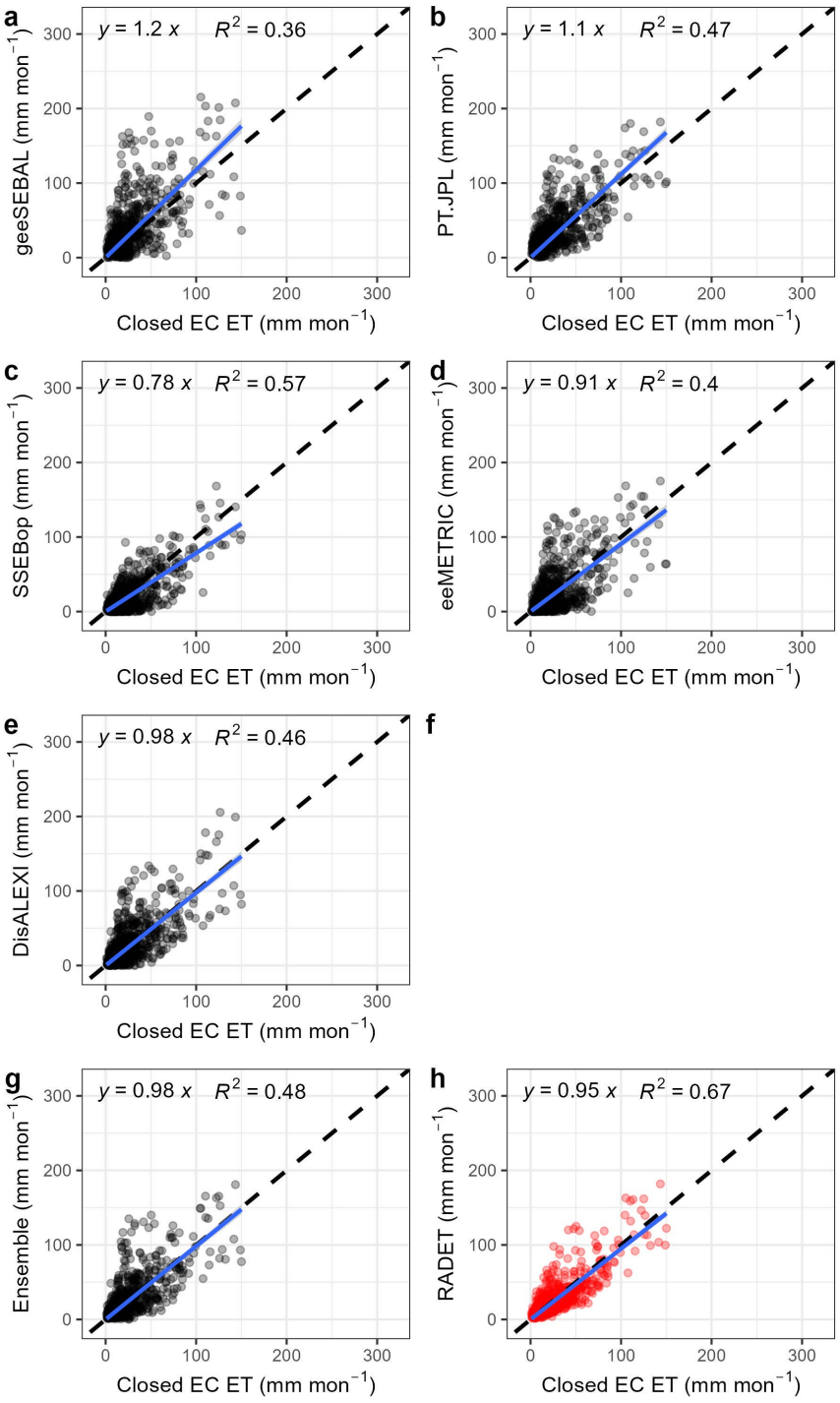

Figure S17 Monthly model estimates versus in situ ET observations (EBR-corrected) over shrubland sites. Panels (a)–(f) show individual OpenET model estimates, panel (g) shows the OpenET ensemble, and panel (h) presents RADET. The dashed line denotes the 1:1 line, and the solid lines represent least-squares regression lines forced through the origin.

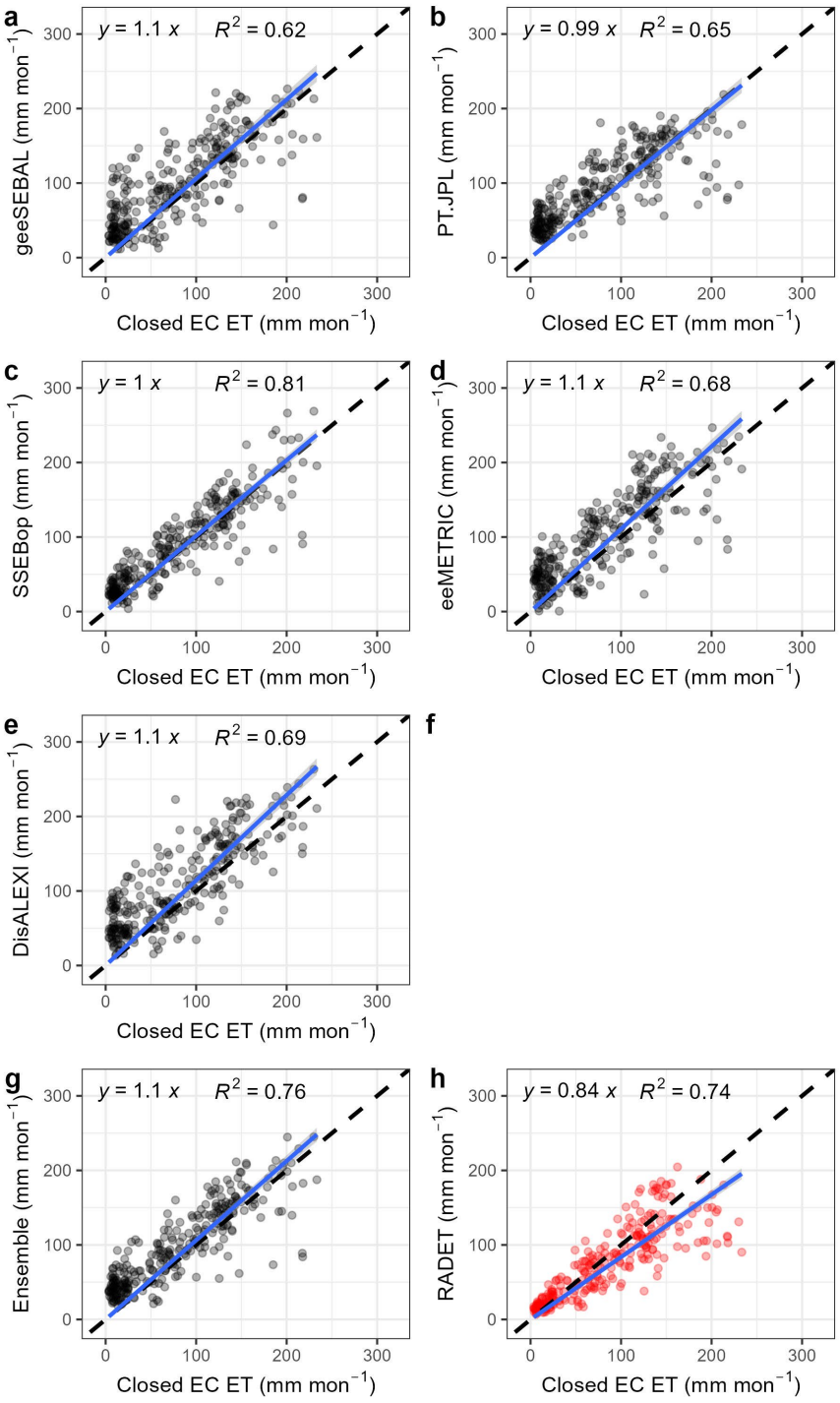

Figure S18 Monthly model estimates versus in situ ET observations (EBR-corrected) over wetland/riparian sites. Panels (a)–(f) show individual OpenET model estimates, panel (g) shows the OpenET ensemble, and panel (h) presents RADET. The dashed line denotes the 1:1 line, and the solid lines represent least-squares regression lines forced through the origin.

a

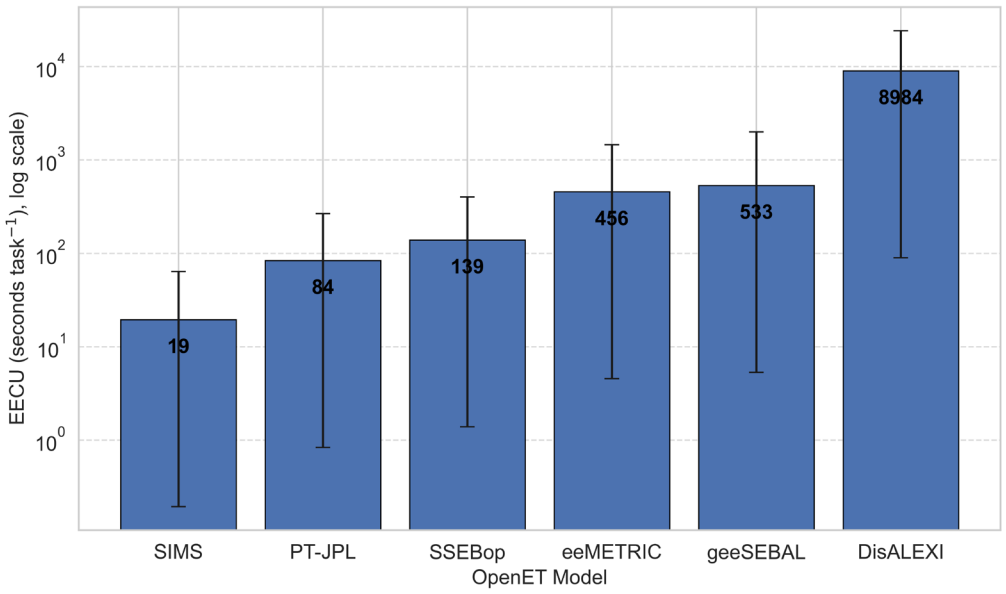
EECU (seconds task^{-1}), log scale)
10^4
10^3
10^2
10^1
10^0
19
84
139
456
533
8984
SIMS
PT-JPL
SSEBop
eeMETRIC
geeSEBAL
DisALEXI
OpenET Model

b

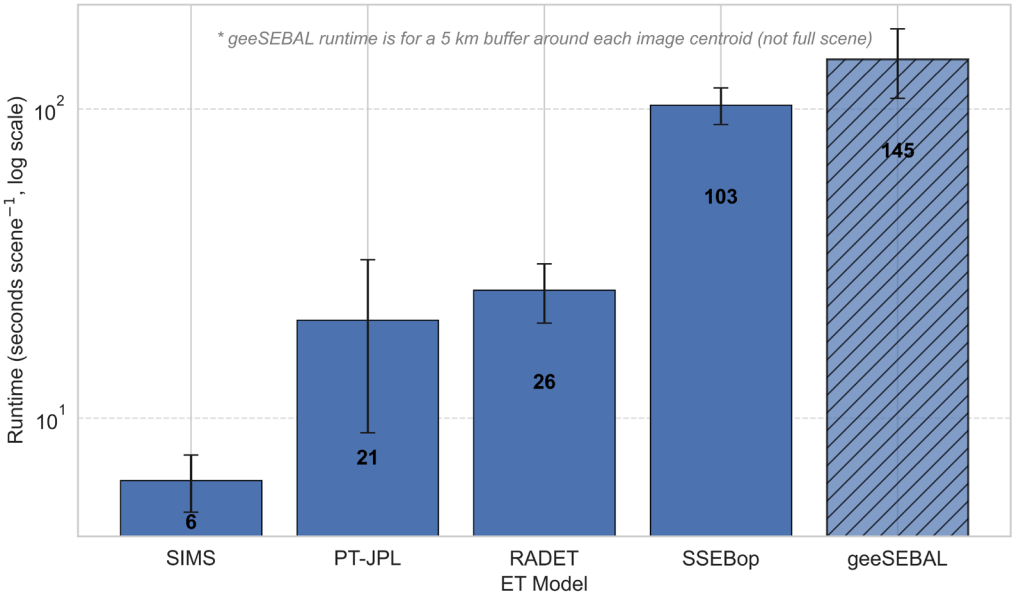
* geeSEBAL runtime is for a 5 km buffer around each image centroid (not full scene)
Runtime (seconds scene^{-1}, log scale)
10^2
10^1
6
21
26
103
145
SIMS
PT-JPL
RADET
SSEBop
geeSEBAL
ET Model

c

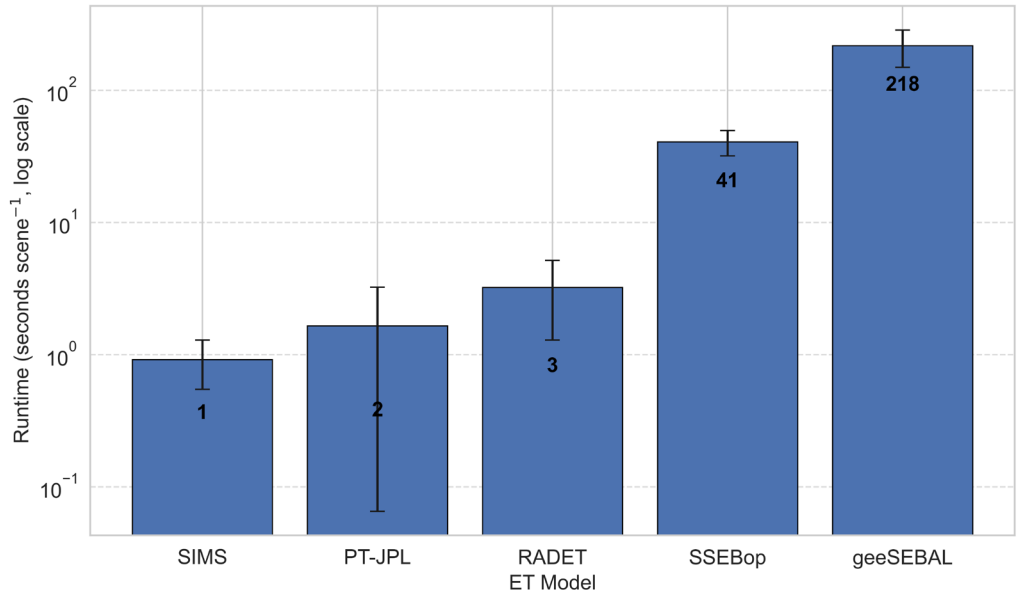

Figure S19 Computational efficiency comparison of RADET and OpenET models. **(a)** Earth Engine Compute Unit (EECU) hours per task from operational OpenET production exports, showing median, interquartile range, and outliers on a log scale. **(b)** Runtime comparison for full Landsat 8 scene processing across RADET, PT-JPL, SIMS, and SSEBop models. The 10 full scenes span diverse regions across CONUS: the Intermountain West (Idaho, Montana), Southwest (New Mexico), Central Plains (Kansas, Oklahoma), Upper Midwest (Minnesota, Wisconsin), Mid-Atlantic (Pennsylvania), Midwest (Kentucky, Illinois), Utah, Northern Plains (South Dakota, Minnesota), Northeast (New Jersey, Pennsylvania), and Gulf Coast (Texas, Louisiana). We also compared against geeSEBAL runs performed using a 5 km buffer around scene centroids to avoid Google Earth Engine (GEE) memory limitations. Full-scene processing for geeSEBAL would otherwise require chunking each scene into multiple tiles and mosaicking them afterward, leading to additional computational overhead, when running the model in an interactive environment (like Jupyter Notebook) or via local Python scripts. **(c)** Runtime comparison using a 5 km buffer around scene centroids, demonstrating model performance under reduced computational load. These include 10 scenes from the western Great Basin (California, Nevada, Oregon), eastern Great Basin (Nevada, Utah, Idaho), Colorado, Great Plains (Nebraska, Kansas), Lower Mississippi (Arkansas, Mississippi), Appalachia (Virginia, West Virginia), Midwest (Indiana, Michigan), Wyoming, Ozarks (Missouri, Arkansas), and Willamette Valley (Oregon). Note that separate scenes for **(b)** and **(c)** were deliberately chosen to avoid automatic GEE caching effects on model runs. We excluded eeMETRIC and DisALEXI from **(b)** and **(c)** because eeMETRIC source code is not publicly available, while DisALEXI requires the highest EECU among all OpenET models as shown in **(a)**. For each ET model, the values shown within the bars represent the average (rounded to the nearest integer) EECU (seconds task^{-1}) and runtimes (seconds scene^{-1}), while the error bars indicate the corresponding standard deviations computed across **(a)** GEE export tasks and **(b-c)** scenes. These runtime comparisons demonstrate that RADET consistently shows lower computational cost across all benchmarks, and is comparable to PT-JPL, with only SIMS displaying better computational efficiency.